HAW HAMBURG

MASTERTHESIS

Simulation-Based Development of a Metal Hydride Compressor for Hydrogen Pipeline Injection

submitted on 01.04.2026

Marisa Klink

First Examiner:	Prof. Dr.-Ing. Marc Hölling
Second Examiner:	Prof. Dr.-Ing. Julian Jepsen
Supervisor:	M. Sc. Lukas Fleming

in collaboration with
Helmholtz-Zentrum hereon and
Hamburg Green Hydrogen Hub

HOCHSCHULE FÜR ANGEWANDTE WISSENSCHAFTEN HAMBURG
Faculty Life Sciences, Department Process Engineering
Ulmenliet 20
21033 Hamburg

Zusammenfassung

In dieser Arbeit wird ein Metallhydridkompressor (MHK) für die Einspeisung in Wasserstoffpipelines als mögliche Alternative zur herkömmlichen mechanischen Verdichtung entwickelt, wobei das „Hamburg Green Hydrogen Hub“ (HGHH) als praxisnaher Referenzfall mit standortspezifischen Randbedingungen dient. Zur Entwicklung und Optimierung einer zweistufigen MHK-Konfiguration, die auf die standortspezifischen Randbedingungen zugeschnitten ist, wurden dynamische Prozesssimulationen in Aspen Custom Modeler (ACM) auf Grundlage eines validierten Models durchgeführt: Ein Verdichtungsverhältnis von 2,67 (30 bis 80 bar) und ein enges Temperaturfenster zwischen Kühltemperaturen von 35 °C und einer Elektrolyseur-Abwärme von 46 °C.

Eine kriterien-basierte Literaturrecherche ergab, dass Hydralloy C1 (Stufe 1: 30 bis ca. 50 bar, 10 bis 65 °C) und $Ti_{1.1}CrMn$ (Stufe 2: ca. 50 bis 80 bar, 10 bis 60 °C) die optimalen Legierungen für diesen Anwendungsfall sind. Die begrenzten experimentellen Daten zu Druck-Konzentrations-Isothermen wurden mithilfe der Purdue Metal Hydride Toolbox erweitert und als polynomiale Oberflächenanpassungen in ACM implementiert. Eine systematische Parameteroptimierung der ein- und zweistufigen Betriebskonfigurationen, Temperaturen, Massenverhältnisse zwischen den Stufen, Zykluszeiten und Bettgeometrien ergab eine Konfiguration im Labormaßstab mit einer gesamten spezifischen Produktivität von 132,21 $Ln/kg_{MH}/h$.

Die industrielle Skalierung auf den Wasserstoff-Massenströme des 100-MW-Elektrolyseurs erfordert eine Gesamtlegierungsmasse von etwa 169.801 kg sowie Bettabmessungen von 1,20 m und 28,3 m Länge pro Stufe. Der maximale Heizbedarf von 18,81 MW wird quantitativ durch die verfügbare Abwärme (23,1 bis 41,7 MW, abhängig von den Systemgrenzen und dem Elektrolyseur-Degradierung) gedeckt, jedoch liegt das verfügbare Temperaturniveau (46 °C) unter den Anforderungen für Stufe 1 (65 °C, ΔT = 19 K) und Stufe 2 (60 °C, ΔT = 14 K).

Die vorliegende Arbeit entwickelt eine simulationsbasierte Grundlage für MHK im industriellen Maßstab, definiert die thermische Integration und skizziert Prioritäten für die weitere Arbeit beispielsweise die experimentelle Validierung und die techno-ökonomische Analyse.

Abstract

This thesis develops a metal hydride compressor (MHC) for hydrogen pipeline injection as a possible alternative to conventional mechanical compression, using the Hamburg Green Hydrogen Hub (HGHH) as a real-world reference case with site-specific boundary conditions. Dynamic process simulation in Aspen Custom Modeler (ACM) based on a validated model was employed to develop and optimize a two-stage MHC configuration tailored to site-specific boundary conditions: a compression ratio of 2.67 (30 to 80 bar) and a narrow thermal window between cooling temperatures (35 °C) and electrolyzer waste heat (46 °C).

A criteria-based literature search identified Hydralloy C1 (Stage 1: 30 to approximately 50 bar, 10 to 65 °C) and $Ti_{1.1}CrMn$ (Stage 2: approximately 50 to 80 bar, 10 to 60 °C) as optimal alloys. Limited experimental pressure-composition isotherm data were extended using the Purdue Metal Hydride Toolbox and implemented as polynomial surface fits in ACM. Systematic parameter optimization of operating one- and two-stage configurations, temperatures, alloy mass ratios, cycle times, and bed geometries yielded a laboratory-scale configuration with a total specific productivity of 132.21 $Ln/kg_{MH}/h$.

Industrial scale-up for the 100 MW electrolyzer requires about 169,801 kg total alloy mass and bed dimensions of 1.20 m bed-diameter and 28.3 m bed-length per stage. The maximum heating demand of 18.81 MW is quantitatively covered by available waste heat (23.1 to 41.7 MW, depending on system boundary and degradation state), but the temperature level (46 °C) falls short of Stage 1 (65 °C, ΔT = 19 K) and Stage 2 (60 °C, ΔT = 14 K) requirements.

Two technically viable integration pathways were identified: Scenario A (upstream atmospheric PEM electrolyzer) requires heat pump integration for temperature upgrading, Scenario B (pressurized electrolyzer expansion) leverages higher-temperature electrolyzer technology (exemplary Alkaline Electrolysis with 75 to 80 °C operating temperature) for direct thermal drive. MHC advantages, such as vibration-free operation, low maintenance and utilization of low-grade waste heat instead of electrical energy to drive the compression, remain systemically relevant, though direct integration under current HGHH conditions is not possible without targeted adaptations.

The present work develops a simulation-based foundation for MHC at industrial scale and clearly defining thermal integration as the binding constraint and outlining priorities in further work for experimental validation and techno-economic analysis.

Contents

List of Figures

List of Tables

List of Abbreviations

ACM Aspen Custom Modeler

AEL Alkaline Electrolysis

AEM Anion Exchange Membrane Electrolysis

EHM Energiehub Moorburg GmbH

EOH Equivalent operating hours

HEnW Hamburger Energiewerke

HGHH Hamburg Green Hydrogen Hub

HH-WIN Hamburger Wasserstoff-Industrie-Netz

HTF Heat Transfer Fluid

IPCEI Important Project of Common European Interest

MH Metal hydrides

MHC Metal hydride compressor

PCIs Pressure-composition isotherms

PEM Proton Exchange Membrane Electrolysis/Polymer Electrolyte Membrane Electrolysis

SOEL Solid Oxide Electrolysis

List of Symbols

A	Pre-exponential factor	$s^{-}1$
α	Reacted fraction	-
c_p	Specific heat capacity at constant pressure	$\mathrm{J\,kg^{-1}\,K^{-1}}$
c_v	Specific heat capacity at constant volume	$\mathrm{J\,kg^{-1}\,K^{-1}}$
d_{bed}	Bed diameter	m
ΔC	Cycle productivity (reversible hydrogen capacity)	%
ΔH	Enthalpy change	$\mathrm{J\,mol^{-1}}$
ΔS	Entropy change	$\mathrm{J\,mol^{-1}\,K^{-1}}$
E_a	Apparent activation energy	$\mathrm{kJ\,mol^{-1}}$
E^0_{rev}	Reversible cell voltage at standard conditions	V
η_{plant}	Plant efficiency (HHV)	%
E^0_{tn}	Thermoneutral voltage at standard conditions	V
$F(P)$	Pressure dependency term	-
$G(\alpha)$	Kinetic model	-
γ	Heat capacity ratio / isentropic exponent (c_p/c_v)	-
$\dot{H}_{2,\mathrm{HHV}}$	Hydrogen chemical power (HHV)	MW
$K(T)$	Temperature dependency term	$\mathrm{h^{-1}}$
l_{bed}	Bed length	m
M_{alloy}	Alloy mass	kg

n	Polytropic index	-
P	Pressure	bar
P_0	Reference pressure	bar
P_{eq}	Equilibrium pressure	bar
P_{plant}	Plant electrical power	MW
P_{stack}	Stack electrical power	MW
Q	Heat	J
$\dot{Q}$	Thermal power / waste heat	kW
MW		
$\dot{Q}_{\text{avg}}$	Average heating power	kW
R	Universal gas constant(8.314 J/mol K)	$\text{J mol}^{-1}\,\text{K}^{-1}$
R^2	Determination coefficient	-
t	Time	s
t_{lifetime}	Lifetime (equivalent operating hours)	h
t_{wall}	Wall thickness	mm
V	Volume	m^3
V_{bed}	Bed volume	m^3
W_{isen}	Isentropic compression work	J
W_{iso}	Isothermal compression work	J
W_p	Polytropic compression work	J
wt	Gravimetric hydrogen capacity	wt %
wt_{max}	Maximum gravimetric hydrogen capacity	wt %
x	Stoichiometric quantity of hydrogen bonded to MH	-
y	Stoichiometric quantity of hydrogen in the α-phase	-

1 General Introduction

This thesis investigates the suitability of a Metal hydride compressor (MHC) as an alternative to mechanical compression for hydrogen conditioning at industrial scale, using dynamic process simulation in Aspen Custom Modeler (ACM). The work is conducted in direct collaboration with the Hamburg Green Hydrogen Hub (HGHH) at the former Moorburg coal power plant site in Hamburg, providing real-world boundary conditions for the analysis.

The following chapter motivates this investigation by outlining the role of green hydrogen in Hamburg's energy transition and the associated demand for reliable compression technologies.

1.1 Motivation

The transition towards a climate-neutral energy system is one of the central challenges of this century. Germany has committed to achieving greenhouse-gas neutrality by 2045, which requires a rapid and profound reduction of emissions in all sectors. Hamburg has translated these national targets into its own climate policy. In the first update of the Hamburg Climate Plan, the city has committed itself to the goal of reducing carbon dioxide emissions by 55% by 2030 compared to 1990 and achieving climate neutrality by 2050. In the second update at the end of 2023, this ambition was tightened further to a 70% reduction by 2030 and carbon dioxide emission neutrality by 2045. [1, 2, 3].

A crucial lever to reach these targets is the decarbonization of energy supply for industry, port operations, transport (shipping, heavy-duty road transport, air traffic), and heat. The decommissioning of large coal-fired power plants such as Moorburg and the planned phase-out of coal based district heating by 2030 create a substantial gap in the energy system that must be filled with climate-compatible alternatives.

In the short and medium term, natural gas will partly take over this role, in the long term, however, Hamburg's strategy explicitly relies on green hydrogen as a key building block of a climate-neutral energy system [4, 5, 6].

Even so, green hydrogen is not only relevant for the decarbonization of Hamburg's district heating system. It is also particularly important for energy-intensive sectors, in which direct electrification and therefore decarbonization through (green) electricity use alone is not technically or economically feasible [6].

The steel industry is a prime example of such a sector. In Hamburg's steel production, process-related emissions occur in the existing direct-reduction plant because natural gas is used as a chemical reducing agent. For this reason, the second update of the Hamburg Climate Plan envisages a federally funded, hydrogen-based direct-reduction unit with a capacity of 100,000 tons of sponge iron per year, which is scheduled to go into operation around 2026/2027 and to replace natural gas with green hydrogen, thereby significantly lowering process-related carbon dioxide emissions [3].[1]

At the national level, Germany's Hydrogen Action Plan also identifies the need for a shift from the current state of the art of direct reduction based on natural gas to direct reduction based on hydrogen as a central decarbonization path. A complete conversion of Germany's primary steel production of 30 million tons (time frame 2050) would require around two million tons (70 TW h) of hydrogen but could save approximately 50 million tons of carbon dioxide. That is equivalent to a reduction of roughly 28 tons carbon dioxide per ton of hydrogen used. Strategy documents for Hamburg envisage that between roughly 30% and 80% of the natural gas used in the metal industry could gradually be replaced by green hydrogen from around 2030 onwards, to a total replacement by 2045, provided that sufficient hydrogen is available at competitive cost. The chemical industry is also dependent on hydrogen. According to the Hydrogen Action Plan, the current demand for hydrogen is 1.1 million tons (37 TW h) with most of the hydrogen obtained from natural gas via steam reforming (gray hydrogen). Replacing this fossil-based hydrogen with green hydrogen represents another important lever for decarbonization [1, 3].

[1] ArcelorMittal has suspended its plans for climate-friendly steel production at its sites in Bremen and Eisenhüttenstadt due to limited hydrogen availability and lacking economic viability. The planned switch to green steel production in Hamburg may likewise be postponed by several years [7]. This underlines the importance of a timely build-up of hydrogen production and infrastructure.

Hamburg's hydrogen import strategy further quantifies this future relevance of green hydrogen. Based on surveys of major industrial consumers in Hamburg, it is anticipated that by 2030 around 5.7 TW h of green hydrogen per year will be needed only in the industrial sector, with an additional 1.9 TW h per year for mobility applications directly related to port logistics. In total, this corresponds to a projected local demand of approximately 7.6 TW h of green hydrogen per year by 2030. At the same time, Hamburg's current project pipeline foresees an electrolysis capacity of approximately 550 MW by 2030, equivalent to roughly 2.2 TW h of annual hydrogen production. The difference between demand and local production can neither be closed by Hamburg nor by Germany as a whole, even under ambitious expansion scenarios for renewables and electrolyzer. As a result, Hamburg expects to depend on substantial hydrogen imports and aims to position itself as a central hub for the handling and distribution of green hydrogen in Northern Europe - with the green hydrogen project in Moorburg as an essential starting point. [6].

At the site of the former coal-fired power plant in Moorburg, Hamburg has begun a redevelopment into a Green Energy Hub. The transformation of the coal power plant into the HGHH with an initial 100 MW electrolyzer demonstrates in a concrete form how fossil infrastructure can be repurposed to support a climate-neutral energy system [8].

With this advance into green hydrogen an understanding of the complete hydrogen energy system becomes essential. The Hydrogen Square model developed by Dawood et al. [9] illustrates the interconnectedness of production, utilization, storage, safety and subsystems to condition the hydrogen.

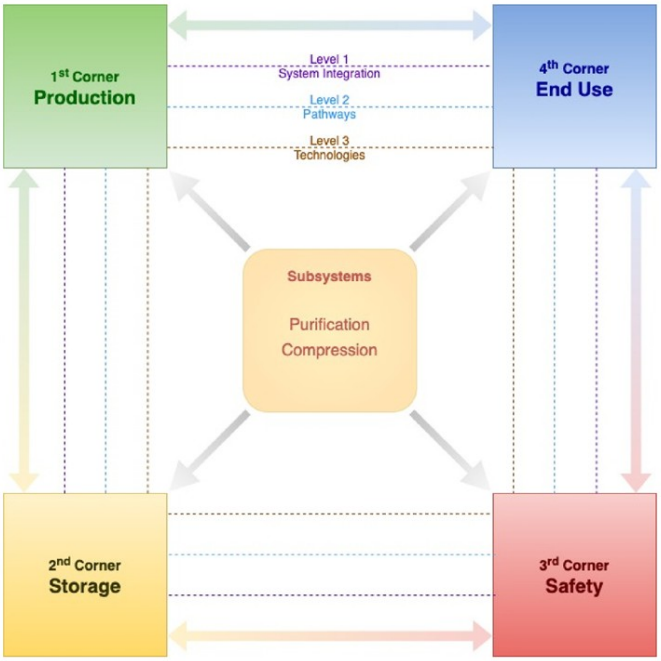

Figure 1.1: Hydrogen Square with the four stages of the hydrogen economy [9, 10]

Central to this interconnected system is hydrogen itself, which makes understanding its unique physical and chemical properties imperative.

Hydrogen is classified using a color code depending on the production process respectively the type of energy source used for production and associated greenhouse-gas emissions. The most important variants in the context of decarbonization strategies are:

- Gray hydrogen: Production through steam reforming of natural gas with the resulting CO_2 released into the atmosphere. In 2022, natural gas reforming accounted for 96% of Europe's hydrogen production, with associated worldwide CO_2 emissions of approximately 830 Mt/a. [11, 12, 13]
- Blue hydrogen: Production through steam reforming of natural gas, with subsequent carbon capture and storage (CCS). This significantly reduces, but not fully eliminates CO_2, providing the captured CO_2 is stored permanently. [11, 12]
- Turquoise hydrogen: Production via methane pyrolysis of natural gas, generating solid carbon instead of CO_2. The overall climate balance depends on methane leakage and carbon handling.

- Green hydrogen: Produced by water electrolysis powered by renewable electricity, with no process-related CO_2 emissions (carbon-free). [11, 12]

From the perspective of Hamburg's long-term climate targets, the green hydrogen is the decisive option, because it permits far-reaching decarbonization without continued fossil fuel dependence.

Hydrogen's physical properties strongly influence how it can be stored, transported and used. Under standard conditions (0 °C, 1,013 bar), hydrogen is the lightest of all elements, with a density of only about 0.089 kg/m^3. Its lower heating value is approximately 120 MJ/kg (around 33 kW h/kg), compared to conventional fuels (13.9 kW h/kg for natural gas, 12.4 kW h/kg for liquid hydrocarbons) means a very high gravimetric energy density compared to conventional fuels. However, due to its low density, the volumetric energy density of hydrogen gas at ambient pressure is only 9.9 MJ/m^3 (around 0.003 kW h/L), significantly lower than conventional fuels (0.08 kWh/L for natural gas, 10.5 kW h/L for liquid hydrocarbons). Hydrogen is therefore an excellent energy carrier per unit of mass, but a very poor one per unit of volume. This poses a problem for the utilization of hydrogen as practical applications under standard conditions are virtually impossible [10, 14, 15].

For practical applications in storage, transport, and further utilization, hydrogen must be conditioned to increase its volumetric energy density. Two approaches dominate as traditional and therefore commonly used:

- Mechanical compression: Hydrogen is compressed to elevated pressures. In pipeline transport, pressures in the range of several tens of bar are common [16], while pressures go up up to 700 bar in fuel cell vehicles [17]. While mechanical compressors are the well-established standard in current hydrogen infrastructure, they face several fundamental technical challenges, illustrated by the fact, that mechanical compressors in refueling stations are "the second largest contributor in the maintenance hours (24%) and frequency of incidents (18%)" [18]. Moving parts in the complex designs introducing wear, noise emission and vibrations, resulting in substantial maintenance requirements, especially in dynamic operation, as well as the necessity for significant electrical energy input. [19, 20, 21]

- Liquefaction: Hydrogen is cooled to its boiling point at -253 °C and stored as a cryogenic liquid. This dramatically increases volumetric energy density up to 1.2 kW h/L but requires high energy input for liquefaction (around 30% of the hydrogen's stored energy content) and continuous refrigeration, as well as sophisticated cryogenic infrastructure. Furthermore, evaporation losses of between 0.3% and 3% per day occur [14, 10].

The technical and energetic limitations of these conventional approaches motivate research into alternative concepts, such as hydrogen storage and compression using metal hydrides. These materials can absorb hydrogen at moderate pressures and release it again at higher pressures, potentially enabling more compact, reliable, quiet and safe compression cycles for specific applications. In the context of Hamburg's planned large-scale hydrogen infrastructure and the high and fluctuating volume flows it must handle, such alternative compression technologies are a promising field of investigation.[20, 22, 23]

1.2 Thesis Outline

The aim of this thesis is to investigate and evaluate the suitability of a MHC as a viable alternative to the mechanical compressors currently planned for the HGHH. By utilizing thermal energy, such as the waste heat from the electrolyzer, to drive the compression process without moving parts, metal hydride technology directly addresses some the fundamental limitations of conventional compression described above.[20, 22, 23]

The following specific questions guide this investigation:

- Which metal hydrides are suitable for operation within the temperature and pressure boundary conditions at HGHH, either covering the full pressure range or within sub-ranges?
- Is a multi-stage arrangement necessary to achieve the required compression ratio and subsequently sufficient productivity, and which combination of metal hydrides is best suited for such a configuration? To what extent can key operating and design parameters, including heating and cooling temperatures, alloy mass, cycle time and compressor dimensions be optimized regarding productivity and specific energy consumption and what values are achievable within the feasible and realistic operating range?

- What are the resulting compressor dimensions and required alloy mass of a MHC scaled to the full hydrogen output of the 100 MW electrolyzer at Moorburg and how does it compare to a mechanical compressor?
- How do the thermal energy requirements of the scaled MHC system compare to the waste heat available at the HGHH site in terms of temperature level and thermal power, and what measures, e.g. the consideration of alternative electrolyzer technologies with other operating temperature levels, could address potential deficits?
- From both a systemic and energetic perspective, which advantages of the MHC approach, such as a potentially more compact design, or the direct utilization of waste heat, remain relevant under the given boundary conditions compared to conventional mechanical compression?

To address these questions and evaluated the technology, a validated dynamic simulation model in ACM is utilized. This model simulates the absorption and desorption cycles of the MHC to determine optimal operating conditions through productivity and energy consumption and derive key operating and design parameters under realistic system constraints.

This analysis is carried out in direct collaboration with the HGHH, which is establishing commercial hydrogen production at the former Moorburg coal power plant with a 100 MW electrolyzer scheduled for grid connection in 2027. By using site-specific boundary conditions such as available waste heat temperature levels and hydrogen output profiles, this work seeks to quantify whether a MHC system can offer a technically robust and energetically competitive advantage for large-scale industrial hydrogen hubs as an alternative to the planned mechanical infrastructure.

2 Fundamentals and State of the Art

This chapter establishes the theoretical and technical foundation necessary to understand the investigation conducted in this thesis. Three subject areas are covered in sequence, each directly relevant to the development and subsequent evaluation of a MHC as an alternative to mechanical hydrogen compression.

The first section addresses the upstream water electrolysis process, which determines the pressure and purity of the hydrogen feed as well as the temperature and quantity of available waste heat, both critical boundary conditions for the thermal integration of the MHC. Four electrolyzer technologies are therefore described and compared with regard to their suitability for large-scale hydrogen production and compatibility with downstream metal hydride compression.

The second section covers conventional mechanical hydrogen compression to benchmark against the MHC developed in this work. The underlying thermodynamic principles of compression are presented, followed by an overview of available compressor types and a discussion of those relevant to large-scale hydrogen service.

The third section introduces the operating principle of metal hydrides. It covers the thermodynamic and kinetic fundamentals governing hydrogen absorption and desorption, and provides an overview of hydride materials relevant to thermally driven compression, forming the theoretical basis for the subsequent alloy selection and compressor development.

2.1 Electrolyzer Technologies for Green Hydrogen Production

Since the metal hydride compressor is intended to operate as part of a larger hydrogen production and distribution chain, an understanding of the upstream water electrolysis process is essential. The type of electrolyzer used determines not only the pressure and purity of the hydrogen feed, but also temperature and quantity of the available waste heat, both of which are critical boundary conditions for the thermal integration of the MHC.

Water electrolysis is the electrochemical splitting of water into hydrogen and oxygen through the application of electrical energy, effectively converting electrical energy into chemical energy stored in the molecular hydrogen produced. This conversion takes place within electrolytic cells, that combines two electrode half-reactions with ion transport through an electrolyte while maintaining physical separation of the product gases. Individual cells are assembled into stacks to form an electrolyzer unit. [12] The overall electrolysis reaction is given by:

$$2\,H_2O\,(l) \rightleftharpoons 2\,H_2(g) + O_2(g) \tag{2.1}$$

Without electrical input, this reaction requires temperatures in excess of approximately 2500°C to proceed spontaneously. In an electrolyzer, the minimum theoretical cell voltage required to drive this reaction is the reversible cell voltage E^0_{rev} of 1.229 V at standard conditions. Since the reversible cell voltage is temperature dependent, this theoretical minimum differs between electrolyzer technologies operating under different conditions [24]. High-temperature technologies benefit from a significantly reduced reversible cell voltage of approximately 0.8 - 2.0 V, as a portion of the energy demand is supplied thermally rather than electrically. In practice, the applied cell voltage must exceed not only the reversible voltage but also the thermoneutral voltage E^0_{tn} (1.481 V at standard conditions) above which the reaction becomes exothermic. The practical cell voltages of all electrolyzer technologies therefore significantly exceed the reversible cell voltage, as additional losses arise from activation overpotentials at both electrodes and ohmic resistances within the cell components [24, 12, 25], as summarized in Table 2.1.

Within the electrolyzer stack, heat is generated as a consequence of both the thermodynamic irreversibility of the electrochemical reactions and the ohmic resistance of the cell components. At the thermoneutral voltage E^0_{tn}, the reaction proceeds adiabatically, neither consuming nor releasing heat, however, the resulting reaction kinetics are insufficient to sustain meaningful hydrogen production. In practice, therefore, a cell voltage above the thermoneutral voltage E^0_{tn} is applied to achieve adequate reaction rates, rendering the electrolysis process exothermic and necessitating active thermal management. The resulting heat output $Q_{produced}$ is given by [25]:

$$Q_{produced} = I \cdot (U_{operating} - U_{thermoneutral}) \tag{2.2}$$

where I is the cell current, $U_{operating}$ the applied cell voltage, and $U_{thermoneutral}$ the thermoneutral voltage. If this heat is not offset by the energy consumed in water evaporation within the stack, it must be actively removed to maintain safe operating temperatures. In a e.g. Proton Exchange Membrane Electrolysis/Polymer Electrolyte Membrane Electrolysis (PEM), waste heat can be recovered from three process streams: the oxygen outlet, the hydrogen outlet, and the water recirculation loop. [25]

Several electrolyzer technologies are currently under development or in commercial deployment, including Alkaline Electrolysis (AEL), Polymer Electrolyte Membrane/Proton Exchange Electrolysis (PEM/PEMEL), Solid Oxide Electrolysis (SOEL), and Anion Exchange Membrane Electrolysis (AEM/AEMEL). [26, 12, 27]

A comparative overview of these technologies is provided in Table 2.1, with further descriptions given in the following paragraphs. The overview focuses particularly on characteristics relevant to renewable energy integration and compatibility with downstream metal hydride compression systems.

Table 2.1: Technology comparison of electrolyzer types [27, 13, 26, 28, 11, 29, 30, 31, 32]

Specification	**Alkaline**	**AEM**	**PEM**	**SOEL**
Technology readiness level	Mature	Under development	Commercialized	Under development
Working temperature (°C)	≤ 90	≤ 60	≤ 80	≤ 1000
Operating pressure (bar)	≤ 30	≤ 35	≤ 70	30
Cell voltage (V)	1.8 – 2.4	1.4 – 2	1.8 – 2.2	0.8 – 2
Current density (A/cm^2)	0.2 – 0.5	0.2 – 1	0.8 – 3	0.3 – 3.9
Electrolyte	Strong alkaline	Diluted alkaline	Water	Steam (water)
Separator	Diaphragm	AEM	PEM	Solid ceramic separator
Anode	Ni, NiCo alloys	Ni, Fe, Co	RuO_2, IrO_2	Ni-YSZ
Cathode	Ni, NiMo alloys	Ni, Ni alloys	Pt, PtPd	LSM-YSZ
Hydrogen purity (%)	≤ 99.5	99.99	99.999	99.9
Cell efficiency, HHV (%)	50 – 80	52 – 67	50 – 83	80 – 100
Spec. energy cons. (kWh/Nm^3)	4.5 – 7.5	4.8 – 5.2	5.8 – 7.5	2.5 – 3.5
Stack lifetime (h)	60k – 100k	15k	20k – 60k	20k – 40k
Response time	Minutes	Seconds	Milliseconds	Unknown
Advantages	Mature technology, non-precious metals (low cost)	Non-precious metals, less corrosive electrolyte	High current densities, high gas purity	High efficiency, high temperature
Disadvantages	Limited current densities, corrosive electrolyte	Limited stability, under development	Precious metal catalysts, acidic electrolyte	Limited stability, high cost

Higher Heating Value (HHV); YSZ: Yttria-stabilized zirconium; LSM: La, Sr, Mn

The technical parameters compiled in Table 2.1 provide the basis for evaluating the suitability of each electrolyzer technology for integration with renewable energy systems and for their potential role as a waste heat source for metal hydride compressor operation, as relevant to the scope of this work. It must be noted that all values presented are sourced from the scientific literature and represent approximate reference ranges only. Actual system performance may deviate above or below the stated ranges depending on the manufacturer, operating conditions, plant scale, and the current state of technological development. This caveat applies in particular to parameters for which the literature shows significant variation, most notably the achievable hydrogen purity. Reaching the commercial hydrogen quality of grade 5.0 ($\geq$ 99.999 mol%) typically requires additional purification steps beyond the electrolyzer itself, as illustrated by the electrolyzer system configuration in Moorburg, described in the Section 3.2.1.

AEL and PEM currently represent the most commercially and technically mature electrolyzer technologies, well-established as technologies in worldwide hydrogen production plants. AEM and SOEL, by contrast, remain at comparatively early stages of commercial development, with ongoing research efforts directed toward improving long-term stability, lifetime, and cost competitiveness [28, 26, 11, 27, 13].

Solid Oxide Electrolysis (SOEL):

SOEL distinguishes itself from the remaining technologies through its significantly elevated operating temperatures, which can reach several hundred degrees Celsius, being well above the operating temperature range of AEL, PEM and AEM, which typically not exceed 100°C. While these high temperatures enhance thermodynamic efficiency and promote favorable reaction kinetics, economically viable operation is contingent on access to external industrial waste heat sources to meet the thermal energy demand, such as those available in chemical or metallurgical industries. From the perspective of this work, the operating temperatures of SOEL substantially exceed those required by metal hydride compressor processes (see Section 2.3.2), rendering direct thermal integration impractical. Combined with the technology's status as still under development to solve challenges such as accelerated material degradation resulting from the prolonged exposure to high temperatures, a detailed treatment of SOEL is therefore excluded from the further analysis conducted in this work. [27, 26, 33, 28, 34].

Alkaline Electrolysis (AEL):

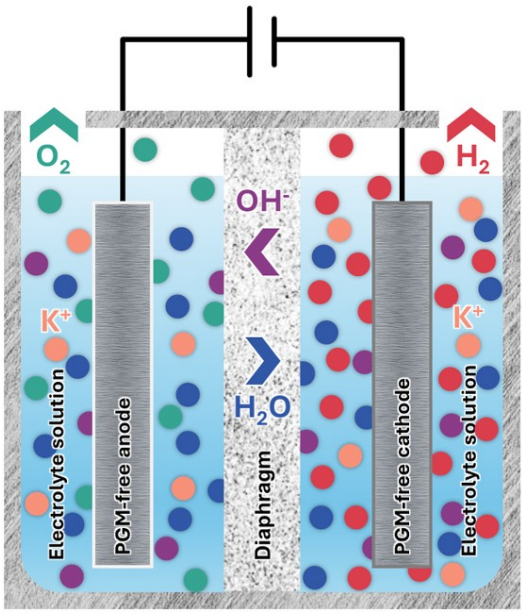

Figure 2.1: Schematic of the working principle of AEL [13]

Alkaline water electrolysis (AEL) is the most mature and well-established low-temperature electrolyzer technology, typically operated at temperatures between 50 and 80°C and pressures up to 30 bar. Figure 2.1 illustrates the schematic working principle of AEL in a conventional gapped-cell configuration, in which a finite gap between the electrodes and the diaphragm is filled with electrolyte. This configuration contributes to elevated ohmic losses, which manifest as comparatively high cell voltages, as reflected in Table 2.1. In more recent zero-gap designs, the electrodes are pressed directly onto the diaphragm to minimize the electrolyte path length and thereby reduce ohmic resistances. [29, 31, 26, 13, 27, 28, 30]

The electrolyte most commonly employed is an aqueous potassium hydroxide (KOH) solution at a concentration of 30 to 40 wt%. Electrodes are generally composed of non-precious metals, typically nickel or nickel-based alloys coated with electrocatalytic layers, offering a cost advantage over noble-metal systems. The anode and cathode compartments are separated by a diaphragm permeable to hydroxide ions (OH^-), which serve as the charge carrier in the alkaline system. [29, 31, 26, 13, 27, 28] The electrode half-reactions and the overall cell reaction are given by:

$$Cathode : 2\,H_2O(l) + 2\,e^- \longrightarrow H_2(g) + 2\,OH^-(aq) \tag{2.3}$$

$$Anode : 2\,OH^-(aq) \longrightarrow 0.5\,O_2(g) + H_2O(l) + 2\,e^- \tag{2.4}$$

$$OverallReaction : 2\,H_2O(l) \longrightarrow 2\,H_2(g) + O_2(g) \tag{2.5}$$

At the cathode, water is reduced to hydrogen and hydroxide ions, which migrate through the diaphragm toward the anode, where they are oxidized to oxygen and water. The overall reaction yields hydrogen and oxygen in a molar ratio of 2:1. Compared to other low-temperature technologies, AEL operates at relatively low current densities, typically between 0.2 and 0.5 A/cm^2, resulting in lower hydrogen production per unit active area. This is primarily attributed to the limited mobility of (OH^-) ions through the liquid electrolyte and the diaphragm. [29, 31, 26, 13, 27, 28]

Following the electrolysis cell, the two-phase mixture of electrolyte and product gas is directed to gas separators to split up the phases. A typical AEL stack achieves a system efficiency of approximately 70% with capacities reaching up to 6 MW per stack, making it well-suited for large-scale hydrogen production. The generated hydrogen can achieve purities of up to 99.5 vol%, with trace impurities arising primarily from gas crossover through the diaphragm and backmixing following gas separation. Gas crossover is particularly pronounced during partial-load operation, where reduced current densities increase the relative permeation of product gases through the diaphragm. As gas impurities above 2 vol% pose an explosion hazard, maintaining impurity concentrations below this safety threshold is crucial to avoid emergency shutdowns and ensure stable operation. An additional limitation is the potential for salt precipitation within the electrolyte circuit, which can foul cell components and degrade long-term performance.[29, 31, 26, 13, 27, 28]

Dynamic operation, as the use of renewable energy entails, exacerbates some of these challenges. The slow ion transport due to the liquid electrolyte and diaphragm results in sluggish electrochemical response and start-up times on the order of minutes, limiting the system's ability to follow fluctuating power inputs. Frequent partial-load operation promotes increased gas crossover through the diaphragm, raising the risk of triggering frequent emergency shutdowns.

Each shutdown–restart cycle subjects the electrodes to repeated thermal and electrochemical stress, leading to accelerated degradation of the electrodes. [29, 31, 26, 13, 27, 28]

Although AEL systems benefit from their technological maturity and the use of non-noble metal electrodes, which contribute to comparatively low capital costs, their limited partial-load operating range of 10–25% of nominal power, inherent sensitivity to dynamic load changes, the sluggish response time and comparatively low current densities remain fundamental constraints for renewable energy integration. [29, 31, 26, 13, 27, 28]

Proton Exchange Membrane Electrolysis/Polymer Electrolyte Membrane Electrolysis (PEM/PEMEL):

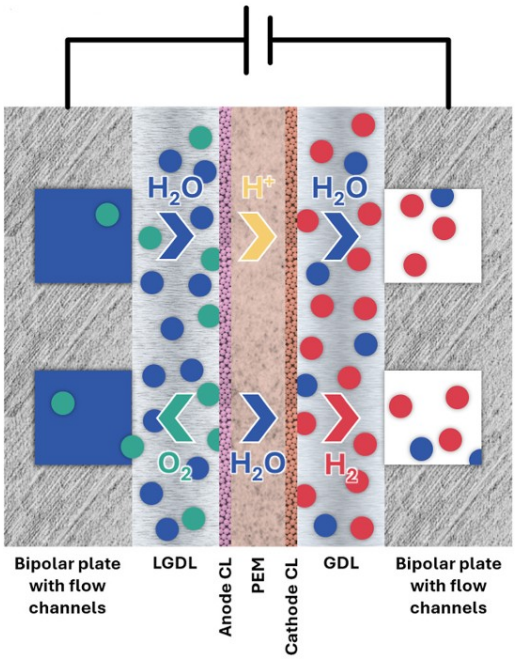

Figure 2.2: Schematic of the working principle of PEM [13]

Proton Exchange Membrane Electrolysis (PEM) is a comparatively newer yet commercially mature low-temperature electrolyzer technology, typically operated at temperatures up to 80°C and pressures up to 70 bar. Figure 2.2 illustrates the schematic working principle of PEM.

The technology employs a humidified, proton-conducting solid polymer membrane as both the electrolyte and the electrode separator, requiring only deionized water as feed without the need for a liquid electrolyte. The thin membrane enables high proton conductivity and fast proton transport, which, combined with the direct coating of electrodes onto the membrane surface to minimize ohmic losses and allows PEM to achieve significantly higher current densities of 0.8 to 3 A/cm^2 resulting in a higher hydrogen production per unit active area. [12, 27, 11, 31, 13, 30, 29]

Due to the strongly acidic environment (pH ~ 2) generated by the proton-conducting membrane and the high potentials imposed during high current density operation, electrode materials must exhibit both chemical stability and electrochemical durability under these conditions. This necessitates the use of precious metal catalysts, such as platinum at the cathode and iridium oxide at the anode. The necessity of these materials is a significant driver of overall system cost, with Iridium being a particularly scarce and costly element [12, 27, 11, 31, 13, 30, 29, 24] The electrode half-reactions and the overall cell reaction are given by:

$$Cathode : 4\,H^+ + 4\,e^- \longrightarrow 2\,H_2(g) \tag{2.6}$$

$$Anode : 2\,H_2O(l) \longrightarrow O_2(g) + 4\,H^+ + 4\,e^- \tag{2.7}$$

$$OverallReaction : 2\,H_2O(l) \longrightarrow 2\,H_2(g) + O_2(g) \tag{2.8}$$

At the anode, water is oxidized to oxygen, protons, and electrons. The protons migrate through the membrane and recombine with electrons at the cathode to form hydrogen. A notable operational characteristic of PEM is the ability to maintain elevated pressure on the cathode side while operating the anode at near-atmospheric pressure, enabling the direct production of compressed hydrogen without additional mechanical compression. [12, 27, 11, 31, 13, 30, 29]

Similar to AEL, the product hydrogen contains water vapor and trace quantities of oxygen arising from membrane crossover, particularly at reduced load. However, residual oxygen can often be catalytically recombined at the cathode, resulting in comparatively low oxygen contamination and achievable hydrogen purities of up to

99.999 vol%. Stack efficiencies are typically around 70%, and the technology is well-suited to large-scale applications. As of 2020, the then-largest PEM hydrogen production facility comprised four 5 MW electrolysis units. [12, 27, 11, 31, 13, 30, 29]

A key advantage of PEM over AEL is its suitability for dynamic operation. The absence of a liquid electrolyte and the fast proton transport through the solid membrane yield rapid electrochemical response and start-up times on the order of milliseconds. The partial-load operating range extends down to approximately 5% of nominal capacity, rendering PEM substantially more tolerant of the intermittent and fluctuating power inputs associated with renewable energy sources. These characteristics, combined with high current densities, the absence of a corrosive liquid electrolyte and the high achievable hydrogen purity, make PEM well-suited for integration with renewable energy systems and downstream metal hydride compression. The primary limitation of the technology remains its high capital cost, driven largely by the requirement for scarce precious metal catalysts. [27, 35, 31, 13, 11, 30, 12, 26, 29, 24]

Anion Exchange Membrane Electrolysis (AEM/AEMEL):

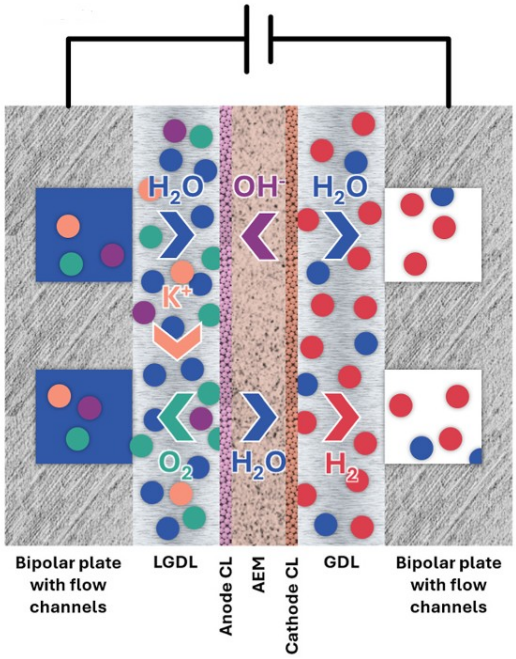

Figure 2.3: Schematic of the working principle of AEM [13]

Anion Exchange Membrane Electrolysis represents a comparatively recent electrolyzer technology, currently still under development, with commercial models already available but with limited long-term operational data. It is conceptually positioned as a middle ground between AEL and PEM, combining the alkaline operating environment of AEL with the solid-state membrane of PEM. The technology operates at temperatures up to 60°C and pressures up to 35 bar. Figure 2.3 illustrates the schematic working principle of AEM. [33, 13, 36]

The core component is a solid anion exchange membrane (AEM), which conducts hydroxide ions (OH^-) from the cathode to the anode while physically separating the product gases. The environment within the membrane is inherently alkaline, therefore demineralized water could be used as sole feed stream, eliminating the need for a liquid alkaline electrolyte. However, current technology exhibits improved performance and durability when a dilute alkaline electrolyte feed is employed. The technology is furthermore compatible with moderate-purity water feed streams, making the technology suitable for decentralized systems in developing countries. [26, 36, 37, 33, 28, 13]

The alkaline operating conditions permit the use of non-precious metal catalysts, most commonly nickel and nickel-based alloys, analogous to AEL, representing a significant cost advantage over PEM. [37, 33] The electrode half-reactions and the overall cell reaction are given by:

$$Cathode : 2\,H_2O + 2\,e^- \longrightarrow H_2 + 2\,OH^- \tag{2.9}$$

$$Anode : 2\,OH^- \longrightarrow H_2O + 0.5\,O_2 + 2\,e^- \tag{2.10}$$

$$OverallReaction : 2\,H_2O(l) \longrightarrow 2\,H_2(g) + O_2(g) \tag{2.11}$$

Water is supplied at the cathode, where it is reduced to hydrogen and hydroxide ions. The hydroxide ions migrate through the membrane toward the anode, driven by the electrochemical potential gradient, where they are oxidized to oxygen and water. The solid membrane facilitates differential pressure operation and supports higher current densities than conventional AEL, increasing hydrogen output per unit active area. [26, 36, 37, 33, 28]

Despite the advantages of a low-cost, optimized system as a middle-ground technology between AEL and PEM, AEM currently faces several critical limitations that constrain its near-term applicability. The technology suffers from durability challenges associated to insufficient chemical and thermal stability of the anion exchange membrane, including low ionic conductivity under operational load, susceptibility to chemical degradation under varying current density conditions, and comparatively short membrane lifespans. These factors result in limited stack lifetimes, as reflected in Table 2.1, and overall system efficiencies that remain lower than those of both AEL and PEM at equivalent operating conditions. Another drawback for this specific use-case is the low operating temperature. Whether around 60°C are enough to supply a MHC is to be considered. In conclusion, AEM is an emerging technology with considerable long-term potential, though further advances in research and development are necessary before it can be considered technically mature for large-scale application. [24, 33, 28, 27, 13]

Technology Assessment

Of the electrolyzer technologies presented, Alkaline Electrolysis (AEL) and PEM emerge as the most relevant for the scope of this work. Both are commercially mature, widely deployed in large-scale hydrogen production, and operate within temperature ranges compatible with the thermal requirements of metal hydride compression. PEM is of particular interest due to its superior dynamic response and suitability for fluctuating renewable energy input. Solid Oxide Electrolysis (SOEL) is excluded from further consideration, as its operating temperatures substantially exceed those required by the metal hydride compression process and its limited technological maturity. Anion Exchange Membrane Electrolysis (AEM), while not yet sufficiently mature for large-scale deployment and limited long-term stability data, represents a promising emerging technology.

2.2 Mechanical Compression

The compression of hydrogen is a critical process step, bridging production, gas processing and distribution. Selecting a suitable compression technology for a hydrogen application is constrained by the requirements on hydrogen compatibility, the ability to handle a volumetric throughput on an industrial scale and the capacity to deliver outlet pressures sufficient for pipeline injection (achievable pressure ratio). The technologies available for hydrogen compression are either mechanical or non-mechanical technologies. Since mechanical compression is currently the better known and therefore more widely used compression method, the fundamentals on this technology are presented in the following section. [18, 21, 20]

2.2.1 Thermodynamics of Mechanical Compression

The theory of compression and therefore the operation of mechanical compressors is governed by thermodynamics, specifically the relationship between pressure, volume, and temperature when mechanical work is added. Real compression in engineering practice is commonly modeled as a polytropic process, expressed by $p_1 V_1^n = p_2 V_2^n$, because heat transfer during compression is neither perfectly prevented nor perfectly removed. The polytropic index n characterizes the compression path. Values closer to 1 indicate stronger heat removal, so closer to isothermal behavior, while values closer to $\gamma = c_p/c_v$ indicate weaker heat removal, which is closer to adiabatic behavior. [38]

There are two limiting cases to the polytropic compression, used as a reference and for defining efficiencies. Isothermal compression (n=1, $p_1 V_1 = p_2 V_2 = const.$is the theoretical minimum-work path because the gas temperature is held constant by perfectly effective cooling, a condition that cannot be achieved exactly in a real machine but can be approached by staging and inter-cooling. Isentropic compression ($n = \gamma$, $p_1 V_1^\gamma = p_2 V_2^\gamma$), represents a reversible adiabatic limit with no heat transfer, leading to a larger temperature rise for a given pressure ratio and therefore higher required work than the isothermal case [38].

The energy requirement of compression can be interpreted on a pressure–volume (p-V)-diagram. The work input is associated with the area under the compression curve, which is why the chosen thermodynamic path or case directly affects power consumption. The theoretical work for each case can be calculated as follows [39, 38]:

$$W_{isen} = \frac{\gamma P_1 V_i}{\gamma - 1}\left[\left(\frac{P_2}{P_1}\right)^{\frac{\gamma-1}{\gamma}} - 1\right], \qquad \text{Isentropic work} \tag{2.12}$$

$$W_p = \frac{nP_1 V_i}{n - 1}\left[\left(\frac{P_2}{P_1}\right)^{\frac{n-1}{n}} - 1\right], \qquad \text{Polytropic work} \tag{2.13}$$

$$W_{iso} = P_1 V_i \ln\left(\frac{P_2}{P_1}\right), \qquad \text{Isothermal work} \tag{2.14}$$

with γ being the ratio of the specific heat (isentropic exponent) and n being the polytropic index.

A pV-diagram provides a graphical representation of the thermodynamic cycle experienced by the gas within a positive-displacement compressor. [38, 40]

The cycle begins at State 1, where the compressor chamber is filled with gas at the suction pressure P_1. During the compression phase (State 1 -> State 2), the chamber volume decreases while the gas pressure rises from P_1 to the discharge pressure P_2. This compression path is represented by different curves on the diagram, depending on isothermal, polytropic, or isentropic compression. [38, 40]

Once maximum pressure is reached at State 2, the discharge phase begins. The compressed gas is expelled from the chamber, and the volume continues to decrease until it reaches the a minimum value, known as the clearance volume V_c (State 3). This clearance volume is unavoidable in real machines due to geometric constraints. The piston cannot physically contact the cylinder head.[38, 40]

The trapped high-pressure gas in the clearance volume then undergoes re-expansion (State 3 -> State 4) as the chamber volume begins to increase again. During this phase, the pressure of the remaining gas drops from P_2 back toward P_1, but no fresh gas enters yet because the internal pressure is still too high. Only when the pressure falls sufficiently below the suction line pressure does the inlet valve open. [38, 40]

Finally, the suction phase (State 4 -> State 1) occurs, during which new gas at pressure P_1 flows into the expanding chamber, refilling it to the full volume and returning the system to State 1 to repeat the cycle. The area enclosed by this four-stage cycle on the pV-diagram represents the net work input required per cycle. [38, 40]

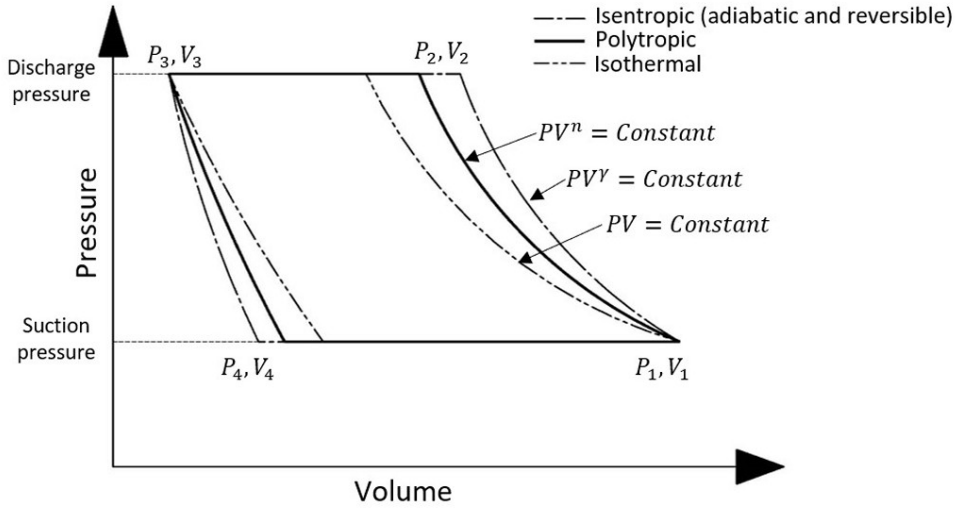

Figure 2.4: Theoretical pV-diagram [39]

Isothermal compression (const. temperature) represents the theoretical ideal for energy efficiency. It assumes that the heat generated during compression is removed instantaneously, keeping the gas temperature constant throughout the process. On the pV-diagram, this curve has the lowest slope and encloses the smallest area, representing the minimum possible work required to compress a gas from pressure P_1 to P_2. Achieving this would require infinite cooling capacity, making it impossible in practice, though multi-stage compressors with inter-coolers attempt to approximate this curve to reduce energy consumption. [38]

Isentropic (Adiabatic) compression represents a reversible process with zero heat transfer to the surroundings. All mechanical energy input is converted into internal energy, causing a maximum rise in gas temperature. On the pV-diagram, this curve is the steepest and encloses the largest area, representing the maximum work input for a reversible process. This case is often used as a reference to calculate the isentropic efficiency of dynamic compressors. [38, 41]

Polytropic compression ($1 < n < \gamma$) represents the actual process in a real mechanical compressor. Real machines are neither perfectly cooled, like in the isothermal process, nor perfectly insulated, like in the isentropic process. There is some heat loss to the, i.e., cylinder walls, but not enough to maintain a constant temperature. The polytropic curve lies between the isothermal and isentropic limits on the pV-diagram.

The value of the polytropic index n indicates the effectiveness of the cooling system with a lower n, closer to 1, implying better cooling and higher efficiency. [38, 39, 41, 41]

2.2.2 Mechanical Compressor Types

The goal of any (mechanical) compressor is to increase the pressure of a gas, a process that requires work input and generates heat. While these underlying thermodynamic principles, illustrated in Subsection 2.2.1, remain consistent across all compressor types, their mechanical designs differ substantially, making them suited for varying applications.

The following table 2.2.2 provides an overview of established types within both categories, identifies those unsuitable for large-scale hydrogen compression, and characterizes the remaining candidates as a reference basis for benchmarking against the metal hydride compressor developed in this work.

- **Positive Displacement Compressor**
  - **Reciprocating Displacement Compressor**
    - Piston Compressor
    - Diaphragm Compressor
    - Ionic Liquid Piston Compressor
  - **Rotary Displacement Compressor**
    - Screw Compressor
    - Scroll Compressor
    - Sliding/Rotary Vane Compressor
    - Liquid Ring Compressor
    - Roots Compressor
- **Dynamic Compressor / Turbomachinery**
  - **Turbo Compressor**
    - Centrifugal / Radial Compressor
    - Axial Compressor

Based on their operating principle, mechanical compressors are divided into two main categories: positive displacement compressors and turbomachinery. [39, 38, 21, 42, 43, 44]

Positive displacement compressors operate by capturing a fixed volume of gas and mechanically reducing that volume, for example by means of a piston, thereby raising the pressure. This category is further divided into reciprocating compressors, in which the volume reduction is achieved by a linearly oscillating element, and rotary displacement compressors, in which rotating elements fulfill the same function. [39, 38, 21, 42, 43, 44]

The second main category, turbomachinery, colloquially known as "dynamic", comprises compressors that transfer kinetic energy to the gas via a rotating impeller and subsequently convert that energy into pressure in a diffuser. Unlike positive displacement compressors, turbomachinery operates on a continuous flow principle. [39, 38, 21, 42, 43, 44]

Of the compressor types listed above, several can be excluded from consideration on the listed requirements hydrogen compatibility, throughput capacity, and achievable compression ratios and ranges. A review of the literature on hydrogen compression after production and in pipeline applications consistently identifies reciprocating piston compressors, diaphragm compressors, ionic liquid piston compressors, centrifugal compressors, screw compressors and liquid ring compressors as the primary candidates discussed and evaluated in the context of hydrogen applications [21, 20, 45, 46, 47]. The remaining types from the classification above, namely scroll compressors, sliding/rotary vane compressors, roots compressors, and axial compressors, are in principle capable of handling hydrogen but are confined to operating ranges that fall outside the requirements of this work and are therefore excluded from further consideration.

Rotary Displacement Compressors:

Scroll, sliding/rotary vane, and roots compressors have been demonstrated in hydrogen service, but their application is focused on the recirculation of unreacted hydrogen of PEM fuel cells in fuel cell vehicles, with a low flow rate and low pressure ratio. While higher flow rates are available for e.g. roots compressor, the achievable outlet pressures remain insufficient for pipeline injection.[48, 49, 50, 51, 52, 53, 54]

Liquid ring compressors operate by means of an eccentrically mounted impeller that forces the operating liquid into a rotating ring, which compresses the gas introduced at the rotor center. This design is particularly suited to vacuum applications and the handling of saturated or contaminated gas streams, but achieves an overall efficiency of only approximately 50%. The scientific literature on the use of liquid ring compressors in pure hydrogen applications is scarce, reflecting the limited suitability of this technology for such service. Although liquid ring compressors are commercially available for green hydrogen gas streams at flow rates up to 20,000 m^3/h, the achievable discharge pressure is limited to approximately 8 bar, far below the pipeline injection pressures required in this work. Liquid ring compressors are therefore not considered further in this work [55, 21, 56].

Rotary screw compressors operate by capturing gas in the space between two parallel interlocking screws that rotate relative to each other and to the casing. The inherent rotor clearances, combined with hydrogen's low molar mass and viscosity, result in significantly higher backflow through the gaps compared to heavier gases, reducing efficiency. Oil- or water-injected variants mitigate this through improved sealing (while cooling simultaneously) but require downstream gas purification, while dry-running oil-free variants avoid contamination but are rarely applied where significant pressure ratios are needed, as sufficiently tight tolerances to limit hydrogen leakage are difficult to achieve. This leakage limits the achievable discharge pressures, which are further constrained by permissible discharge temperatures, and shaft load capacity. The limits reported in literature are typically around 30 bar, with some manufacturers reporting up to 52 bar. While volumetric flow rates of up to 100,000 m^3/h have been reported, the achievable outlet pressure falls below the minimum pipeline injection pressure required in this work, and screw compressors are therefore not considered further. [43, 42, 57, 46, 47, 44]

Following the further exclusion of the remaining rotary displacement compressors, only reciprocating displacement compressors and turbo compressors remain from the initial selection. This is consistent with the literature, as according to Stolten et al., reciprocating compressors are the primary recommended technology for hydrogen applications, while centrifugal compressors are frequently cited as a viable alternative for large-scale, high-flow scenarios.[18, 20, 46]

Turbo Compressors:

In a centrifugal compressor, gas is accelerated by a rotating impeller and the imparted kinetic energy is subsequently converted into pressure in a downstream diffuser. Multiple impeller stages are arranged in series on a common drive shaft to achieve the required overall pressure ratio.

Centrifugal compressors can, in principle, handle very large volume flows of up to 50,000 Nm^3/h and discharge pressures up to 850 bar, making them technically capable of meeting the compression targets of a large scale hydrogen production plant. They represent a mature technology in hydrogen-rich gas applications. However, the low molecular weight of hydrogen fundamentally limits the achievable pressure ratio per stage to only 1.1 to 1.2. Since the maximum achievable pressure rise is approximately nine times lower for hydrogen than for natural gas at the same impeller speed, a dramatically greater number of stages is required for equivalent duty, quickly exceeding the practically realizable rotor dynamic stability constraints. The practical remedy is to significantly increase impeller tip speeds and, although the high speed of sound in hydrogen in principle permits such speeds, this conflicts with material strength limits imposed by hydrogen embrittlement. As a result, pure hydrogen centrifugal compression remains in the development phase, with only a few models on the market that achieve a pressure ratio of 3. *Kawasaki Heavy Industries* commenced the world's first demonstration of a centrifugal compressor for pure hydrogen in January 2026, with the *KM Comp-H2* rated at 35,000 m^3/h and a pressure ratio of 3, deployed at a liquefaction plant with the explicit objective of verifying performance under real operating conditions. Centrifugal compressors therefore remain a promising future candidate, but are not considered further in this work. [20, 46, 43, 58, 44]

Axial compressors are an established technology for large-scale gas pipeline compression at moderate pressure ratios, and have been proposed for hydrogen pipeline applications in the literature. However, the low molecular weight of hydrogen and the susceptibility of many metals to hydrogen embrittlement under high mechanical stresses limit the achievable pressure ratio per stage, resulting in an impractically large number of stages [59, 60]. In the available literature, axial compressors could not be identified as viable options for industrial-scale hydrogen service, and commercially available units for this application could not be confirmed. Axial compressors are therefore not considered further in this work.

Reciprocating Displacement Compressors:

In a diaphragm compressor, the movement of a piston is transmitted via a hydraulic fluid to a thin metal membrane, the diaphragm, which physically separates the hydraulic section from the compression chamber. This design completely isolates the hydrogen from lubricating oils and hydraulic fluid, making diaphragm compressors particularly suitable for high-purity gas applications. Discharge pressures of up to and exceeding 1000 bar are achievable, well above the pipeline injection pressures required in this work. However, throughput is inherently limited by small compression chambers and high flow rates causing a higher risk of premature diaphragm failure, restricting capacity to a practical maximum of around 2000 Nm^3/h per unit. Diaphragm compressors are therefore suitable for high-purity, high-pressure hydrogen service, but are restricted to smaller-scale applications and are therefore not further considered in this work.[21, 43, 46, 20, 61]

In an ionic liquid compressor, a hydraulically driven ionic liquid periodically displaces the gas volume within the compression chamber, thereby functionally replacing the solid piston of a conventional reciprocating compressor. The negligibly low solubility of hydrogen in ionic liquids eliminates the need for a separating membrane. This results in an efficiency of approximately 70% and a specific energy consumption of roughly 25% of a comparable reciprocating compressor. Discharge pressures of up to 1000 bar are achievable. However, the capacity of ionic liquid compressors is fundamentally limited by the small swept volumes inherent to the design, with a practical maximum of approximately 500 to 750 Nm^3/h per unit . The technology has been developed and commercialized for hydrogen refuelling stations, an application characterized by small flow rates, high pressures and intermittent operation. Due to the differing requirements of a large-scale hydrogen production plant and the lack of relevant literature for this application are ionic liquid compressors not considered further in this work [46, 42, 21, 20, 62, 63].

Following the exclusion of rotary displacement compressors, turbo compressors as well as diaphragm and ionic liquid compressors, the piston compressor remains as the only established mechanical technology that fully meets the requirements of this work and will now be examined in detail.

Reciprocating Piston Compressor:

A single-stage reciprocating piston compressor is built around a piston-cylinder assembly equipped with automatic intake and discharge valves. The piston is driven by a crankshaft-connecting rod mechanism, which converts the continuous rotational output of the drive motor into the oscillating linear, reciprocating motion characteristic of this compressor type. During the downward stroke from the so called "Top Dead Center (TDC)" to "Bottom Dead Center (BDC)" , the expanding cylinder volume creates a pressure drop below the suction pressure, causing the intake valve to open and gas to flow into the cylinder. At BDC, the intake valve closes and the trapped gas is sealed within the cylinder. On the return stroke toward TDC, the progressively reducing cylinder volume compresses the gas. Once the rising gas pressure exceeds the set discharge pressure, the discharge valve opens and the compressed gas is expelled (Fig. 2.5). [21, 45, 38]

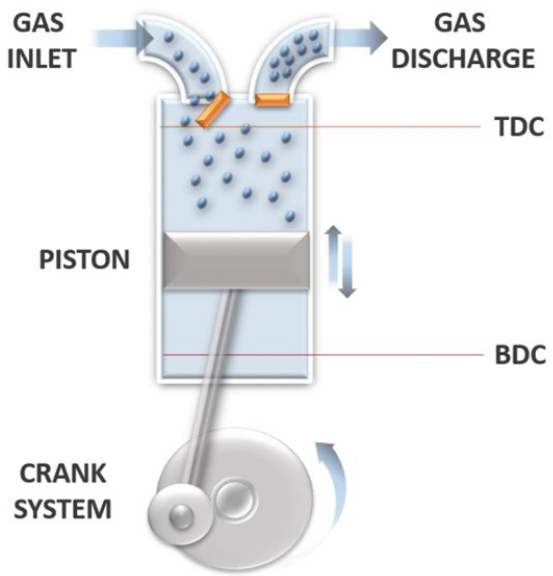

Figure 2.5: Reciprocating piston compressor [21]

For high overall pressure ratios, a multistage configuration is employed, in which successive compression stages are connected in series with intermediate heat exchangers between each stage. Intercooling removes the heat of compression between stages, reducing the inlet temperature of each subsequent stage and thereby lowering the specific compression work. This approach approximates a stepwise isothermal compression process and is standard practice for hydrogen compression applications.

The number of stages and the intermediate pressure levels are optimized to minimize total power consumption while remaining within the mechanical and thermal limits of each stage. The pressure ratio per stage is typically limited to 4.5 to 5.0 at low inlet pressures, decreasing to 2.0 to 2.5 at inlet pressures above 70 bar, due to constraints on piston rod load and volumetric efficiency [43, 20, 21].

Reciprocating piston compressors are consistently identified in the literature as the most mature and widely deployed technology for hydrogen compression [42, 46, 43, 47]. They are broadly classified into oil-lubricated and oil-free (dry-running) designs. Lubricated types achieve the highest pressures and largest throughput but require downstream gas purification to remove contamination's. Together, the two designs cover a wide range of operating conditions, with flow rates ranging from small-scale applications of around 10 Nm^3/h up to over 100,000 Nm^3/h in the largest industrial configurations. Discharge pressures also vary from a few bar up to more than 1000 bar, well above the pipeline injection pressures required in this work. [43, 42, 46, 64]

The main advantages of reciprocating compressors is their versatility. The broad achievable range of pressures and flow rates makes them adaptable to a variety hydrogen applications [44]. Partial load operation is achievable through techniques such as speed regulation, making reciprocating compressors well-suited for operation at varying loads, due to intermittent renewable energy input. As a fully mature technology with decades of industrial hydrogen service, a broad supplier base and an extensive spare parts supply chain further support high operational reliability and predictable maintenance planning. The technology's performance is also largely independent of gas density, making it inherently well-suited for light gases such as hydrogen, unlike centrifugal compressors whose performance degrades significantly with decreasing molecular weight. [43, 46, 45, 65]

The disadvantages of reciprocating compressors are rooted in their design mechanics. The output capacity is determined by the cylinder swept volume and operating frequency. Scaling up throughput requires larger, heavier pistons that generate substantially higher inertial loads, which in turn necessitates a reduction in operating speed to keep mechanical stresses within acceptable limits. High cycling frequencies are therefore only practically achievable in smaller, compact designs, which inherently constrains the maximum flow rate per unit and explains why the technology is most commonly deployed in the small-to-mid flow range. The reciprocating motion also produces pressure pulsations, vibrations and noise, requiring pulsation dampeners in both piping directions and vibration isolation measures.

These auxiliary demands, combined with the need for intercoolers and a substantial structural foundation, result in a large overall plant footprint as well as adding to system complexity and capital cost. Effective in-cylinder cooling is not achievable due to the presence of moving parts, which increases the heat of compression and adds thermal management complexity [20, 21, 44]. The large number of moving and wear-prone components such as pistons, valves, connecting rods, crankshaft and sealing rings, results in substantial maintenance requirements, with annual maintenance costs estimated at approximately 5% of total investment, frequent start-stop cycles, as expected in dynamically coupled renewable operation, further accelerate wear and reduce service intervals [46, 43, 20]. Additionally, the dynamic sealing surfaces represent potential hydrogen leak paths, which requires careful attention as prolonged exposure to high-pressure hydrogen poses a risk of hydrogen embrittlement in metallic components, necessitating appropriate material selection, sealing and periodic inspection. [21, 20, 44]

Reciprocating piston compressors fulfill all primary technical requirements of this work and represent the established industrial reference for hydrogen compression at this scale. They are therefore retained as the benchmark technology against which the metal hydride compressor is evaluated with respect to footprint, noise and vibration, maintenance effort, and suitability for dynamic renewable energy integration.

Technology Assessment:

Of the compressor types discussed, only the reciprocating piston compressor fulfills all primary requirements for large-scale hydrogen compression in this work, covering the necessary pressure and flow rate ranges while representing the established industrial standard. Liquid ring and screw compressors are limited by insufficient achievable discharge pressures, while ionic liquid compressors as well as diaphragm compressors are restricted by their capacity and development for a different application. Centrifugal compressors, while capable of large volume flows, are currently not technically mature for pure hydrogen service at the required pressure ratios. The reciprocating piston compressor is therefore retained as the sole benchmark technology against which the MHC is evaluated in this work with respect to footprint, noise and vibration, maintenance effort, and suitability for dynamic renewable energy integration.

2.3 Metal Hydrides

While mechanical compressors are the well-established standard in current hydrogen infrastructure, they face several fundamental technical challenges, such as moving parts introducing wear, complex structure resulting in substantial maintenance requirements, noise emission and vibration as well as the necessity for significant electrical energy input [19, 20, 21].

One of the most promising non-mechanical alternatives, that circumvents the disadvantages of mechanical compression, is the thermally driven metal hydride compressor (MHC). Metal hydride hydrogen compression operates in a thermal cycle based on a reversible heat-driven reaction between a hydrogen gas and a metal, alloy, or intermetallic compound, M, occurring under certain temperature and pressure conditions. This is described by the following reaction, with x as the stoichiometric quantity of hydrogen bonded to M [19, 18, 23, 66, 67, 15]:

$$\mathrm{M\,(s)} + \frac{\mathrm{x}}{2}\,\mathrm{H_2\,(g)} \underset{\text{Desorption}}{\overset{\text{Absorption}}{\rightleftharpoons}} \mathrm{MHx\,(s)} + \mathrm{Q} \tag{2.15}$$

This cycle operates through two main phases:
The first phase involves exothermic hydrogen absorption (the forward direction of Reaction (2.15)). This occurs at lower temperatures and pressures. During this stage, the metal absorbs hydrogen to form a metal hydride, MHx. As the hydride forms, it releases heat, Q, equivalent to the hydrogenation enthalpy - ΔH.[19, 18, 23, 66, 67, 15]

By raising the temperature, the system reverses the reaction and enters into the second phase, the endothermic hydrogen desorption. The metal hydride decomposes, absorbing roughly the same amount of heat released during the first phase. Crucially, this release of hydrogen occurs at significantly higher pressures.[19, 18, 23, 66, 67, 68]

The specific temperature and pressure conditions for these processes to occur depend on the selected metal hydride-forming material, with its specific thermodynamic and kinetic properties. [19, 18, 23, 66, 67, 15]

This technology offers several advantages over the conventional compression technologies suitable for a large-scale hydrogen production plant, that were outlined in Subsection 2.2.2. [18, 23, 19, 22, 20, 22, 69, 70]

- Simplicity and reliability: The absence of moving parts eliminates vibration, noise emission and mechanical wear, thereby increasing system reliability and reducing maintenance requirements.
- Utilization of low-grade waste heat instead of electrical energy
- Safety: Low-pressure hydrogen storage combined with self-limiting desorption kinetics, caused by the endothermic desorption process, cooling and therefore slowing the reaction upon containment failure and providing an inherent safety buffer and increasing overall system flexibility
- High hydrogen purity: The absorption–desorption reaction is highly selective, enabling delivery of ultra pure hydrogen (up to 99.9999 mol%)
- Compact hydrogen storage: The high volumetric density of hydrogen in the metal matrix reaches appropriately 100 g_{H2}/L, exceeding the volumetric density of liquid hydrogen (70 g_{H2}/L) at its boiling point (-252.9 °C) .
- Modularity and scalability: The technology allows for modular system design, enabling flexible adaptation to varying flow requirements.

Despite these advantages, it must be noted that metal hydride technology is considerably less mature than mechanical compression and still requires further development and remains an active subject of research and development, as evidenced, for example, by ongoing investigations at the Helmholtz-Zentrum Hereon in Geesthacht. [19, 18, 23, 66, 67, 68]

2.3.1 Metal Hydride Materials

Hydrogen possesses the ability to form stable bonds with a vast array of metals and alloys. The nature of these bonds is largely determined by the host element's position in the periodic table: s-block elements (alkali, alkaline earth metals) typically form ionic bonds, d- or f-block (transition metals, including lanthanides and actinides) elements form metallic bonds and the remaining p-block elements form covalent bonds. Due to ongoing research, a definitive classification is not always possible. Furthermore, certain elements, most notably the noble gases, do not form binary compounds with hydrogen. [71, 72, 73, 67]

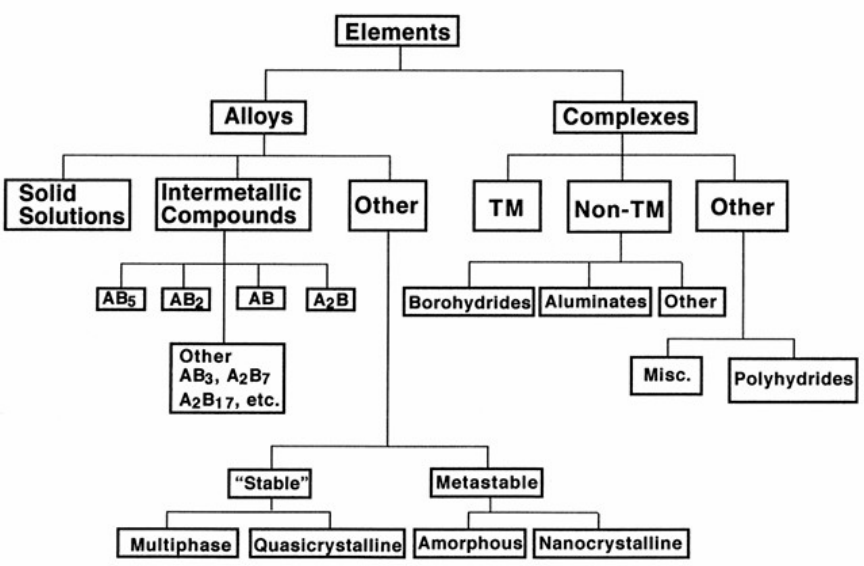

Figure 2.6: "Family tree of hydriding alloys and complexes. TM = transition metal" [71]

Based on these interactions, hydrides are generally categorized into three main groups: Ionic, also known as saline hydrides, generally known as MHx, are formed when hydrogen reacts with electropositive s-block elements, specifically alkali or alkaline earth metals. The structure relies on an electrostatic bond between a metal cation M^{n+} and a hydride anion H^{-}. Common examples include Lithium Hydride LiH and Sodium Hydride NaH. [71, 72, 73, 67]

Like ionic hydrides, metal(lic) hydrides, also known as interstitial hydrides, are often described by the formula MHx, but their structure is fundamentally different. Metal Hydrides form, when hydrogen is bound in the interstitial sites of the metal lattice. The metal bonds do not change the metallic structure significantly, aside from minor distortions. Metal hydrides can consist of a single element, an alloy, or a complex material. Alloys are further divided into the categories solid solutions, intermetallic compounds, and high-entropy alloys, as can be seen in 2.6. [71, 72, 73, 67]

Covalent hydrides, also known as molecular hydrides, are formed by hydrogen and p-block elements (groups 13–17). The bond between hydrogen and the other element consists of shared electron pairs between atoms. There are further distinctions into polymeric and volatile subgroups. Group 12 hydrides are often considered intermediate between covalent and metallic hydrides. [71, 72, 73, 67]

Due to the different nature of hydride formation, which in turn depends on the chemical nature of the host material, hydrides differ in their chemical and physical properties. This influences storage capacity, working temperatures and pressures and therefore application. [71, 72, 73, 67]

2.3.2 Intermetallic Compounds

From a technical perspective the most important hydrides for hydrogen storage and compression are the intermetallic compounds , as absorption and desorption are possible under mild temperature conditions. Depending on the stoichiometry, the compounds can further be classified into groups, as exemplary shown here [74, 75, 72, 73, 18, 75].

- AB_5
- AB_2
- BCC (body-centered cubic solid solutions)
- AB

Furthermore, the partial substitution of the A and/or B element offers any number of possibilities for producing hydride-forming materials with specific properties desired by the user [71, 73, 74].

Their functionality relies on the precise combination of two distinct metallic elements ("A" and "B") with opposing affinities for hydrogen to create a thermodynamic balance. Element A is typically a rare earth metal or early transition metal found on the left side of the periodic table. They have a strong chemical affinity for hydrogen and a large difference in electronegativity relative to hydrogen (0.5 to 1.0), leading to the formation of very stable hydrides. The B element is usually a late transition metal on the right side of the periodic table. They exhibit a lower electronegativity difference (0.2 to 0.5), compact crystal lattices, and high cohesive energies. These elements generally form unstable hydrides or do not bond with hydrogen at all, such as Iron. The B elements can enhance reaction kinetics, and through varying ratios, it is possible to engineer a metal hydride with optimal properties for specific uses [75, 72, 71].

Intermetallic compounds can operate under moderate conditions, making them ideal for system integration. On the downside, these materials often have low gravimetric capacity, rarely exceeding 2.0 wt% [72].

Exemplary, the group of AB_5 alloys is a category of intermetallics formed by combining rare-earth elements (Site A) with transition or non-transition metals (Site B), such as nickel, cobalt, aluminum or tin. One prominent representative is $LaNi_5$, where lanthanum occupies the A-site and nickel the B-site, forming the basis for numerous commercial and research-grade materials. These alloys generally exhibit a hydrogen storage capacity between 1.2 and 1.5 wt % with a wide operating range between 0 to 200 °C and < 1 to 200 bar. The substitution of elements heavily influences the metal hydride properties, e.g. aluminum increases durability during extended cycling, while simultaneously decreasing capacity. [71, 18, 23, 66]

2.3.3 Thermodynamics

The relationship between the temperature applied and the resulting equilibrium pressure is given by the Van't Hoff equation 2.16:

$$ln\left(\frac{P_{eq}}{P_0}\right) = \frac{\Delta H}{RT} - \frac{\Delta S}{R} \tag{2.16}$$

where P_eq is the equilibrium pressure, P_0 is a reference pressure (usually 1 atm), T is the temperature, ΔS and ΔH are the changes in hydrogenation entropy and enthalpy and R = 8.314 J / (mol K) the universal gas constant. [18, 67]

A resulting Van't Hoff Plot 2.7b shows the linear correlation between $ln(p/p_0$ and 1/T. The "values for ΔH and ΔS can be obtained from the slope and intercept of the linear correlation" [15]. ΔH and ΔS are two important parameters for practical application. ΔS only varies slightly around approximately 111 ± 14 $J/(mol_{H2}\ K)$ for most alloys and intermetallic compounds. This consistency arises because ΔS is governed primarily by the configurational entropy released upon hydrogen dissociation (130 $J/(mol_{H2}\ K)$). ΔH is therefore the parameter, that is predominantly determining the plateau pressure, which reflects the average metal–hydrogen bond strength, which varies significantly between metal hydrides [23].

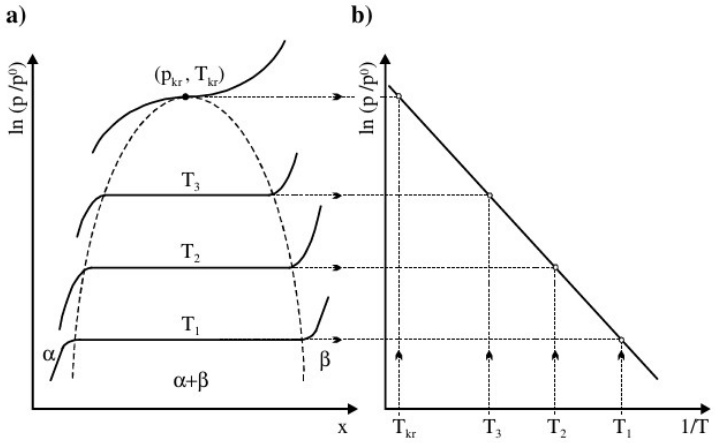

Figure 2.7: Ideal Systems: a) Pressure-Composition Isotherms (PCI), b) Van't-Hoff-Diagram [73]

To initially determine the equilibrium pressures to represent the linear Van't Hoff correlation or to obtain further information about the absorption and desorption process such as the capacity or cycle productivity, it is necessary to represent the so-called Pressure-composition isotherms (PCIs), an ideal version shown in 2.7a. These can be determined experimentally by exposing the alloy to increasing hydrogen pressure in a sealed vessel at the same temperature. [18, 15]

The characteristic shape of the PCIs is the direct result of how hydrogen interacts with the metal lattice at the atomic level. When molecular hydrogen contacts the metal, the hydrogen molecules first adhere to the surface via weak Van der Waals forces (physisorption). They then dissociate into individual atoms and form chemical bonds with the surface (chemisorption). These atoms penetrate the surface and exothermically diffuse into the metal lattice, randomly occupying interstitial sites (voids). At this early stage, the hydrogen concentration is low. The hydrogen atoms interact strongly with the surrounding metal atoms but barely interact with each other. This creates a solid solution known as the α-phase. [66, 15] This is illustrated by the following equation 2.17:

$$\mathrm{M\,(s)} + \frac{\mathrm{y}}{2}\,\mathrm{H_2\,(g)} \underset{\text{Desorption}}{\overset{\text{Absorption}}{\rightleftharpoons}} \mathrm{MHy\,(s)\,(}\alpha\mathrm{phase)} \tag{2.17}$$

In the steep left part of the curve, pressure rises sharply with concentration as it becomes increasingly harder to force more hydrogen into the random lattice sites without significant external pressure [23, 73, 68]

As more hydrogen is forced into the material, the concentration reaches a critical limit. The hydrogen atoms begin to interact with each other, leading to the nucleation of a new, ordered structure called the hydride phase or β-phase. This phase has a distinct, fixed hydrogen-to-metal ratio. In this stage, the dilute α-phase and the concentrated β-phase coexist. Any additional hydrogen gas doesn't increase the pressure, instead, it is consumed to transform more of the α-phase into the β-phase. This equilibrium creates the flat plateau (pressure equilibrium) seen in the isotherm. The length of this plateau represents the usable, also known as reversible capacity of the material, which is significantly lower than the maximum capacity[23, 67, 73, 15] This is illustrated by the following equation 2.18

$$\mathrm{MHy\,(s)\,(}\alpha\mathrm{phase)} + \frac{\mathrm{x}-\mathrm{y}}{2}\,\mathrm{H_2\,(g)} \underset{\text{Desorption}}{\overset{\text{Absorption}}{\rightleftharpoons}} \mathrm{MHx\,(s)\,(}\beta\mathrm{phase)} \tag{2.18}$$

Once the entire metal matrix has been converted into the β-hydride phase, the phase transition is complete. The material is now fully saturated. To force any further hydrogen into this fully formed hydride lattice, the hydrogen must occupy less favorable sites or expand the lattice further. This resistance causes the pressure to rise steeply again (the right side of the curve), indicating that the material can accept very little additional hydrogen even with large increases in pressure. [15, 23, 73]

During discharge, the process reverses. Nuclei of the hydrogen-poor α-phase form on the surface, eventually creating a continuous layer. Hydrogen atoms diffuse from the bulk β-phase through this α-layer to reach the surface, where they recombine into hydrogen molecules and return to the gas phase.[73]

The shape of these isotherms is heavily influenced by temperature. As the operating temperature increases, the distinct plateau region in which the two phases coexist gradually narrows. This trend continues until the system reaches its critical temperature (T_{cr}). At this point, the plateau vanishes entirely, and the distinction between the α and β-phases disappears, resulting in a smooth, continuous curve.[74]

In a theoretically ideal system (as depicted in Figure 2.7), the hydride formation process is perfectly reversible. This implies two key conditions [73]:

- Pressure Symmetry: The equilibrium pressure required to absorb hydrogen is identical to the pressure at which it is released during desorption.
- Isobaric Transition: The phase transformation from the solid solution (α-phase) to the metal hydride (β-phase) occurs not only at a constant temperature (isothermally) but also at a strictly constant pressure (isobarically).

The actual behavior of metal hydride systems under experimental conditions deviates more or less from the ideal behavior described. Those deviations that real-world systems exhibit are known as hysteresis and plateau slope and shown in 2.8 [73, 68, 71].

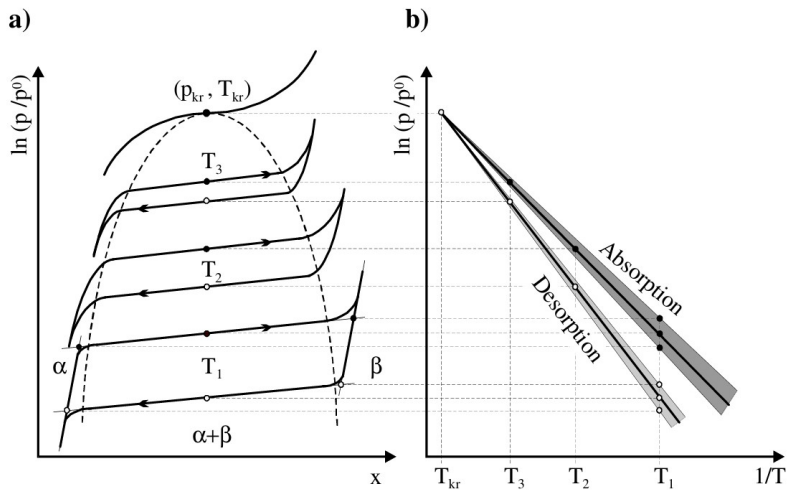

Figure 2.8: Real Systems: a) Pressure-Composition Isotherms (PCI), b) Van't-Hoff-Diagram [73]

Hysteresis refers to the discrepancy between the absorption and desorption pathways at temperature T, with the equilibrium pressure of the absorption process being lower than the equilibrium pressure of the desorption process. This is indicating that the system is not in a state of perfect thermodynamic equilibrium during operation. [71, 23]

The primary driver of this phenomenon is lattice strain energy. When hydrogen atoms force their way into the small interstitial sites of the metal lattice during absorption, the lattice must physically expand. The system must overcome an energy barrier to stretch the metal structure, requiring higher pressure. Conversely, during desorption, the hydrogen leaves an already expanded lattice, meaning that this strain barrier is absent, allowing release at a lower pressure. [23, 74, 73]

This effect typically diminishes at higher temperatures. As the material heats up, the metal lattice expands naturally (increasing interstitial hole size) and its shear modulus decreases (becoming softer), reducing the energy penalty for hydrogen insertion. Other contributing factors include irreversible plastic deformation, the creation of crystal defects, and non-stoichiometric compositions.[73]

Plateau slope is the other effect that non-ideal systems can exhibit. In ideal diagrams, the two-phase region is perfectly horizontal, while in real PCIs there is almost always a sloped plateau, where pressure increases gradually across the transition range. This slope is caused by inhomogeneities in the material, such as variations in lattice stress or chemical composition. Due to this slope, the "plateau pressure" is technically defined in engineering practice as the pressure measured at the midpoint of the plateau capacity and suction P_L and discharge pressures P_H are respectively higher and lower than the values calculated with the Van't Hoff equation. [15, 23]

Figure 2.3.3a) illustrates the operating principle of a single-stage metal hydride compressor on a pressure-composition diagram. The dashed blue curve represents hydrogen absorption at the low temperature T_L, while the solid red curve shows desorption at the high temperature T_H. The cycle begins at Point A, where the material absorbs hydrogen at low pressure P_L and temperature T_L, reaching a hydrogen concentration of C_A. Upon heating to T_H, the equilibrium pressure rises and the material desorbs hydrogen at the elevated pressure P_H (Point B), reducing the stored concentration to C_B. Engineers evaluate the performance of this thermal compressor using the compression ratio and the cycle productivity. [66, 23]

- Compression ratio (CR): The factor by which the pressure is increased, calculated as P_H/P_L.
- Cycle productivity: The actual quantity of hydrogen leaving the compressor. This is equal to the reversible capacity of the material in the operating pressure-temperature range $\Delta C = C_A(P_L, T_L) - C_B(P_H, T_H)$, whereby it must be considered that a and b are temperature-dependent.

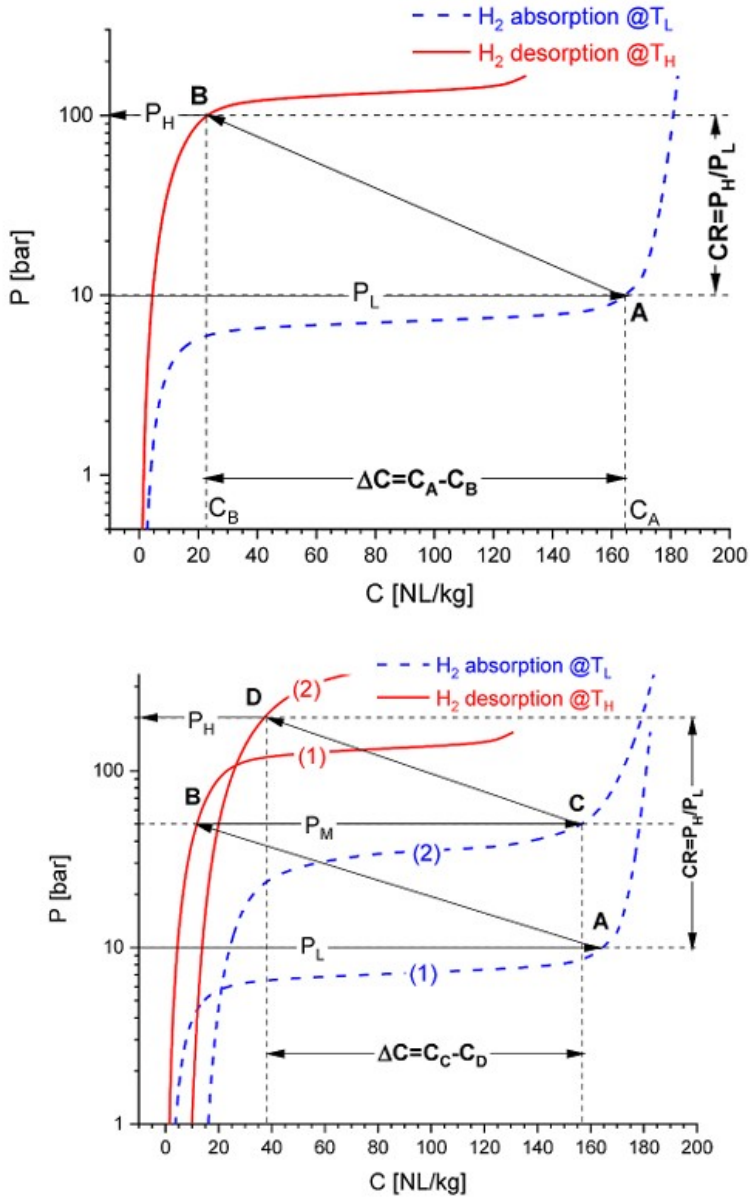

Figure 2.9: Operating principle of a single-stage (a) and two-stage (b) metal hydride compressor [18]

When working with limited available temperature differentials ((T_L to T_H) it is possible that a single stage compressor cannot achieve the desired high compression ratios and a multi-stage compression layout is needed. In this configuration, the discharge from one stage becomes the intake for the next. Crucially, each subsequent stage utilizes a metal hydride with lower thermal stability. Thermodynamically, a less stable hydride requires higher pressures to form, meaning it generates significantly higher equilibrium pressures when heated to the same temperature.[66, 18]

The interaction between two different materials (low pressure stage 1, high pressure stage 2) creates a stepwise progression across the pressure-composition isotherms, as Figure 2.3.3 (b) illustrates .[66, 18]

1. Stage 1 Absorption (Point A): The compression cycle begins with material 1 absorbing hydrogen at the lower pressure (P_L) and low temperature (T_L) [66, 18].
2. Transfer (Path AB → BC): By heating Material 1 to T_H, the desorption begins, raising the pressure to an intermediate level (P_M). Material 2, being thermodynamically less stable, absorbs the hydrogen at the intermediate pressure [66, 18].
3. Stage 2 Desorption (Path CD): The heating T_H and therefore desorption process of Material 2 concludes the cycle, as the pressure is brought to the target value (P_H). The pressurizes gas released at Point D can either be delivered to the end-user or fed into a third stage for further compression. The overall productivity of this system is defined by the least efficient stage (ΔC along path CD) [66, 18].

2.3.4 Kinetics

While thermodynamics determine whether a metal hydride can store hydrogen under given pressure and temperature conditions, practical operation is often limited by kinetic constraints, requiring higher temperatures than thermodynamically predicted. For practical applications like hydrogen compressors and initially the selection of a suitable alloy, knowledge about the kinetic behavior is therefore essential.

The kinetic behavior of a metal hydride determines the required time for absorption and desorption of hydrogen under dynamic conditions.

Figure 2.3.4 shows two exemplary kinetic curves (absorption and desorption), representing a characteristic metal hydride behavior. The reacted fraction α is plotted against time, with α defined as the ratio of the absorbed/desorbed hydrogen mass at a given time and the maximum capacity. The hydrogenation reaction starts when the operative pressure exceeds the equilibrium pressure P_{eq}, causing the hydride to absorb hydrogen, while dehydrogenation begins when the operative pressure is below P_{eq}, causing the hydride to release hydrogen. The shape of both curves reflects the underlying rate-limiting mechanism which governs how quickly the reacted fraction α evolves. [15]

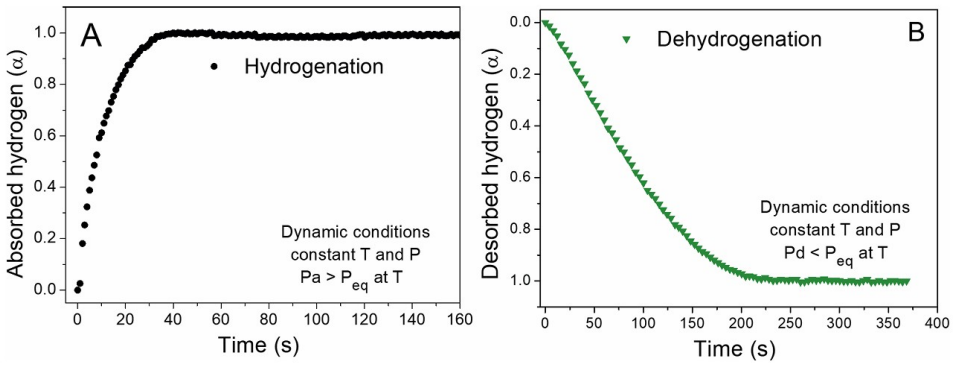

Figure 2.10: "(A) Hydrogenation kinetic behavior and (B) dehydrogenation kinetic behavior for metal-hydrogen system."[15]

Absorption and desorption reaction rates depend on temperature, pressure, and material morphology. These rates can be described by Equation 2.19 [15, 76, 77].

$$\frac{\mathrm{d}\alpha}{\mathrm{dt}} = \mathrm{K(T)} \cdot \mathrm{F(P)} \cdot \mathrm{G}(\alpha) \tag{2.19}$$

with the reaction rate $\frac{d\alpha}{dt}$, (α as hydrogen fraction, t as time) being a product of temperature function, a pressure function and a reaction model, which includes the rate-limiting step and also morphological material changes [15, 76, 77].

The temperature dependence term K(T) describes the accelerating reaction rate with an increasing temperature (with constant pressure). This is described by the Arrhenius equation 2.20:

$$\mathrm{K(T)} = \mathrm{A} \cdot \exp(\frac{-\mathrm{E}_a}{\mathrm{RT}}) \tag{2.20}$$

with A being the pre-exponential factor, EA the activation energy of the reaction, R the gas constant and T the temperature [15, 76, 77].

The pressure dependence term F(P) describes the "relationship between the operative pressure (P) and the equilibrium pressure (P_{eq})" [15]. Through experimental investigations, several functions for F(P) were developed for different alloys. Each of the functions has a rate-limiting step (such as nucleation and growth in the two-phase region) and differs for each material and experimental conditions. Examples of such functions are 2.21: [15, 76, 77]:

$$\mathrm{F(P)} = \ln(\frac{\mathrm{P}}{\mathrm{P_{eq}}}), \qquad \mathrm{F(P)} = \mathrm{P} - \mathrm{P_{eq}}, \qquad \mathrm{F(P)} = \frac{(\mathrm{P}-\mathrm{P_{eq}})}{\mathrm{P_{eq}}} \tag{2.21}$$

Both terms F(P) and K(T), provided that temperature and pressure are nearly constant for an individual curve, can be expressed as follows:

$$\mathrm{k(T,P)} = \mathrm{K(T)} \cdot \mathrm{F(P)} \tag{2.22}$$

with k(T,P) being the empirical kinetic constant. Combined with Equation 2.19, this can be written as:

$$\frac{\mathrm{d}\alpha}{\mathrm{dt}} = \mathrm{k(T,P)} \cdot \mathrm{G}(\alpha) \tag{2.23}$$

This leads to the integral form of the kinetic equation:

$$\int_0^{\alpha} \frac{1}{G(\alpha)}\, d\alpha = g(\alpha) \tag{2.24}$$

$$g(\alpha) = \int_0^{\alpha} \frac{1}{G(\alpha)}\, d\alpha = k \cdot t \tag{2.25}$$

with g(α) being the integral form of the kinetic model. A number of examples of the four main models are listed below. [15, 77, 76]

Table 2.2: Exemplary kinetic Models in integral form [15]

Model	Integral form $g(\alpha)$
Nucleation and growth models	
Johnson-Mehl-Avrami	$[-ln(1-\alpha)]^{1/n}$
Geometrical contracting models	
Contracting area	$1-(1-\alpha)^{1/n}$
Diffusion models	
1-D Diffusion	α^2
Autocatalytic models	
Modified Prout-Tompkins	$ln[\frac{\alpha}{(1-\alpha)}]$

Apart from the models shown above, there are also simplified empirical reaction order models. These approximate kinetics through chemical reaction kinetics, rather than diffusion or phase transformation mechanisms [78]. wt denotes the instantaneous gravimetric hydrogen capacity in wt. % and $w_{\max}$ the maximum achievable capacity of the metal hydride.

Table 2.3: Reaction order models [78]

Function	Form
0^{th} Order absorption	wt_{max}
0^{th} Order desorption	wt_{max}
1^{st} Order absorption	$wt_{max}-wt$
1^{st} Order desorption	wt

Building on the now established theoretical background of electrolyzers, mechanical compressors, and metal hydride systems, the Hamburg Green Hydrogen Hub (HGHH) project in Moorburg is introduced in detail in the following chapter, placing the investigated technologies within the context of a real-world application.

3 Hamburg Green Hydrogen Hub

As outlined in section 1.1, Hamburg has committed to ambitious decarbonization targets, aiming for a 70% reduction in emissions by 2030 and climate neutrality by 2045. A critical driver for achieving these goals is the supply of green hydrogen to energy-intensive industries where direct electrification is often not feasible. With local demand projected to reach approximately 7.6 TW h/a by 2030, but planned local electrolysis capacity covering only about 2.2 TW h/a (550 MW), a significant structural gap remains. This discrepancy underpins Hamburg's strategic decision to position itself not only as a production site but, crucially, as a major import and distribution hub for green hydrogen to bridge the supply deficit for both the city and the wider national market. Against this background the HGHH has been designated as a central anchor project [6]. As this thesis is based on the practical use case of the Hamburg Green Hydrogen Hub, it will be described in the following sections, focusing on its technical configuration, the transformation of the Moorburg site, and its integration into the regional energy network.

3.1 Project Description

The HGHH is a large-scale green-hydrogen production plant being developed on the site of the decommissioned coal-fired power plant Moorburg in Hamburg's port area. The center of the project is a 100 MW electrolyzer system designed to produce approximately 10,000 tons of green hydrogen per year from renewable electricity, primarily with wind and solar power from northern Germany. The start of commercial operation is scheduled for the second half of 2027. The project is explicitly mentioned and part of Hamburg's hydrogen strategy, and aims to decarbonize key segments of Hamburg's local industry, port operations, and transport sectors. [6, 79, 8]

The project is developed by a consortium consisting of *Luxcara*, a Hamburg-based energy investment and asset management company, holding a 74.9% stake, and *Hamburger Hamburger Energiewerke (HEnW)*, the municipal energy supplier, with 25.1%. Together, they form HGHH, which is responsible for the construction and operation of the electrolyzer plant and the trailer loading infrastructure. This public-private partnership reflects both the belief in commercial viability and the municipal interest in supporting a strong hydrogen infrastructure for the city's energy transition. To manage the transformation of the Moorburg site, a hundred percent subsidiary of *Hamburger Energiewerke*, *Energiehub Moorburg GmbH (EHM)* has been established as the site operator. It owns and provides the land, is responsible for the dismantling of the coal power plant, and will be responsible for the water treatment plant operation and network connection. The company will also procure electricity and market the hydrogen. [80, 81, 79, 82]

HGHH received substantial public funding under the Important Project of Common European Interest (IPCEI) *Hy2Infra* framework. It is one of 23 projects of the third wave of IPCEI, that are being sponsored to promote the emergence of European hydrogen infrastructure. The project has secured a funding commitment of around 154.1 million euros from national and regional governments, with a third of the amount coming from the city of Hamburg. Beyond the immediate 100 MW of installed capacity of the first building phase, the project explicitly anticipates expansion potential up to 800 MW on the Moorburg site. This would place Moorburg among the largest electrolysis locations in Europe [83, 80, 84, 85].

3.2 Location - Moorburg's Transition from Coal to Hydrogen

Before its closure and during its main operation between 2015 and 2020, the coal-fired power plant in Moorburg contributed to a significant increase in carbon dioxide emissions in Hamburg. According to a statement by the senate about the Moorburg plant, the coal-fired plant was the largest carbon dioxide emitter in Hamburg, until its shutdown. Its decommissioning therefore created both a substantial emission reduction and the availability of a large, well-connected energy site - that can again be made useful. [86, 87, 82]

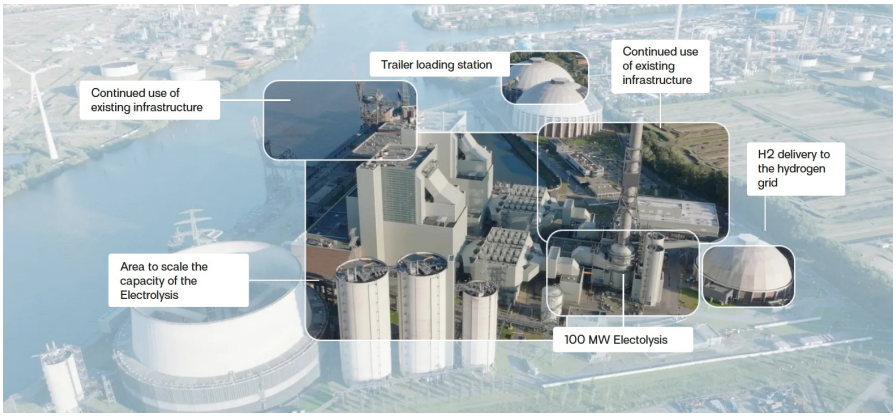

Figure 3.1: Transformation of the Moorburg site [8]

The figure 3.1 shows the Moorburg site as it was, with the coal power plant still standing. For the construction of a new production plant, there are several site-specific advantages. Those will be explained in more detail below.

Parts of the existing infrastructure and facilities can be utilized as part of the renewable energy project HGHH.

The location has an existing 380 kV connection to the national transmission grid and a 110 kV link to the city's distribution network, originally established for the high-capacity coal plant. These grid connections can now be repurposed to supply large amounts of renewable electricity to the electrolyzer, avoiding the need to build entirely new high-voltage infrastructure.[80]

Second, many auxiliary facilities of the former power station can be integrated into the new concept. Water treatment systems that previously supplied boiler feed-water can now be updated and used to provide demineralized water required for electrolysis. Parts of the switchgear and most of the underground infrastructure, such as the tunnel and cable ducts, are also to be reused. Existing buildings, such as the administration building, canteen, workshop, warehouse, a security building for site and plant, as well as the quay wall and flood defenses, will be retained, reducing both costs and resource use compared to a greenfield development.[80]

Third, Moorburg is directly linked to the port's logistics ecosystem. The site lies on the southern bank of the Elbe. River water will be used for the process water and therefore the electrolysis. The proximity to major industrial and logistics areas facilitates short pipeline connections to industrial off-takers and a possibility for the development of a stable and wide distribution network.

The hydrogen production plant will be connected to *HH-WIN*, Germany's core hydrogen network and therefore the European Hydrogen Backbone and a distribution via trailer is possible for local sales and industrial off-takers, that are not connected to the grid. The site also offers sufficient space to house additional process machinery (possible expansion to 800 MW), enabling the development of a larger hydrogen campus [80].

3.2.1 Technical Details

The publicly available and non-confidential technical data for the main components of the HGHH are summarized below to provide a better understanding of the overall system.

- **High-voltage grid connection (380 kV):** Provides the electrical power supply for the electrolysis system and auxiliary infrastructure.
- **Water Treatment Plant**: Process water is drawn from the River Elbe and treated on-site to meet the purity requirements of the PEM electrolysis process.
- **Electrolysis System:** The hydrogen production is based on six modular PEM electrolysis units (Siemens Energy Elyzer P-300), together forming a 105 MW system. As described in Section 2.1, PEM technology enables dynamic operation with start-up times under one minute, making it well-suited to variable renewable energy input. The system achieves a plant efficiency of 75.5%, producing hydrogen at a purity of 99.95 vol% at an output pressure of 100 mbar, with a mass flow of 1998 kg/h after drying [88, 89]. The electrolyzer generates waste heat at two characteristic lifecycle stages — beginning of life (BOL) and end of life (EOL) — as stack efficiency degrades over the operational lifetime. Siemens rates the stack for an optimized lifetime of 80,000 Equivalent operating hours (EOH), with continued operation beyond this threshold remaining possible [88]. Auxiliary systems, including the hydrogen compressor, contribute an additional thermal load. These figures, together with the available temperature levels, form the thermal boundary conditions for the metal hydride compressor design discussed in Chapter 4.1 and Subsection 5.2.3. [1]

[1] The exact waste heat figures are subject to confidentiality agreements and cannot be disclosed. The values used in this work were derived from electrolyzer efficiency data and degradation rates.

- **Buffer storage:** The Buffer storage acts as a decoupling interface between hydrogen production and downstream processing. While the electrolyzer is designed to operate dynamically to match the availability of the renewable energy, the mechanical compressor typically requires more stable and continuous flow conditions to operate efficiently and avoid mechanical stress. The buffer temporarily holds hydrogen to smooth short-term production fluctuations. It has a maximum volume of 140 m3 and operates isobarically at variable fill level.
- **Gas Processing (purification & compression):** Upon exiting the electrolyzer the produced hydrogen is saturated with water vapor and contains trace amounts of oxygen, that must be removed to meet the purity standard 5.0 (99.999 mol%). The gas passes through a DeOxo unit (packed-bed palladium catalyst) to remove the oxygen and an adsorption dryer to remove moisture [89, 88]. The dry hydrogen is then compressed by a four-stage reciprocating piston compressor from 100 mbarg to 30 barg. The compressor unit (approximately 180 tons [90]) requires gas coolers and vibration dampers as peripherals. While the exact dimensions of the compressor are confidential, a rough estimate based on Siemens Energy's plant layouts suggests an estimated footprint of roughly 16 × 14 m for the compressor itself, excluding peripheral equipment [89]. An additional compressor stage is installed upstream of trailer loading and pipeline feed-in.
- **Cooling:** Thermal management is provided by hybrid dry coolers. Heat is rejected via heat exchangers, recooling the heat transfer fluid from 47 °C to 35 °C, with 35°C representing the lowest temperature level available in the plant. These temperatures represent the key thermal boundary conditions for the metal hydride compressor design (see Chapter 4.1 and Subsection 5.2.3.

3.3 Timeline

Beginning with the shut-down and dismantling of the coal-fired power plant to the building of the hydrogen production plant, the HGHH is following a strict timeline, to start operation in 2027.

The transformation of the Moorburg site began with the shut-down of commercial operations at the Vattenfall coal-fired power plant in July 2021, following the operator's successful bid in the German federal coal phase-out auction. In January 2021, a letter of intent was signed to redevelop the site into a "Green Energy Hub."

The initial consortium featured four partners: the site owner *Vattenfall*, the oil & gas company *Royal Dutch Shell*, the Japanese industrial firm *Mitsubishi Heavy Industries (MHI)*, and the municipal energy supplier *Wärme Hamburg* (now H*Hamburger Energiewerke*). This group jointly applied for European Union-funding and launched the initial feasibility studies for a 100 MW electrolyzer. [87, 91, 92, 8]

However, the project structure underwent a significant realignment in 2023. The former operator of the coal-fired power plant, *Vattenfall*, sold the associated company with 94 employees, the buildings, the remaining components and the land at Moorburger Schanze to the municipal energy supplier HEnW. Following this acquisition, the private sector partners shifted and Shell and Mitsubishi exited the consortium as well. In September 2023, *Luxcara*, a Hamburg-based energy investment and asset management company, entered as the new majority partner, acquiring the shares previously held by the exiting corporations [93, 87].

With the new partnership in place, the project advanced to physical implementation. The project realization relies on a multi-contractor strategy where specialized firms handle distinct work packages, such as site dismantling, Frond End Engineering, supplying and maintenance of the core technology, and construction of the overall infrastructure.

Dismantling and site preparation works began after the shut-down of the coal-fired power plant and were transferred to the new site operator, EHM. While EHM manages the dismantling, *Arcadis*, a planning and consulting firm, helped conceptually and procedurally prepare the dismantling, with execution being handled by the *Hagedorn* Group. In November 2024 the Chimneys of the flue gas depressurization system were detonated, while the dismantling of the coal storage facilities took until the end of 2025.The area where further electrolyzer could be built in the future (scaling up to 800 MW) still needs to be completely cleared to date. [94, 95]. Some of these companies and their tasks are listed below. The engineering and consulting company *Ramboll* was commissioned to handle the Frond End Engineering & Design (FEED), including the support in the permitting process and in preparing tender documents. The major supplier contracts followed in 2024 and 2025, such as *Siemens energy* as the core technology supplier of the electrolyzer and maintenance thereof and the company *Kraftanlagen* as the main infrastructure contractor. They are responsible for the "Balance of Plant" area, which means the construction of plant infrastructure with the "planning, delivery, and construction of all ancillary technical and supply facilities for the project. These include power distribution and water treatment facilities, cooling and compressor stations, and connections to the hydrogen network and trailer loading station." [84, 96,

81] *Drees & Sommer* act as project and engineering managers to oversee construction. Their job includes site supervision, scheduling, interface management between the different contractors, and ensuring compliance with construction plans and safety standards [90].

Mid to end 2025, soil improvement measures, such as the installation of 906 vibro-compaction columns, foundation work, and a fire-protection wall were completed for the the hall, in which the electrolyzer and compressor will be, were completed. The official laying of the foundation stone took place in December 2025, symbolizing the shift from coal-based power generation to hydrogen production at the same site.

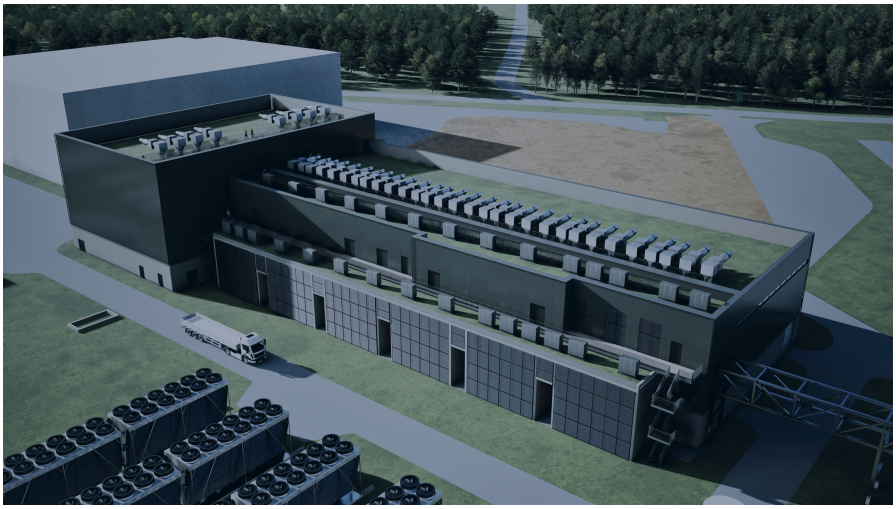

Figure 3.2: Rendering of the compressor- and electrolyzer hall [97]

The project schedule envisages completion of the electrolyzer building in the second quarter of 2026, the installation of process technology starting in the same period, and the start of commercial operation in the second half of 2027 [96, 79].

3.4 Hamburg as a Hydrogen Hub and Import Gateway

The Senate's strategy paper "Green Hydrogen Hub Europe – Hamburg as a hub for hydrogen imports to Germany and Europe" frames Hamburg's role explicitly as a hydrogen gateway for both national and European markets. This role builds on several structural advantages: Hamburg operates Germany's largest and Europe's third-largest container port, with vast existing infrastructure for bulk cargo, liquids and gases.

The port already combines deep-sea shipping, barge transport on inland waterways, extensive rail connections (around 300 km of industrial tracks) Europe's largest railway port) and direct access to the German motorway network (A1, A7, A23, A24, A20 and in the future to the A26 motorway). Hamburg's proximity to the Nord-Ostsee Canal (world's busiest artificial waterway) simplifies maritime links to Scandinavia and therefore the hydrogen transport to and from Scandinavia. At the same time, the port is closely connected to other North Sea energy locations such as Brunsbüttel and Stade, enabling coordinated development of import capacities along the Lower Elbe [6].

From a logistical perspective, these multimodal connectivity possibilities are critical. It enables efficient distribution of (imported) hydrogen and hydrogen derivatives by ship, rail, pipeline and road across Germany and into neighboring countries [6].

On the demand side, the metropolitan region around Hamburg is the third-largest industrial cluster in Germany, one of Europe's most important industrial areas. Within the port area alone, around 22 large industrial plants are concentrated in a relatively small area - doing metal production, mineral processing, energy, shipbuilding and construction. As described in 1.1, these industry plants have significant decarbonization needs. Together with mobility applications, these industries represent a stable and spatially concentrated demand base for hydrogen that can justify large infrastructure investments [6].

3.5 Network Integration with HH-WIN

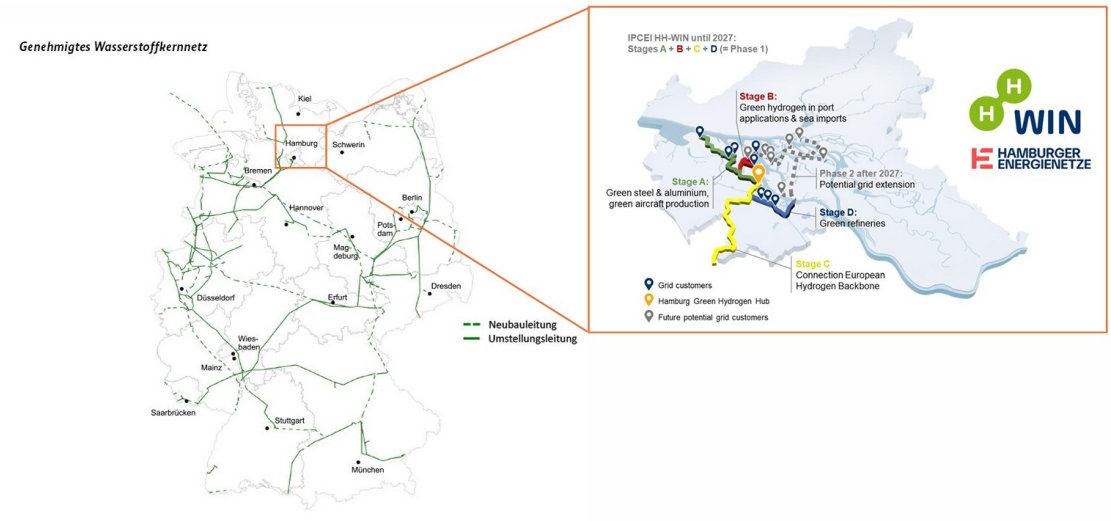

Figure 3.3: Hydrogen supply: HH-WIN and European Hydrogen Backbone Pipelines [98, 99]

The distribution and thus the success of the HGHH will be aided by another IPCEI project, the *"Hamburger Wasserstoff-Industrie-Netz" (HH-WIN)*, developed by Gasnetz Hamburg (now Hamburger Energienetze). For customers without access to the network infrastructure, delivery of the hydrogen will be accomplished via a trailer loading station at the HGHH.

In the south of Hamburg, the network will cover 60 km up to around 2030, of which the initial 40 km are sponsored by IPCEI, supplying industrial and commercial sites with produced hydrogen and imports. The expansion will largely rely on converting existing natural-gas pipelines to hydrogen service, progressively extending the network. The first companies are expected to be connected to this new hydrogen network in 2027. Expansion clusters, each of which groups potential hydrogen customers, have already been named and are intended to give other Hamburg-based companies the opportunity to be supplied with green hydrogen in the quantities needed. Possible customers are *Hamburger Hafen und Logistik AG (HHLA)* with the project "Hydrogen Logistics Applications & Distribution" (H_2LOAD) to equip various types of heavy-duty machinery with fuel cell drives or *tesa Werk Hamburg* to use green hydrogen in energy-intensive production processes. [3, 100, 101].

Hamburger Wasserstoff-Industrie-Netz (HH-WIN) will not remain a purely local network. It is intended to be connected to the planned national hydrogen core network and, via this, to the emerging European Hydrogen Backbone. Once completed, the planned national hydrogen core network will have a pipeline length of approximately 9,000 km, with around 40% of this being newly constructed. One of the most important projects in this context is the *HyPerLink* initiative of the energy network operator *Gasunie*. *HyPerLink 1* connects the Netherlands (*hydrogen network Hynetwork)* to Bremen and Hamburg, *HyPerLink 2* links Bremen and Hannover and Salzgitter and *HyPerLink 3* would establish a north–south axis between the Danish border, Schleswig-Holstein and Hamburg, connecting Denmarks hydrogen export potential to the industrial cluster around Heide and Brunsbüttel to Hamburg. Further extensions to the pipeline are planned via *Hyperlink 4* and *5*. *HyPerLink I* and *II* have already been selected for IPCEI funding. The aim is for Hamburg to become the central hub for the German hydrogen economy in the north, with Moorburg as one of the main hydrogen suppliers. [3, 16, 102].

HH-WIN designed to carry both locally produced hydrogen (for example from Moorburg) and imported hydrogen arriving via the port or via long-distance pipelines. The planned capacity of the hydrogen pipeline is around 3 TW h potentially transported energy per year in phase one and 6.4 TW h per year in phase two (with 13 possible clients in the first phase and another seven in the second phase). In phase one, 580,000 tons carbon dioxide can be saved per year, and after the completion of phase two, this figure is expected to reach 1.4 million tons. The pipeline has diameters ranging between 0.2 to 0.5 km, enabling the movement of about a million m^3 of hydrogen per hour, at pressures up to 70 bar. [16, 103, 104]

3.5.1 Compression Challenges in Moorburg

With the construction of a 100 MW electrolyzer and the possibility to scale 800 MW, the HGHH project faces the critical task of conditioning the produced hydrogen for distribution. As the hydrogen leaves the electrolysis stack at a significant lower pressure than is needed to inject it into the pipeline, it must be compressed. To manage these pressure differentials at an industrial scale, the project currently relies on multi-stage reciprocating piston compressors. As illustrated in 2.2.2 this technology is mature and a well-known, established industry standard for hydrogen applications. However, the specific boundary conditions in Moorburg as large-scale plant amplify engineering and operational challenges, motivating the investigation of a MHC as an alternative.

First, the physical dimensions and civil engineering requirements for these compressors at the existing hydrogen flows and the required compression ratio of 30 (compressor after the atmospheric electrolyzer) are substantial. Reciprocating compressors generate significant dynamic loads and vibrations due to the oscillating masses of the pistons. To prevent these vibrations from damaging the plant infrastructure, or affecting the precision of nearby sensitive equipment (like the electrolyzer stacks), massive, complex foundations are required. This necessitates extensive subsoil preparation and reinforced concrete works. Furthermore, the noise emissions generated by the mechanical movement require additional acoustic enclosures to comply with occupational safety standards.

Second, the operational profile of a green hydrogen plant clashes with the steady-state preference of such compressors. The electrolyzer at Moorburg must follow the fluctuating availability of renewable energy, like wind and solar energy. Mechanical compressors, however, struggle with frequent start-stop cycles and rapid partial-load ramps. Operating them under highly variable conditions further accelerates wear on seals, valves, and bearings, leading to high maintenance intervals and potential downtime.

Beyond the compressor itself, the multi-stage concept requires a comparatively extensive and large set of peripheral systems. In the Moorburg, this includes an isobaric buffer storage (about 140 m^3) to decouple short-term fluctuations in the flow, and thus prevent or at least improve the aforementioned damage to the compressor. There are also pulsation dampers installed at the compressor inlet and outlet. They smooth the discontinuous gas flow inherent to reciprocating pistons, thereby preventing harmful pressure waves from propagating upstream into the electrolyzer or downstream into the distribution network . Additionally, gas coolers are installed between the compression stages to remove the heat of compression, protect seals and valves, and keep discharge temperatures within reasonable limits.

These limitations, especially size, maintenance susceptibility, vibration and noise as well as the the necessity for electrical energy highlight the need for alternative compression concepts that could align better with the dynamics of renewable hydrogen production. This provides the context for the following chapters, which investigates the alternative of MHC. By utilizing thermal energy instead of mechanical work, the metal hydride technology offers a vibration-free, low-maintenance, reliable, safe and potentially more compact alternative that also leverages the site's waste heat to drive the compression process.

Despite these advantages (detailed in 2.3), metal hydride compression also presents a number of challenges that must be addressed for large-scale deployment. The main reason behind those challenges is is that, the technology still has a comparatively low commercial maturity, especially at industrial scale. While metal hydride compression has reached a technology readiness level of 9 (proven in operation environments) in stationary applications, metal hydrides are an active subject of research and development without the long standing experience that the operation of piston compressors bring with themselves. [19, 18, 23, 66, 68]

After parida et el, "the literature lacks comprehensive methodologies for designing high-pressure reactors and selecting appropriate alloys, which are crucial for the efficient operation of [MHC] systems." [105]

One of the largest factors influencing the performance of metal hydride compressors are the properties of the selected alloy. Therefore, it is fundamental prerequisite to identify a suitable alloy with certain properties, fitting the intended application. As discussed in Section 2.3.3, a metal hydride operates only within a material specific temperature–pressure window. The alloy must therefore be selected such that the operating conditions in Moorburg, with the narrow available temperature range are sufficient to achieve the required pressures. Beyond thermodynamic compatibility, the material must also exhibit a high reversible capacity, a flat plateau with minimal slope, and low hysteresis between absorption and desorption, fast kinetics, while several more factors such cycle stability or sensitivity to gaseous impurities must be taken into account. As the selection of materials for the compressor to be developed is part of this work, more detailed selection criteria are detailed in 4.3.1.[19, 18, 23, 66, 68]

Then there are design challenges, with heat transfer within the hydride bed often outlined as one of the most pressing issues. As metal hydrides typically only exhibit a low thermal conductivity, the rate at which heat can be supplied or removed during absorption and desorption is limited, the achievable cycle times and throughput is directly constrained. The thermal mass of the pressure vessel itself adds a parasitic heat capacity that further reduces the effective energy available for driving the compression cycle.[19, 18, 23, 66, 68]

With metal hydrides and metal hydride compression as a current research optic, these challenges are being tackled daily by researchers around the world, with the Helmholtz-Zentrum hereon as a well-known local example.

The following chapters introduce the modeling approach utilized in this work and its implementation, providing the basis to evaluate whether a metal hydride compressor represents a viable alternative to mechanical compression at Moorburg — and ultimately, whether its advantages outweigh the challenges outlined above.

4 Solution Approach and Model Development

Building on the theoretical foundations established in Chapter 2 and the site-specific context introduced in Chapter 3, this chapter presents the practical solution approach pursued in this thesis to develop a metal hydride compressor for hydrogen pipeline injection, as a possible alternative to mechanical compression.

The approach proceeds along four interconnected steps. First, the technical boundary conditions derived from the Moorburg site, specifically the available heating and cooling temperatures, the required inlet and outlet pressures, and the hydrogen volume flow, that are defined and consolidated in Chapter 4.1. These constraints directly govern both the selection of suitable metal hydride materials and the subsequent model development.

Second, the identification and selection of alloys that are (thermodynamically) compatible with the narrow available temperature window and the required pressure ratio represents a central challenge of this work. For this broad literature search as structured selection methodology is applied (4.3.1), drawing on criteria such as PCI-characteristics, slope, cycle stability and data availability. Subsequently, the isotherm data of the selected alloys is prepared, resulting in polynomial surface fits for integration into the simulation framework (4.4).

Third, the existing one-dimensional dynamic simulation model in Aspen Custom Modeler (ACM), described in Section 4.2, is extended and further developed to incorporate the selected alloys in one- and two-stage configurations and to quantify the compressor's performance in terms of specific productivity and specific energy demand.

The extended model then forms the basis for the systematic simulation experiments presented in Chapter 5, in which key design parameters, including operating temperatures, alloy mass ratio, cycle time, and tank geometry, are optimized. The resulting optimized configuration is subsequently scaled to the full 100 MW electrolyzer output at Moorburg to derive the compressor dimensions and thermal energy requirements for an industrial-scale application. Chapter 6 then assesses the technical feasibility of integrating the scaled system into the Moorburg site under realistic boundary conditions.

4.1 Boundary Conditions and System Outline

Although the theoretical foundation of this thesis references the Moorburger HGHH project as a practical use-case, specific technical constraints regarding metal hydride compression require an adjusted definition of the system boundaries for the design phase.

The initial theoretical framework considered the compression of hydrogen at atmospheric pressure (approx. 1 bar) after the 100 MW electrolyzer. However, a critical evaluation of the required conditioning to achieve the desired hydrogen purity of grade 5.0 reveals significant integration challenges at this pressure level. Before hydrogen can be introduced into a Metal hydride compressor (MHC), it must meet strict purity and moisture standards to prevent degradation and poisoning of the hydride-forming alloys. This necessitates passing the gas through a de-oxidation (DeOxo) unit and a dryer.

At atmospheric pressure, the volumetric flow rate of hydrogen is high due to its low density. Consequently, the sizing of the DeOxo and dryer units would become disproportionately large to accommodate the flow velocity and residence time required for effective purification. Exemplary, a hydrogen drying plant (absorption dryer) from the company *Bilfinger* for volume flows between 100,000 Nm^3/h and 1,200,000 Nm^3/h and operating pressures between 15 and 80 bar occupies a floor space of 55 x 25 m, with a height of 15 m. Although the volume flows and operating pressures in this example exceed those of Moorburg, it nonetheless illustrates the considerable scale these systems can reach.[106].

To keep the development task focused on a technically meaningful and realistic scenario, the MHC development for the thesis is shifted to a higher-pressure level and formulates two feasible alternative scenarios.

Scenario A shifts the MHC downstream, before the pipeline injection. In Moorburg at this stage, there is another mechanical compressor (operated by *Hamburger Energienetze*) to compress the hydrogen a second time from 30 to 80 bar. In Scenario A the hydrogen is produced at atmospheric pressure and first routed through a multi-stage mechanical compressor that raises the pressure to about 30 bar. Downstream of this pre-compression stage, the hydrogen is purified and dried at the elevated pressure level and is then fed to the MHC.

Alternatively, in scenario B the system is defined around a different electrolyzer concept in the expansion of the HGHH that delivers hydrogen directly at approximately 30 bar. In this configuration, purification and drying are again placed at the elevated pressure level, and the MHC is designed to reach the higher-pressure requirements for the pipeline injection.

Both scenarios preserve the project intent while providing a consistent and technically feasible boundary condition for the theoretical MHC design, namely a defined hydrogen feed pressure of approximately 30 bar after purification and drying.

4.1.1 Technical Boundary Conditions in Moorburg

Table 4.1: Technical boundary conditions at HGHH

Project Parameter	**Value**	**Unit**
Available Cooling Temperature	35	°C
Available Heating Temperature	46	°C
Inlet Pressure MHC	30	bar
Goal Outlet Pressure MHC	80	bar

To begin the design of the MHC, specifically the selection of a suitable alloy, the technical boundary conditions at the HGHH plant must be established. As detailed in Chapter 4.1, the hydrogen inlet pressure into the MHC is fixed at 30 bar, originating either from a pre-compression stage or directly from a pressurized electrolyzer. The required discharge pressure for injection into the pipeline network is 80 bar. Consequently, this pressure range represents a hard boundary for design and operation.

The compressor must reliably operate between 30 and 80 bar. As illustrated in the Subsection 2.3.2, while these individual pressure values fall within the typical operating range of many commercial hydride-forming alloys, the required pressure ratio of 2.67, corresponding to a differential of 50 bar, presents a thermodynamic challenge considering the available temperatures. This substantial compression step is an early indication that a single-stage design may not be sufficient, especially given the low available thermal driving force.

In the the exceptionally narrow temperature range available at the Moorburg site for thermal cycling lies the primary challenge of the compressor design. This constraint is critical because the cooling temperature of 35 °C is relatively high for absorption, while the heating temperature of 46 °C is very low for desorption. The resulting temperature difference ($\Delta T = 11$ K) is extremely small for achieving a pressure ratio of 2.67 and reaching 80 bar , as the relationship between pressure and temperature (Van 't Hoff equation) typically requires a larger thermal differential to drive such a compression step.

Therefore, it is necessary to evaluate whether these temperatures represent absolute hard limits analogous to the pressure requirements. The upper temperature limit of 46 °C is defined by the waste heat stream of the specific Siemens electrolyzer model currently planned. For this specific unit, the waste heat temperature is fixed and cannot be increased. However, engineering solutions such as the integration of a heat pump are conceivable to boost this temperature. Furthermore, in Scenario B (utilizing an MHC downstream of a pressurized electrolyzer), it would be possible to select an alternative electrolyzer technology that operates at a higher operating temperature, thereby providing higher waste heat temperatures. Regarding the lower temperature limit, 35 °C is determined by the capacity of the existing external cooling system. If an MHC were implemented, this cooling infrastructure could theoretically be expanded or upgraded to achieve lower absorption temperatures.

Since the strictly available temperatures make achieving the required compression ratio thermodynamically difficult or impossible with commercially available alloys, the temperature range is treated as a design guideline rather than an absolute technical limit. While deviations are permissible to make the system viable, the design objective remains to stay as close as possible to the existing site conditions. This approach avoids the need for massive oversizing of the cooling system or the selection of an electrolyzer operating at significantly higher temperatures solely for the compressor's benefit. Minimizing additional energy consumption and physical footprint must remain a priority in the design development.

4.2 Existing Model Framework

Aspen Custom Modeler (ACM), a software product developed by the company *AspenTech*, enables the development of customized process and equipment simulation models by specifying the underlying engineering equations. ACM supports steady-state and dynamic simulations solved in an equation-based manner, using an object-oriented modeling language. The language includes basic concepts such as statements for variable declarations, type definitions for models, streams, variables, etc. like temperature, parameters for fixed values, and component lists for components and physical property options. Models of process units can be combined in a flow sheet to build a simulation application. ACM can integrate physical properties from Aspen Properties with over 37,000 components, provides visualization capabilities such as custom tables, trend plots and execute a sequence of actions during a dynamic simulation in flow sheet tasks. [107, 108].

This framework supports specialized applications in chemical engineering, including the metal hydride compressor model used in this thesis, which incorporates differential equations, thermodynamic and kinetic data and models, heat and mass transfer balances as well as and dynamic pressure/heat cycling controls for the selected alloys.

4.2.1 Description of the Existing Model

The dynamic ACM model used for designing the metal hydride compressor is based on a model developed by Lukas Fleming, a Research Associate/PhD student at Helmut Schmidt University and supervisor of the present work. The model was validated by him, using experimental data obtained from a laboratory compressor at the Helmholtz Zentrum hereon.

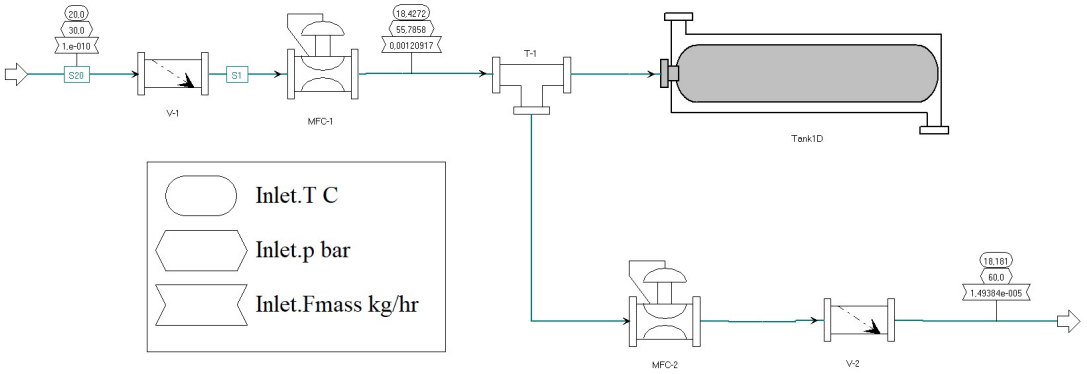

Figure 4.1: Flowsheet Aspen Custom Modeler

In the model, the process fluid hydrogen flows from the left through valve V1 and mass flow controller MFC-1 into the compressor tank Tank1D. The tank is externally cooled for absorption, with a defined time period set to ramp the temperature. Following the cooling phase, the temperature is ramped up for desorption, allowing hydrogen to exit at elevated pressure via the T-piece T-1, through mass flow controller MFC-2 and valve V2. The governing calculations of the model will be described in more detail in the following.

The central model in the flowsheet is the compressor tank model Tank1D, which simulates the dynamic behavior of the metal hydride bed during absorption and desorption cycles, including the associated thermal and chemical processes.

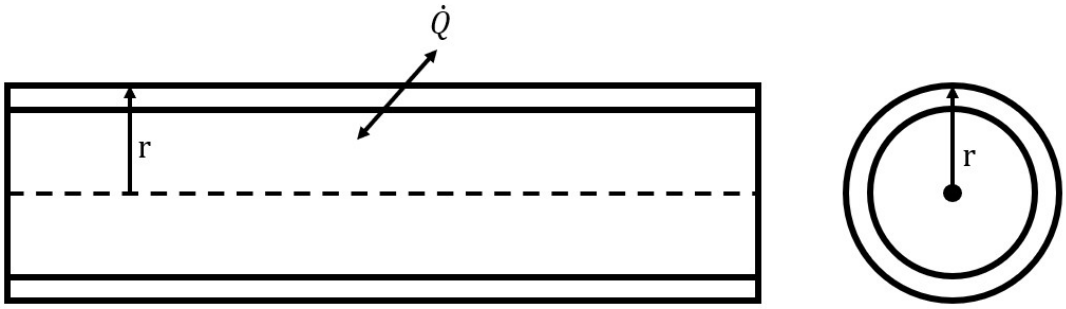

Figure 4.2: Schematic Compressor 1D Model

Figure 4.2 illustrates the geometry and modeling assumptions of the tank as a one-dimensional radial model. The Metal hydrides (MH) bed forms the inner cylinder with diameter d_{bed}, surrounded by a steel tank wall of thickness t_{wall}.

The most important tank variables are summarized in Table 4.2. Variables in the ACM model are classified into three types: *fixed*, *free*, and *initial* variables. Fixed variables are constant inputs specified before the simulation such as the the alloy mass M_{alloy} and bed diameter. Free variables are computed by the equation system during simulation, such as geometric variables that can be derived from set fixed variables such as l_{bed} and t_{wall}. Initial variables carry a prescribed value only at $t = 0$ as a starting condition for the integrator. These are for instance, the temperature of the heat transfer fluid (T_{HTF}) at the start of each simulation run. It should be noted here that, as long as an equilibrium between free, fixed, and initial variables exists, for example, a free variables can be assigned an fixed value, that solely depends on the objective of the simulation.

Table 4.2: Tank geometry parameters and derived quantities

Parameter	Symbol	Unit	Calculation/Description
Bed diameter	d_{bed}	m	fixed input
Bed length	l_{bed}	m	$l_{tank} - 2\,t_{wall}$
Tank length	l_{tank}	m	$M_{alloy} = l_{bed} \cdot \frac{\pi}{4}\, d_{bed}^2 \cdot \rho_{\text{bulk,unsat}}$ [a] $l_{bed} = l_{tank} - 2\,t_{wall}$
Tank diameter	d_{tank}	m	fixed input
HE inner diameter	$d_{HE,in}$	m	fixed input
Wall thickness	t_{wall}	mm	$(d_{tank} - d_{bed})/2$
Hydraulic diameter	d_h	mm	$d_{HE,in} - d_{tank}$
Bed volume	V_{bed}	m^3	$l_{bed} \cdot \frac{\pi}{4} \cdot d_{bed}^2$
HTF volume	V_{HTF}	m^3	$\frac{\pi}{4}(d_{HE,in}^2 - d_{tank}^2) + 0.00033$[a]
Tank volume	V_{tank}	m^3	$l_{tank} \cdot \frac{\pi}{4}(d_{tank}^2 - d_{bed}^2)$ $+ 2 \cdot \frac{\pi}{4} \cdot d_{bed}^2 \cdot t_{wall}$
Tank surface area	A_{tank}	m^2	$\pi \cdot d_{tank} \cdot l_{tank}$
Alloy mass	M_{alloy}	kg	fixed input
Tank mass	M_{tank}	kg	$V_{tank} \cdot \rho_{\text{steel}}$
HTF mass	M_{HTF}	kg	$V_{HTF} \cdot 1050$

[a] l_{tank} calculated implicitly by the equation-oriented solver as M_alloy is fixed

The Heat Transfer Fluid (HTF) flows through the outer ring-shaped gap between the tank outer wall and the heat exchanger inner diameter $d_{HE,in}$. Heat exchange $\dot{Q}$ between the fluid and the tank wall drives the thermal management of the absorption and desorption cycles. Hydrogen is transferred into the tank via a mass port, which connects the metal hydride tank to adjacent process units in the flowsheet by exchanging variables such as mass flow and pressure across the model boundary.

As a one-dimensional model, it discretizes the radial spatial coordinate r into finite segments using CFD2 (second-order centered finite differences) as the discretization method. The bed domain (bedradial) employs $n_{bed} = 10$ uniform intervals yielding 11 nodes, while the wall domain (wallradial) uses $n_{wall} = 4$ intervals yielding 5 nodes, with its origin located at the outer bed radius. This spatial discretization transforms the continuous partial differential equations (PDEs) into a system of coupled ordinary differential equations (ODEs), one per spatial node, which are then integrated over time by the ACM solver.

State variables such as temperatures T_{bed} and T_{wall}, equilibrium pressures p_{eq}, and reaction rate R vary only with radial position r (from the centerline $r = 0$ to the outer tank wall) and time t, under the assumption of circumferential and axial uniformity. Symmetry boundary conditions enforces the absence of radial gradients at the central axis, which satisfies this aforementioned assumption. Another physical boundary is the temperature and heat flux continuity between the two spatial domains of bed and wall.

The tank model incorporates comprehensive material data for the the gas phase, the selected metal hydrides and the tank. This includes data such as the thermal conductivity and specific heat capacity of the steel, the molar mass of hydrogen as well as densities and thermodynamic and kinetic parameters of the alloy, as summarized in Table 4.3.

Table 4.3: Alloy parameters

Parameter	**Symbol**	**Unit**
Particle size, unsaturated	d_{p0}	m
Storage capacity	wt_cap	wt%
Equilibrium coeffs (Abs.)	KoeffAbs[1:18]	–
Equilibrium coeffs (Des.)	KoeffDes[1:18]	–
Reaction enthalpy (Abs.)	ΔH_abs	GJ/kmol
Reaction enthalpy (Des.)	ΔH_des	GJ/kmol
Pre-exponential factor (Abs.)	A_abs	1/s
Pre-exponential factor (Des.)	A_des	1/s
Activation energy (Abs.)	Ea_abs	kJ/mol or J
Activation energy (Des.)	Ea_des	kJ/mol or J
Bulk density, unsaturated	ρ_bulk_unsat	kg/m^3
Crystalline density, unsat.	ρ_cryst_unsat	kg/m^3
Crystalline density sat.	ρ_cryst_sat	kg/m^3
Eff. thermal conductivity (bed)	$k_e f f_f ix$	W/(mK)
Alloy specific heat capacity	cp_alloy	kJ/kg·K

The model contains several governing equations covering the key physical phenomena of a metal hydride system. These include the hydrogen saturation balance and the associated alloy swelling, the energy balances for the bed, wall, and heat transfer fluid, the resulting heat of reaction, as well as the hydrogen mass balance.

The energy balance for each radial node of the MH bed is given by:

$$\rho_{\text{bulk,1D}}(r) \cdot \frac{c_{p,\text{alloy}}}{3600} \cdot \frac{\partial T_{\text{bed}(r,t)}}{\partial t} = \frac{k_{\text{eff}}}{1000} \cdot \frac{1}{r} \frac{\partial}{\partial r} \left(r \frac{\partial T_{\text{bed}}}{\partial r} \right) + \dot{Q}_{\text{react}}(r) \tag{4.1}$$

The left-hand side represents the transient heat storage in the alloys bed at radial position r. The local bulk density $\rho_{\text{bulk,1D}}(r)$ varies with radial position due to the local hydrogen loading, while $c_{p,\text{alloy}}$ is assumed constant. The term $\partial T_{\text{bed}}/\partial t$ is the partial time derivative at fixed r, evaluated independently at each radial node. The first term on the right hand side described the radial heat conduction accounting for the increasing cross-sectional area with the radius. The effective thermal conductivity k_{eff} governs the rate of heat conduction, while second term $\dot{Q}_{\text{react}}(r)$ is the local heat of reaction, positive during the exothermic absorption and negative during the endothermic desorption reaction, as defined in Equation 4.2

$$\dot{Q}_{\text{react}} = -\frac{R_{\text{abs}}}{3600} \cdot \Delta H_{\text{abs}} \cdot 10^6 - \frac{R_{\text{des}}}{3600} \cdot \Delta H_{\text{des}} \cdot 10^6 \tag{4.2}$$

Since $\dot{Q}_{\text{react}}$, R_{abs} and R_{des} are declared as one-dimensional distributions over the radial domain, this equation is implicitly evaluated at each radial node by the ACM solver.R_{abs} and R_{des} are the local absorption and desorption reaction rates in kmol/m^3/h, and ΔH_{abs} (converted to kmol/m^3/s), ΔH_{des} are the respective reaction enthalpies in GJ/kmol (kJ/kmol).

Analogously to the bed, the energy balance for each radial node of the steel wall is given by:

$$\rho_{\text{steel}} \cdot \frac{c_{p,\text{steel}}}{3600} \cdot \frac{\partial T_{\text{wall}(r,t)}}{\partial t} = \frac{k_{\text{steel}}}{1000} \cdot \frac{1}{r} \frac{\partial}{\partial r} \left(r \frac{\partial T_{\text{wall}}}{\partial r} \right) \tag{4.3}$$

where ρ_{steel} and $c_{p,\text{steel}}$ are the density and specific heat capacity of the steel wall (assumed constant), and k_{steel} is its thermal conductivity. Unlike the bed energy balance, no heat source term appears, as no chemical reaction takes place in the wall.

The energy balance of the HTF treats the fluid as a single well-mixed volume:

$$M_{\mathrm{HTF}} \cdot c_{p,\mathrm{HTF}} \cdot \frac{\mathrm{d}T_{\mathrm{HTF}}}{\mathrm{d}t} = \dot{m}_{\mathrm{HTF}} \cdot c_{p,\mathrm{HTF}} \cdot (T_{\mathrm{HTF,in}} - T_{\mathrm{HTF}}) + h \cdot A_{\mathrm{tank}} \cdot (T_{\mathrm{wall,outer}} - T_{\mathrm{HTF}}) \quad (4.4)$$

The left-hand side represents the transient heat storage of the fluid. On the right-hand side, the first term accounts for the convective enthalpy flux due to the incoming HTF mass flow $\dot{m}_{\mathrm{HTF}}$ at inlet temperature $T_{\mathrm{HTF,in}}$. The second term describes the heat exchange between the outer tank wall and the fluid, governed by the heat transfer coefficient h and the outer tank surface area A_{tank}, where $T_{\mathrm{wall,outer}}$ is the temperature at the outermost wall node.

The hydrogen mass balance links the local reaction kinetics to the gas phase. Since the reaction rate $R(r)$ varies with radial position, a cross-sectional average is computed by weighting each local value by its radial position, accounting for the increasing cross-sectional area with radius:

$$R_{\mathrm{avg}} = \frac{2}{r_{\mathrm{bed}}^2} \int_0^{r_{\mathrm{bed}}} R(r) \cdot r \, \mathrm{d}r \quad (4.5)$$

This radially averaged reaction rate is then used to determine the total hydrogen mass flow exchanged between the solid and gas phase:

$$\dot{m}_{H_2,\mathrm{reaction}} = -R_{\mathrm{avg}} \cdot V_{\mathrm{bed}} \cdot M_{H_2} \quad (4.6)$$

The negative sign indicates that hydrogen absorbed by the solid ($R_{\mathrm{avg}} > 0$) represents a sink for the gas phase, and vice versa during desorption.

The reaction kinetics for the metal hydride are formulated as described in section 2.3.4, depending on the specific alloy (see 4.3.2), expressing the reaction rate R as the product of a temperature-dependent Arrhenius term $K(T)$, a pressure driving force term $F(p)$, and a the kinetic model $G(\alpha)$.

Of particular importance for the further course of this work is the equilibrium pressure calculation. At each radial node, the local absorption and desorption equilibrium pressures $p_{eq,abs}$ and $p_{eq,des}$ are computed using high-order bivariate polynomial fits in local hydrogen loading $w(r)$ and bed temperature $T_{bed}(r)$, with separate coefficient sets for absorption and desorption. The material specific polynomial coefficients (for example 18 coefficients) were obtained during the course of this work, by fitting experimental PCI data from the selected alloys, using the *MATLAB Curve Fitting Toolbox*, as described in Section 4.4. A lower bound of 1 bar is enforced via [max(1,...)] to prevent physically implausible values and ensure numerical stability. From these, the local pressure driving forces are computed as $\Delta p_{abs} = p_{Gas} - p_{eq,abs}$ and $\Delta p_{des} = p_{eq,des} - p_{Gas}$, where p_{Gas} is the current uniform gas pressure in the tank. A positive Δp_{abs} indicates absorption conditions ($p_{Gas} > p_{eq,abs}$), while a positive Δp_{des} indicates desorption conditions ($p_{eq,des} > p_{Gas}$).

The aforementioned heat exchanger, positioned externally adjacent to the tank, operates cyclically via a flowsheet task “CompressorRun”. It alternately cools the tanks to facilitate the hydrogen absorption and heats for the desorption, repeating until endtime. This scripted control defines the thermal ramp profiles and time periods for staged temperature cycling. This task makes it possible to observe and evaluate the compression based on the fundamental equations in the Tank1D model over a period of time, thereby enabling the design of a suitable compressor for the use case in Moorburg.

4.3 Material Selection

The selection of suitable hydride-forming alloys represents the fundamental decision in the development of metal hydride compressors because the thermodynamic and kinetic properties of the chosen hydride-forming alloys directly determine the operational performance, efficiency, and feasibility of the entire compression system. While many selection criteria are application-specific, such as "the maximum hydrogen supply pressure available at the source, required inlet pressure, and targeted delivery pressure" [105], a number of material parameters are of general relevance and require a fundamental understanding for an informed alloy selection. Those properties determine parameters such as absorption and desorption pressures, achievable pressure ratios, temperature ranges needed for operation, and also the speed of the reaction. In metal hydride compressors, the material itself is the active compression agent, making this selection critical to system viability.[105, 47]

In the following, these parameters are outlined, providing the foundation upon which the alloy selection for the system developed in this thesis is built.

4.3.1 Selection Criteria

In the literature, the selection of metal hydrides for compression applications is a guided by a common set of several criteria spanning thermodynamic properties (PCI characteristics, hysteresis, slope, reversible capacity), reaction kinetics, cyclic stability, resistance to gaseous impurities, and cost. To reliably assess these properties, a solid literature and data base for the specific hydride material is required, making "data availability" another selection criterion. In the following, these aspects are presented together with a brief overview of the AB_5 and AB_2 intermetallics, that are frequently cited for compression applications. [19, 23, 67, 18]

Thermodynamics:

The primary selection criterion involves matching the alloy's equilibrium pressure-temperature relationships to the desired compression application. Ideal materials exhibit plateau pressures that align with target input and output pressures within practical temperature ranges. Non-ideal properties including pressure hysteresis between absorption and desorption and plateau slope must be considered, as these factors reduce effective compression ratios and therefore productivity. [19, 67, 23]

Furthermore, a high reversible hydrogen storage capacity is desirable, as gravimetric and volumetric hydrogen storage capacities determine the size and mass of the compressor system. Higher capacity materials require less alloy mass for a given hydrogen flow rate, reducing material costs, system footprint and “energy consumption and heat losses associated with thermal cycling” [23]. Typical metal hydrides for compression applications store hydrogen at capacities ranging from 1 to 2 wt% for AB_5-type alloys to higher values for AB_2-type materials.[19, 67, 23]

Figure 4.3 illustrates pressure-composition isotherms for several AB_2-type alloys, illustrating the outlined selection criteria. The horizontal width of the plateau, representing the reversible capacity, differs for each alloy. Likewise, the plateau slope varies from a slight incline to a steep, nearly vertical line in some alloys. The vertical offset between the absorption and desorption Isotherms for the same alloy, the hysteresis, ranges from nearly overlapping curves to gaps as large as 50 bar.

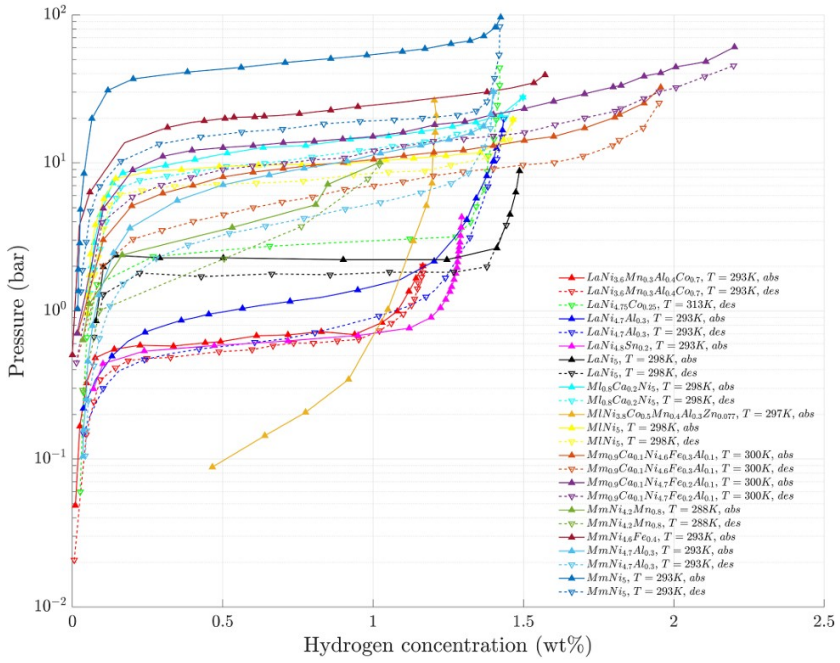

Figure 4.3: Exemplary PCT diagrams of several AB_5 alloys [67]

Multi-stage compression:

In the case, that there is no single alloy that fits the temperature-pressure criteria introduced by the operating conditions the best or that two (or more) alloys fit the lower and upper end of the working range better, a multi-stage compressor could be considered. In such a case, the selected alloys need to match in the overlapping pressure area. The desorption pressure of stage one at a high temperature must be higher than the absorption pressure of stage two at a low temperature. [19]

Kinetics:

Rapid hydrogen absorption and desorption kinetics are essential for achieving acceptable cycle times and system productivity. Materials with slow reaction rates require extended heating and cooling periods, reducing throughput and increasing operational costs. [23, 19]

Cyclic Stability:

Cyclic stability describes the ability of a metal hydride material to maintain its hydrogen storage capacity and kinetic performance over repeated absorption and desorption cycles. For practical applications, a compressor must endure thousands of cycles over its service lifetime, making this a critical selection criterion. The primary mechanism of degradation is thermodynamic disproportionation. In this process intermetallic compounds break down into into a stable, binary hydride (formed by an element with high hydrogen affinity) and a metallic phase (non-hydride-forming). Disproportionation can be triggered repetitive absorption/desorption cycling or by extended exposure to high temperatures and pressures ("thermal ageing"). This results in a reduced reversible storage capacity, a reduction of the plateau pressure and increases plateau slope, leading to a reduced compressor productivity over time. This effect is shown in Figure 4.4. [71, 67, 18]

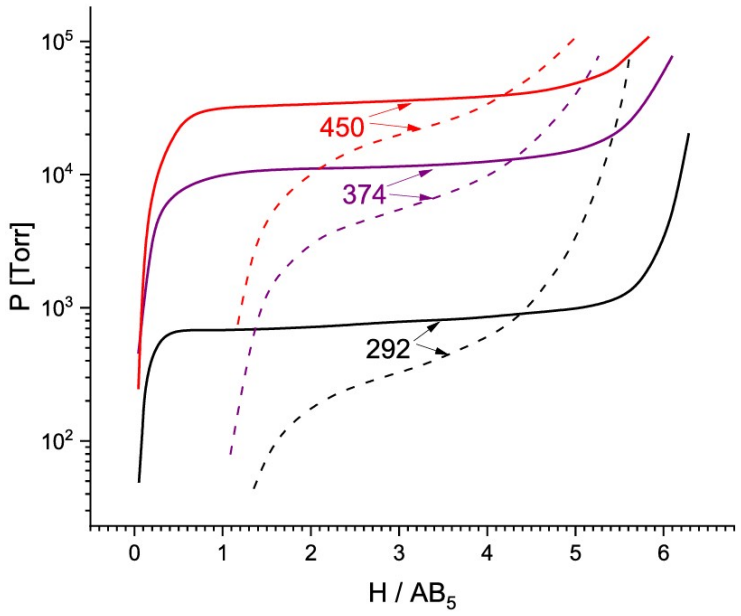

Figure 4.4: Exemplary "desorption isotherms before (solid lines) and after ageing (dashed lines) at 500 K for 1207 hours. Curve labels show the isotherms temperature in K." [18, 109]

The extent of degradation varies significantly across alloy families. For AB_5-type intermetallics measurable degradation typically appears after 20,000 to 30,000 cycles, with the possibility of sorption performance recovery by heating the material to 400°C to 500°C in a vacuum. AB_2-type alloys seem less prone to disproportionation making them attractive where long cycle life is prioritized. [66]

Gaseous impurities resistance

While metal hydrides inevitably experience the phenomena of degradation (loss of capacity) even under ideal, high-purity conditions, practical operation could introduce another form of damage to the metal hydride, leading to a drop in productivity. For hydrogen compression, that "is open-ended [using] new hydrogen for each [compression] cycle" [71], resistance to gaseous impurities is critical. The feed hydrogen can contain contaminants from production methods, in this case, water electrolysis, which can degrade performance and reliability. Four main types of damage are identified, depending on the resistance of the alloy used:

- Poisoning: Rapid (reversible) capacity loss, no influence on kinetics
- Retardation: Slowing kinetics without capacity loss (reversible)
- Reaction: Irreversible alloy corrosion
- Innocuous effects: Inert gas blanketing, leading to a (pseudo-) kinetic decrease

At a microscopic level, "poisoning" is essentially a passivation process. Impurity gases bind strongly to the active centers on the metal's surface, preventing the necessary dissociation of hydrogen molecules into atomic hydrogen (chemisorption). Consequently, improving tolerance involves either blocking these impurities or increasing the number of active centers. Surface treatments such as fluorination or the deposition of metallic catalysts have been successfully employed to slow down degradation rates in contaminated streams. This performance loss is not always irreversible, poisoned hydrides can often recover their sorption capacity through thermal regeneration, typically by heating the material to 100 to 150°C under vacuum or reduced hydrogen pressure. For water electrolysis the common impurities are oxygen and water vapor, with other production methods other impurities, such as carbon dioxide and monoxide could be present. The severity of this damage varies significantly between different alloy families. While TiFe-based materials and AB_2-type compounds are particularly prone to poisoning effects, AB_5-type alloys exhibit much higher natural tolerance. It is possible to reduce those sensitivities by e.g. surface modifications . Adding an deoxidizer to the alloy also showed improvements. [67, 71, 18, 23, 66]

Cost:

The selected (commercially available) material must be affordable at the required scale. As economic considerations are outside the scope of this work, this requirement is not further detailed. [23]

Data availability:

As the materials need to be searched for and thoroughly investigated in a literature research, data availability plays a big role in the selection of a suitable material. To select a material, information such as PCIs in a reasonable temperature and pressure range, kinetic and thermodynamic data needs to be available in a reputable paper or comparable work. A mere listing of operating pressures or temperatures in tabular form, lacking the corresponding PCI diagram, is deemed inadequate for material assessment, as does not provide the precise curve shape with information such as slope and hysteresis, even when a capacity is stated.

4.3.2 Project Specific Material Selection

Following the establishment of the technical boundary conditions for the Moorburg HGHH plant (30 - 80 bar, 35° and 46 °C available cooling and heating temperature (Table 4.1) a comprehensive literature search was conducted to identify metal-hydride alloys suitable (see 4.3.1) for the intended compression application.

The primary challenges encountered during the search stemmed the narrow available temperature span of Δ T = 11 °C (35°C–46°C) and the availability and quality of experimental data. While the temperature limits can be extended, the design objective remained to minimize deviation from existing site conditions, ruling out most metal hydrides. Simultaneously, data availability proved critical, as many sources cited only tabular works, PCIs for only few temperatures or qualitative descriptions. The searched encompassed journal articles, review paper as well as specialized databases, such as the "*Purdue Metal Hydride Toolbox*" (see 4.4.1).

The search was not restricted to specific alloy families, such as AB_2 or AB_5 and deliberately formulated with broad keywords, to ensure that potentially suitable materials were not overlooked. This methodology yielded a set of candidate alloys with sufficient PCI data for further investigations.

Hydralloy C1

Hydralloy C1 ($Ti_{0.99}Zr_{0.01}V_{0.43}Fe_{0.09}Cr_{0.05}Mn_{1.5}$) seems to be one of the most promising candidates for a possinle first stage. Its properties are described in more detail below.

Hydralloy C materials, a trademark term, are titanium-based commercially available AB_2-type alloys developed specifically as low-temperature hydride alloys for applications at ambient temperature. They are produced by the German Manufacturer GfE Metalle und Materialen GmbH [110].

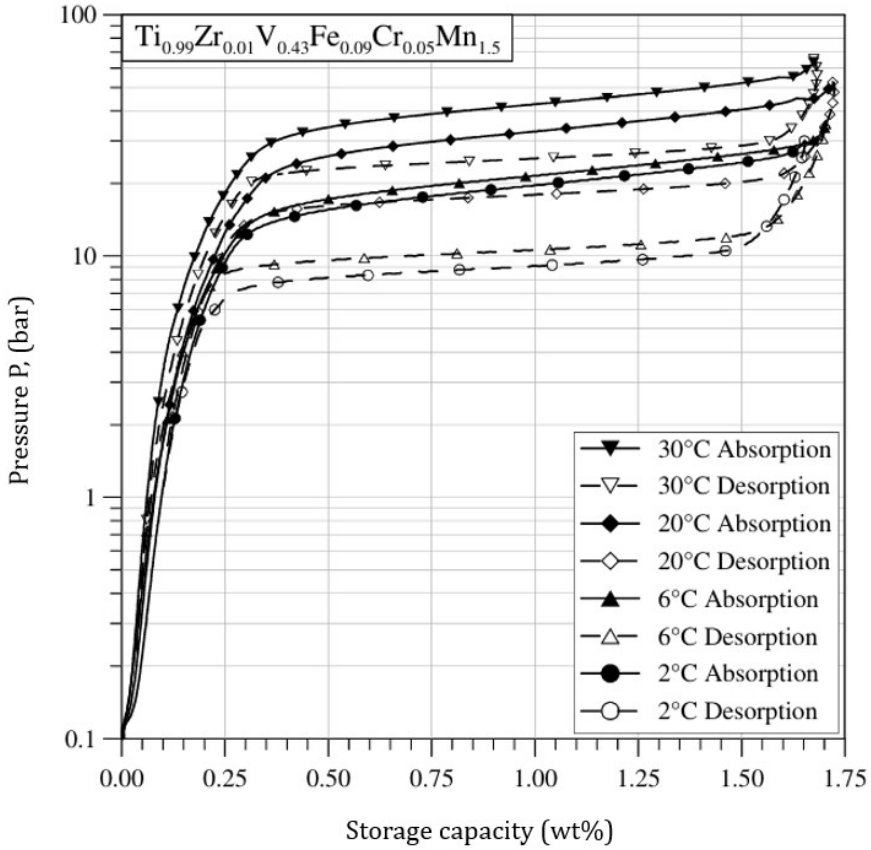

Figure 4.5: Pressure Composition Isotherms of Hydralloy C1 [73]

Literature reports PCIs for Hydralloy C1 measured between 2°C and 30°C, as illustrated in 4.5. At 6°C, the equilibrium absorption pressure reaches approximately 20 bar, whereas the equilibrium desorption pressure at 30°C is around 25 bar. The plateau slope is moderately pronounced (0.42 for absorption, 0.22 for desorption), allowing relatively stable hydrogen release over 1.75 wt% capacity without sharp pressure increases.

The somewhat more pronounced hysteresis (0.27) indicates a notable pressure gap between absorption, but remains practical for cycling. [111]

Wimmer et al. assume good cyclic stability for Hydralloy C1, based on the findings of Wanner et al., who observed only a minor 10% degradation in hydrogen capacity for Hydralloy C2 after 85,100 cycles, equivalent to 4,255 hours of operation at a half-cycle time of 150 sec.. This performance is expected to extend to Hydralloy C1, as "it belongs to the same class of AB_2 Laves phase materials" [111]. The important thermodynamic and kinetic parameters, as well as the kinetic model for absorption and desorption for Hydralloy C1, are summarized in 4.4:

Table 4.4: Material properties for Hydralloy C1 [73, 78]

Alloy	$Ti_{0.99}Zr_{0.01}V_{0.43}Fe_{0.09}Cr_{0.05}Mn_{1.5}$		
Type	AB_2		
Thermodynamics Parameter	**Symbol**	**Value**	**Unit**
Weight Percent	wt_{max}	1.75	%
Dehydriding	ΔH	25.98	kJ mol^{-1}
	ΔS	112.6	J $mol^{-1}K^{-1}$
Hydriding	ΔH	-20.12	kJ mol^{-1}
	ΔS	-97.4	J $mol^{-1}K^{-1}$
Kinetics Parameter	**Symbol**	**Value**	**Unit**
Dehydriding	A	65	s^{-1}
	E_a	29.0	kJ mol^{-1}
Hydriding	A	305	s^{-1}
	E_a	31.4	kJ mol^{-1}
Kinetic model			
Dehydriding	G(α)	1^{st} Order desorption	wt
	F(P)	$\ln(\frac{P_{eq}}{P})$	
Hydriding	G(α)	1^{st} Order absorption	$wt_{max} - wt$
	F(P)	$\ln(\frac{P}{P_{eq}})$	

The intrinsic kinetics of Hydralloy C1 were described by Lindner et al. as "sufficiently fast" [112]. The last remaining selection criterion, resistance to gaseous impurities was not mentioned in literature. Since hydrogen of grade 5 purity (99.999 mol%) can be assumed at Moorburg following deoxidization and drying, and the remaining selection criteria are well satisfied by this material, Hydralloy C1 is selected for further development in this work.

Hydralloy C5

Another promising candidate is the Hydralloy C5. Hydralloy C5 is another commercial low-temperature AB_2 manufactured by GfE Metalle und Materialien GmbH [110].

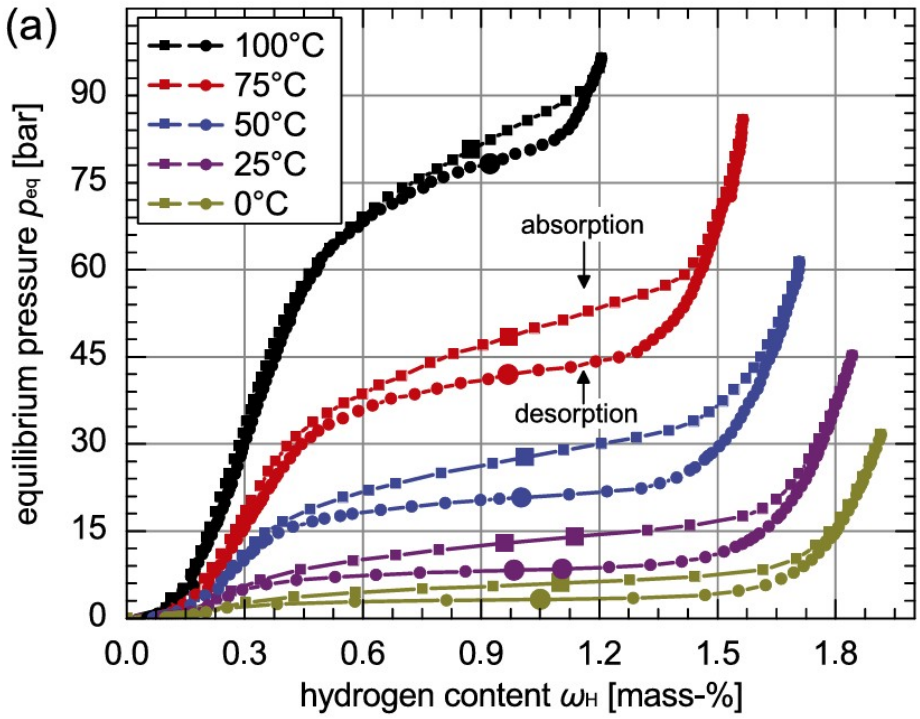

Figure 4.6: Pressure Composition Isotherms of Hydralloy C5 (Squares indicate absorption Circle indicates desorption) [113]

Herbrig et al. measured PCIs for Hydralloy C5 between 0°C and 100°C, as illustrated in 4.6. At 25°C, the equilibrium absorption pressure reaches approximately 20 bar, whereas the equilibrium desorption pressure at 75°C is around 50 bar.

Both hysteresis and plateau slope are visible, with the max. weight capacity decreasing significantly at higher temperatures being particularly noticeable (around 1.9 wt% at 0 °C to 1.2 wt% at 100°C.

Puszkiel et al. assume good cycle stability based on the findings of several studies: Pohlmann et al. cycled Hydralloy C5 pellets (up to 12.5 wt% added Expanded Natural Graphite) 85 times with intact structure (while clamped for stabilization). Dieterich et al. achieved 1000 cycles with only surface cracks. A similar Ti-Zr-V-Fe-Cr-Mn alloy showed less than 5% capacity loss after 2000 cycles or 25% (regainable) after 20000 cycles [68].

The important thermodynamic and kinetic parameters, as well as the kinetic model for absorption and desorption for Hydralloy C5, are summarized in 4.5:

Table 4.5: Material properties for Hydralloy C5 [68, 114]

Alloy	$Ti_{0.95}Zr_{0.05}Mn_{1.55}V_{0.45}Fe_{0.09}$		
Type	AB_2		
Thermodynamics Parameter	**Symbol**	**Value**	**Unit**
Weight Percent	wt_{max}	1.60	%
Dehydriding	ΔH	26.4	kJ mol^{-1}
	ΔS	107.9	J $mol^{-1}K^{-1}$
Hydriding	ΔH	-20.8	kJ mol^{-1}
	ΔS	-92.9	J $mol^{-1}K^{-1}$
Kinetics Parameter	**Symbol**	**Value**	**Unit**
Dehydriding	A	527.6	s^{-1}
	E_a	22.0	kJ mol^{-1}
Hydriding	A	11.8	s^{-1}
	E_a	11.3	kJ mol^{-1}
Kinetic model			
Dehydriding	G(α)	$4 \cdot (\alpha)^{2.8}$	
	F(P)	$\frac{P_{eq}-P}{P_{eq}}$	
Hydriding	G(α)	$4 \cdot (1-\alpha)^{2.8}$	
	F(P)	$\frac{P-P_{eq}}{P_{eq}}$	

Hydralloy C5 also satisfies the selection criteria, albeit requiring higher temperatures to achieve the same pressure levels as Hydralloy C1. This material is likewise incorporated into the model and considered in the further analysis.

Ti1.1CrMn

$Ti_{1.1}CrMn$ seems to be the most promising candidate for a possible second stage. Its properties are described in more detail and summarized below (4.6). This specific $Ti_{1.1}CrMn$ was manufactured by Japan Metals & Chemicals Co.,Ltd (JMC). The material has been utilized for automobile applications, having the potential to reach high equilibrium pressures at comparatively moderate temperatures.

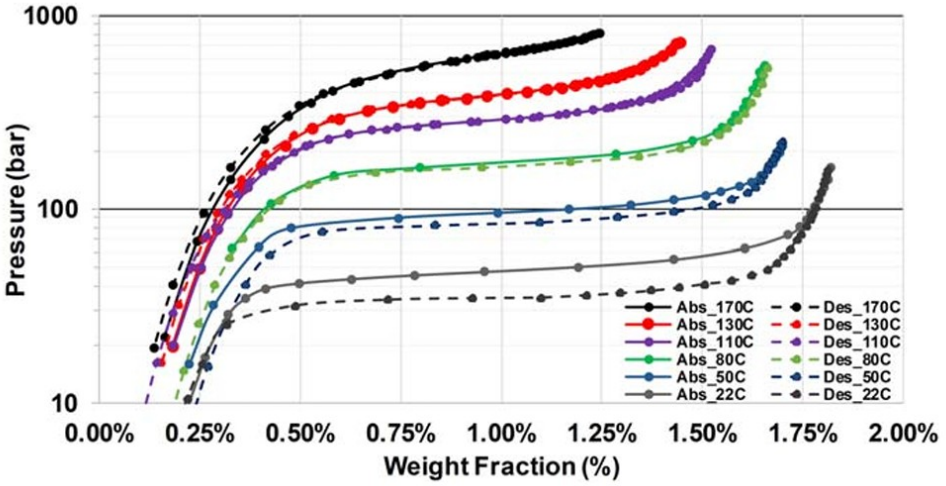

Figure 4.7: Pressure Composition Isotherms of $Ti_{1.1}CrMn$ [115]

As illustrated in 4.7, PCIs for 22°C to 170°C were measured. At 22°C, the equilibrium absorption pressure reaches approximately 50 bar, whereas the equilibrium desorption pressure at 80°C is around 180 bar. The temperatures required to achieve these pressures are much lower than those required for comparable alloys. It is also noticeable that there is neither significant hysteresis ($\frac{P_{abs}}{P_{des}}$ = 0.34 at 22 °C, 0.013 - 0.023 over 110°C) nor a high plateau slope, as well as a high weight capacity up until high temperatures. [115]

The cycle performance was of $Ti_{1.1}$ was tested by Corgnale et al, resulting in 20 cycles with essentially no degradation. [115].

Table 4.6: Material properties for $Ti_{1.1}CrMn$ [116, 117, 115, 118, 119]

Alloy	$Ti_{0.99}Zr_{0.01}V_{0.43}Fe_{0.09}Cr_{0.05}Mn_{1.5}$		
Type	AB_2		
Thermodynamics Parameter	**Symbol**	**Value**	**Unit**
Weight Percent	wt_{max}	1.75	%
Dehydriding	ΔH	24.5	kJ mol^{-1}
	ΔS	114.9	J $mol^{-1}K^{-1}$
Hydriding	ΔH	-14.7	kJ mol^{-1}
	ΔS	-92.2	J $mol^{-1}K^{-1}$
Kinetics Parameter	**Symbol**	**Value**	**Unit**
Dehydriding	A	300	s^{-1}
	E_a	20.5	kJ mol^{-1}
Hydriding	A	150	s^{-1}
	E_a	20.7	kJ mol^{-1}
Kinetic model			
Dehydriding	G(α)	1^{st} Order desorption	wt
	F(P)	$\ln(\frac{P_{eq}}{P})$	
Hydriding	G(α)	1^{st} Order absorption	$wt_{max} - wt$
	F(P)	$\ln(\frac{P}{P_{eq}})$	

Kojima et al. investigated the kinetics of $Ti_{1.1}CrMn$, describing them as sufficient, with absorption to 100% (between 33 and 0.1 MPa at 296 K) being accomplished in 60 sec., the desorption taking about 300 sec [120].

While $Ti_{1.1}CrMn$ seems like an ideal candidate for a second stage, it must be noted, that the material ignites in the presence of air or moisture, [making] its handling [...] both difficult and dangerous [117]. Despite this, due to its excellent fitting of the other selection parameters, $Ti_{1.1CrMn}$ will also be included into the ACM model.

4.4 Isotherm Data Preparation

In order to proceed with the compressor design, it was first necessary to prepare the thermodynamic data of the selected alloys for it to be consistent and sufficiently comprehensive. As described in section 2.3.3, Pressure-composition isotherms (PCIs) provide direct graphical insight into achievable pressure ranges at different temperatures as well as several other parameters, such as the corresponding hydrogen storage capacities. Many of those parameters (storage capacity, amount of sloping and hysteresis) were already considered in the subsections 4.3.2, 4.3.2 and 4.3.2.

A particular challenge in this context is that PCIs data in the literature are often only available for a limited set of temperatures. This is especially true for the material Hydralloy C1, for which published measurements for absorption and desorption isotherms cover only a narrow range from 2 to 30 °C, leaving significant gaps in the temperature regime relevant for the Moorburg application. To address this limitation, both candidate materials were implemented in a Matlab-based metal hydride database in order to obtain PCI-curves at additional temperatures beyond those reported experimentally, using the thermodynamic model within the database.

4.4.1 Purdue Metal Hydride Toolbox

The mentioned database, already utilized in the material selection process, is the Purdue Metal Hydride Toolbox [78]. an open-source, object-oriented Matlab toolbox specifically developed for the analysis of metal hydride thermal systems. The toolbox couples an extensive materials database with physically based models for equilibrium thermodynamics, reaction kinetics, and thermophysical properties, and thus provides a coherent framework to generate pressure–composition–temperature (PCT) relationships over wide operating ranges even when only limited experimental data are available. This was essential for the next steps in designing a MHC, as the literature datasets for the considered alloys either did not cover the full temperature range of interest or provided too sparse isotherms, which is insufficient for robust compressor design.[78]

The underlying hydride database in the toolbox contains more than 300 materials compiled from approximately 150 literature sources, including the former Sandia hydride database. In the toolobox a equilibrium model and a reaction rate model is included. For each hydride, the entry typically includes at least the hydride type (e.g. AB_2, AB_5), alloy composition, reversible hydrogen capacity, and desorption thermodynamic parameters (enthalpy and entropy of formation), and may additionally include absorption thermody-

namics, plateau slope, hysteresis, critical temperature, thermophysical properties, and kinetic parameters. Where full absorption thermodynamics are not directly available, the toolbox can work with partially defined materials by using combinations of available quantities (e.g. one of enthalpy/entropy plus hysteresis or critical temperature) and type-dependent default values to construct a physically plausible, though approximate, PCI representation. This flexibility allows the inclusion of materials for which only incomplete literature data exist, which is, like for both selected alloys in this thesis, often the case for technically relevant alloys.[78]

The equilibrium model was designed to satisfy a set of physical criteria for realistic (representation of relevant features), physically "plausible thermodynamic behavior with minimal data, while also being able to accommodate additional data". [78] lists the following criteria:

1. $p_{eq,a}(T) \geq p_{eq,d}(T)$ for all x at any T
2. $p_{eq}(x \to 1) \to$ High pressure for all T
3. $p_{eq}(x \to 0) \to$ Low pressure for all T
4. No hysteresis or phase transition at $T > T_c$
5. Diminishing two-phase region width as $T \to T_c$
6. Reversion to a mostly straight plateau model at $T \ll T_c$
7. Definable with minimal inputs (ΔH_d and ΔS_d) but able to accommodate additional information (plateau slope, hysteresis, absorption thermodynamics, plateau widths, critical temperature) if available
8. Extensible outside the fitted data range without oscillatory, unstable, or non-physical behavior or a violation of any of the prior criteria

The model requires the equilibrium absorption pressure$p_{eq,a}(T)$ to be greater than or equal to the desorption pressure $p_{eq,d}(T)$ for all compositions x and temperatures T. This reflects physical reality in hydride systems where absorption occurs at higher pressures than desorption, ensuring a well-defined reaction direction.[78]

As composition x approaches maximum capacity ($x \to 1$), equilibrium pressure approaches high pressure across all temperatures T. This captures the steep pressure rise in the β-phase of the isotherms, reflecting correct boundary behavior. Conversely, as the composition approaches zero ($x \to 0$), the equilibrium pressure must tend to low values across all temperatures, aligning with the initial linear rise in α-phase absorption. [78]

Above the critical temperature ($T > T_c$), no hysteresis or distinct phase transition should occur, producing smooth single-phase isotherms without plateau regions.[78]

As temperature approaches the critical temperature ($T \to T_c$), the width of the (two-phase) plateau region continuously diminishes, consistent with the critical point where α and β phases merge.[78]

Far below the critical temperature ($T \ll T_c$), the model reverts to a nearly straight plateau, representing ideal coexistence of hydride phases with minimal slope.[78]

The model must function with minimal thermodynamic input (desorption enthalpy ΔH_d and entropy ΔS_d) while accommodating additional data such as plateau slope, hysteresis, absorption thermodynamics, plateau boundaries, or critical temperature when available. [78]

The model remains numerically stable and physically plausible when applied outside the temperature/composition range of the original fitting data, avoiding oscillations, instability, non-physical results, or violations of prior criteria, thus ensuring reliability for the design.[78]

These criteria must be combined in an equilibrium model. The model developed by the authors calculates pressure $p_{eq}(x, T)$ based on chemical potential, using a linear model in the (two-phase) plateau region and a regular solution model in the single-phase regions, with the transition at their coincident and tangent point for seamless, physics-based continuity. The goal of this approach was to "define a model which is physically plausible and which can still be robustly applied to the numerous and varied hydrides in [the] database", while accepting the fact that due to the reduction in the fitting parameters, the model "will not necessarily provide [such a] close fit to the isotherm" [78] as other models.

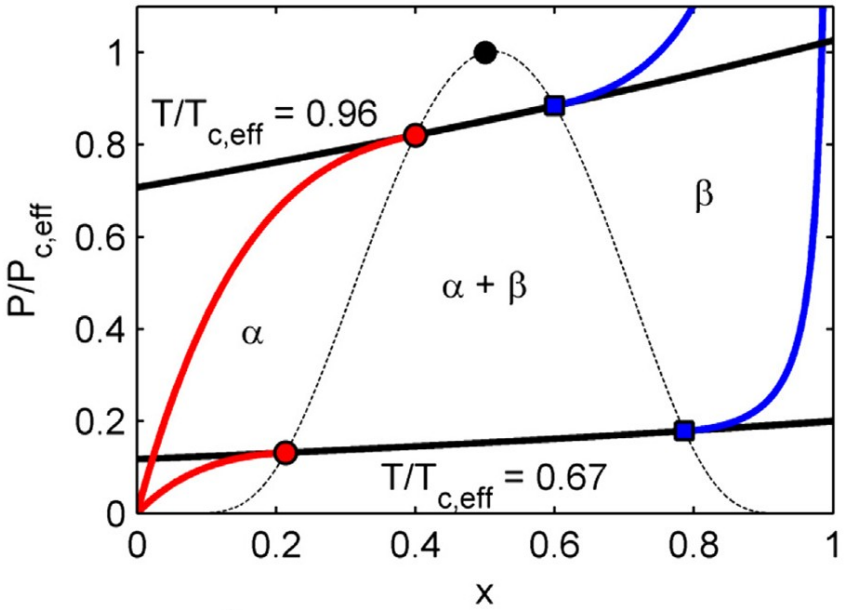

Figure 4.8: Equilibrium pressure model regions [78]

In the two-phase region, the chemical potential μ_{a+b} follows a linear profile dependent on enthalpy ΔH, entropy (ΔS), and phase interaction energy (A), as Equation 4.7 expresses and shown by the straight lines depicted in Figure 4.8. The two-phase region in the model lasts until an effective critical temperature $T_{c,eff}$, beyond which there is no flat plateau and the phases blend smoothly.[78]

$$\mu_{\alpha+\beta} = \Delta H - T\Delta S + A(x - 0.5) \tag{4.7}$$

In both single-phase regions, a regular solution model is applied to satisfy the criteria 2, 3, and 5, that were not addressed by the linear model, expressed by the Equations 4.8 and 4.10. The transition between single-phase and two-phase regions is defined as the point where the chemical potentials from the regular solution (derivative) and linear model share identical values. [78]

$$\mu_\alpha = \mu_{\alpha,0} + (1 - 2x)\Omega + RTln\left(\frac{x}{1-x}\right) \tag{4.8}$$

$$\mu_\beta = \mu_{\beta,0} + (1-2x)\Omega + RTln\left(\frac{x}{1-x}\right) \tag{4.9}$$

The equilibrium pressure is then calculated from the chemical potential. The equilibrium model extends to materials with multiple plateaus, provided sufficient isotherm data is available for the additional parameters.[78]

$$p_{eq} = p_0 exp\left(\frac{\mu(x,T)}{RT}\right) \tag{4.10}$$

The authors compiled isotherm curves for several dozen hydrides and compared them with the data from the literature, with the model providing a reliable fit to measurements across diverse material classes, even with sparse input data. [78]

The model includes further underlying equations as well as a kinetics model, however, these are beyond the scope of this work, as the toolbox's primary purpose for the following working steps is to generate isotherms for the selected alloys in Subsection 4.3.2. [78]

4.4.2 Alloy Integration into the Purdue Toolbox

Building on the comprehensive Metal Hydride Toolbox database, the next step involved adding the selected alloys into the Toolbox to generate isotherms. This was done, as the available PCI data for these alloys is limited, either with no data in the needed temperature range or with isotherms being scarce regarding the amount of data points recorded for an isotherm or the total of the measured isotherms. After the generation of the isotherms, the fit can be compared visually by overlaying the generated curves with measured data and adjust parameters such as plateau slope, to optimize the alignment under the model's physical constraints. The following describes in more detail the insertion of the selected alloys Hydralloy C1 and $Ti1.1CrMn$ types into the database as well as the fit assessment of the modeled isotherms.

The PCI data in the literature for the selected alloy Hydralloy C1 ranged between 2 and 30 °C for both absorption and desorption. For absorption, cooling between these temperature values is within the expected range. The heating temperatures required to reach 80 bar for MHC are expected to be significantly above 30 °C.

The model used in Aspen Custom Modeler in the further course of the work is based on a test compressor at the Helmholtz Zentrum hereon, which requires temperatures of 10 °C and 90 °C for compression from 30 to 60 bar, with Hydralloy C5 as chosen metal hydride. Despite the selection of another alloy (Hydralloy C1) selected for this work, besides Hydralloy C5, due to the simularities of the alloys, it can be assumed that temperatures higher than 30°C will be required to reach the desired pressure of 80 bar.

To add a new alloy to the toolbox, the relevant data is entered into a txt.mh file for the corresponding alloy, with Hydralloy C1 already being available in the database. The source [121] is listed for the enthalpy and entropy data in the existing entry, the hydriding enthalpy, slope and the hysteresis entry ln(Pabs/Pdes) has been adjusted for better alignment with the utilized literature isotherm data. Since the isotherms in the literature data have a slightly different shape, the maximum weight capacity was reduced in order to shift the entire graph to the right on the x-axis and align both datasets. The parameters used to generate the isotherms are listed in Table 4.7, while the resulting isotherms are shown in Figure 4.9.

Table 4.7: Thermodynamics parameter for Hydralloy C1 (Purdue Toolbox)

Alloy	$Ti_{0.99}Zr_{0.01}V_{0.43}Fe_{0.09}Cr_{0.05}Mn_{1.5}$	
Type	AB_2	
Thermodynamics Parameter		**Unit**
	Weight Percent	1.65 %
Dehydriding	ΔH	-25.98 kJ mol^{-1}
	ΔS	-112.6 J mol^{-1}K^{-1}
	slope	0.55
Hydriding	ΔH	-19.2 kJ mol^{-1}
	ΔS	-97.4 J mol^{-1}K^{-1}
	ln(Pa/Pd)	0.5

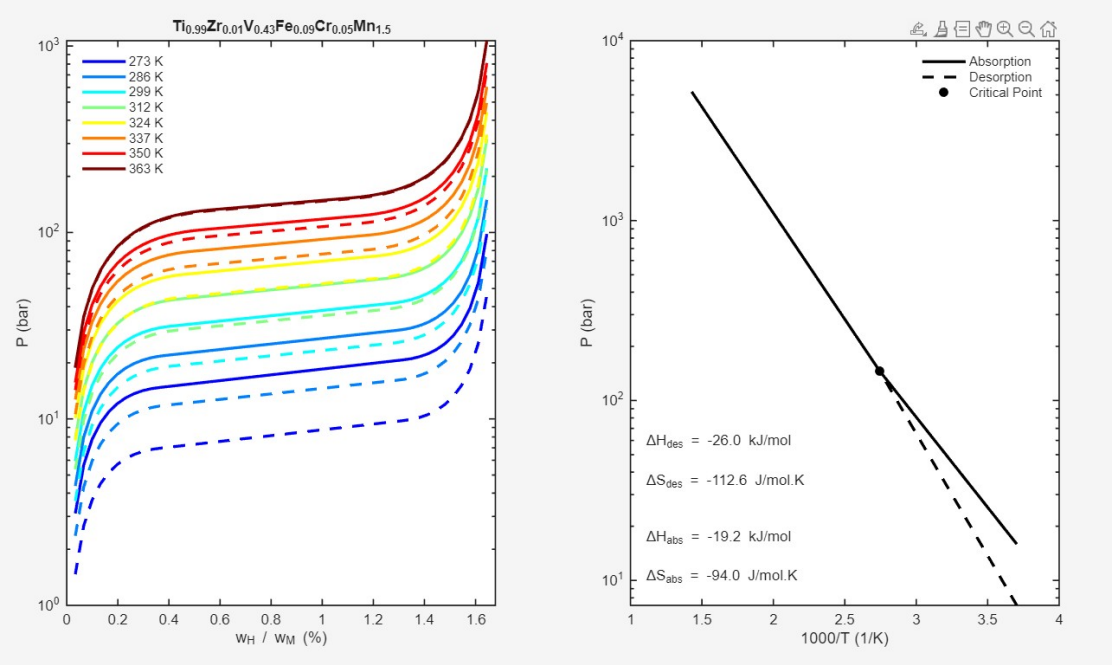

Figure 4.9: Purdue Toolbox: PCI Hydralloy C1

Figure 4.10 shows the values of the existing literature of [73] compared to the isotherms generated by the toolbox in the expected temperature ranges for absorption and desorption. As a high goodness-of-fit in the plateau (two-phase) region is critical for both absorption and desorption isotherms to determine the equilibrium pressures, the α-phase fit holds particular importance for absorption, as the isotherm rises through the α phase directly affecting the plateau onset pressure. The same applies to the fit of the β-phase for desorption.

Visually, the Figure 4.10 shows, that the model fits literature data well, particularly for absorption, with minor deviations limited to the high weight fraction region. Desorption shows acceptable agreement overall, though with greater deviations at low and high weight fractions. The coefficient of determination R^2 can further quantify the deviation of the generated isotherms from the literature values. For the individual absorption isotherms shown, the coefficient of determination R^2 ranges between 0.9696 and 0.9868, with the values rising as the temperature increases. The isotherm for 20 °C is an outlier, as can also be seen in Figure 4.10a, since the literature range for the β-phase does not increase as sharply. In desorption, too, the values of the coefficient of determination rise steadily with increasing temperature. As expected, however, the values are lower than those for absorption, with the lowest values being 0.6271 and 0.9503. Visually, it

can be seen in Figure 4.10b that as the temperature rises, the maximum weight capacity of the literature data decreases, which the thermodynamic model underestimates at lower temperatures, with an improvement in fit at higher temperatures, consistent with the R^2 values. Overall the values indicate good agreement, especially for the absorption, with the offsets in single-phase regions attributable to experimental variability.

Using the extended temperature range, the suitability of the material as a metal hydride for the to be designed compressor, either across the full pressure range or as the first stage material, can be reassessed. Figure 4.10a indicates that hydrogen absorption is feasible at 30 bar under moderate temperatures of 15 to 20 °C. Figure 4.10b reveals that desorption to reach the target pressure of 80 bar requires temperatures of around 70 °C. Thus, Hydralloy C1 remains a viable candidate, with utilization in the first compression stage preferred given the constrained temperature window.

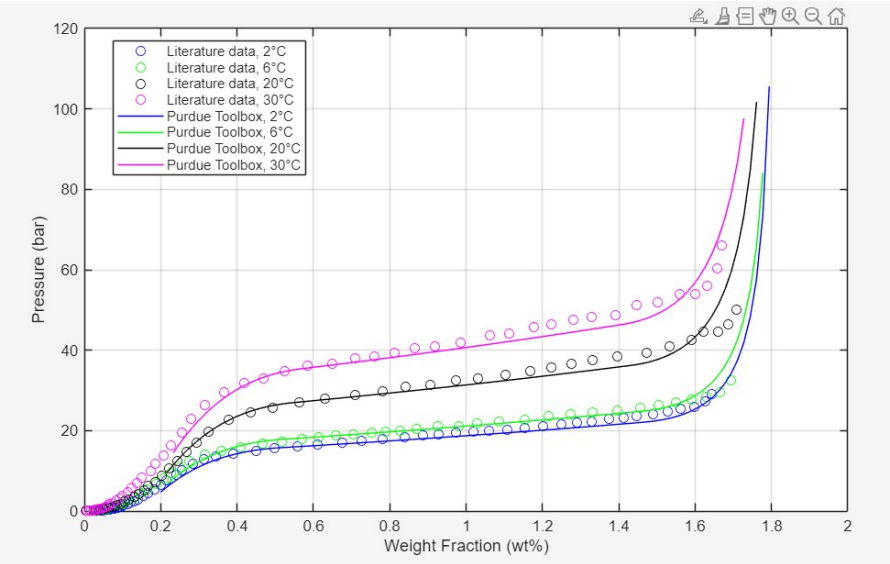

(a) Absorption Hydralloy C1

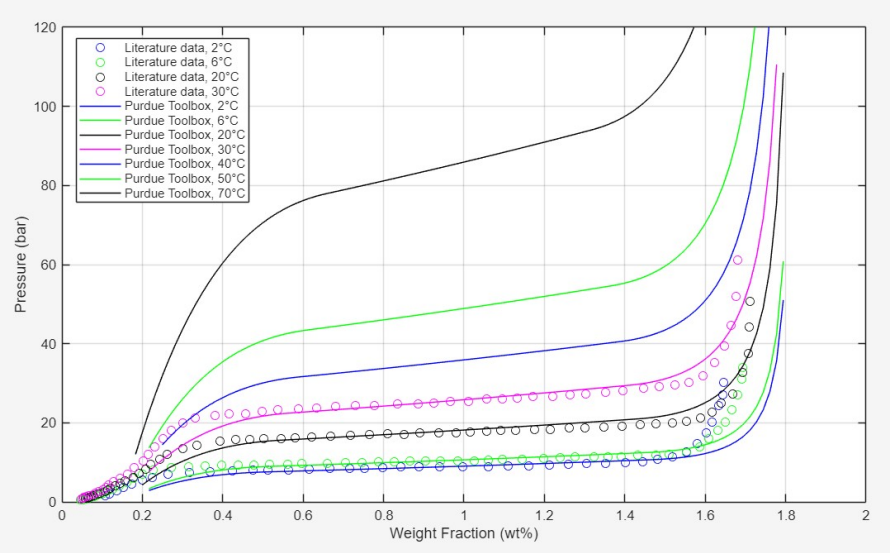

(b) Desorption Hydralloy C1

Figure 4.10: Comparison of literature data and Purdue Toolbox for Hydralloy C1

Literature data for $Ti_{1.1}CrMn$ already covers a wide temperature range of isotherms. However, isotherms in the low-temperature range, essential for assessing suitability across the full pressure range, are lacking. These isotherms can again be generated using the thermodynamic model within the Toolbox.

For this purpose, the steps previously performed for material Hydralloy C1 are repeated, starting with the creation of a txt file into which the thermodynamic data is inserted. The thermodynamic data was taken from [115], whereby data was also adjusted here to achieve better alignment with the literature isotherm data. Since the isotherms in the literature data have a slightly different shape, the maximum weight capacity was reduced in order to shift the entire graph to the right on the x-axis and align both datasets. The parameters used to generate the isotherms are listed in Table 4.8, while the resulting isotherms are shown in Figure 4.11.

Table 4.8: Thermodynamics parameter for $Ti_{1.1}CrMn$ (Purdue Toolbox)

Alloy	$Ti_{1.1}CrMn$	
Type	AB_2	
Thermodynamics Parameter		**Unit**
	Weight Percent	1.62 %
Dehydriding	ΔH	-22.9 kJ mol^{-1}
	ΔS	-107.8 J mol^{-1}K^{-1}
	slope	0.6
Hydriding	ΔH	-21.3 kJ mol^{-1}
	ΔS	-102.16 J mol^{-1}K^{-1}
	ln(Pa/Pd)	0.12

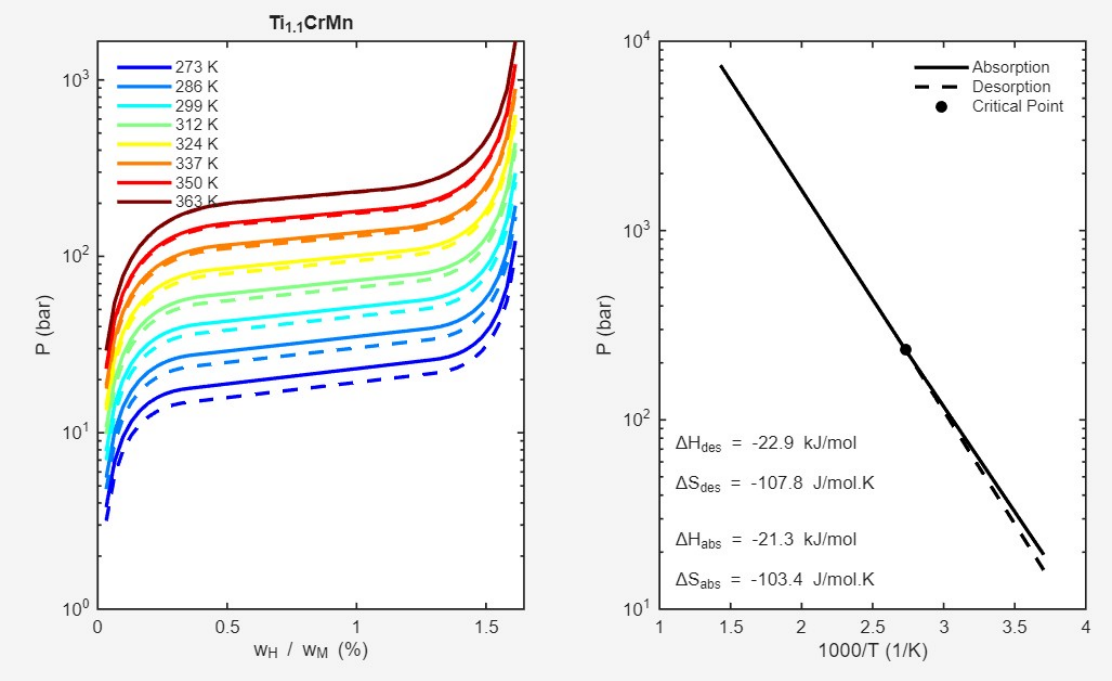

Figure 4.11: Purdue Toolbox: PCI $Ti_{1.1}CrMn$

Figure 4.12 compares literature values from [115] with Toolbox generated isotherms across expected temperature ranges for absorption and desorption. Visually, both processes exhibit excellent agreement in the plateau region, while single-phase regions show some systematic offsets. With $Ti_{1.1}CrMn$, it is even more apparent than with Hydralloy C5 that a compromise must be made when setting a value for the maximum weight capacity , as the thermodynamic model overestimates this at low temperatures and underestimates it at higher temperatures. For the absorption isotherms shown, the coefficient of determination R^2 ranges between 0.9059 and 0.9850, for desorption it ranges between 0.8916 and 0.9908. The coefficient of determination values again show an overall good agreement.

A reassessment of the alloy $Ti_{1.1}CrMn$, to determine its suitability across the full pressure range or as a material for the second compression stage, can now be performed using the modeled isotherms. Figure 4.12a shows that hydrogen absorption at 30 bar is feasible at around 10°C. Given the constrained temperature window, however, its application as a second-stage material appears more appropriate, as desorption at 80 bar is already possible at around 50 °C.

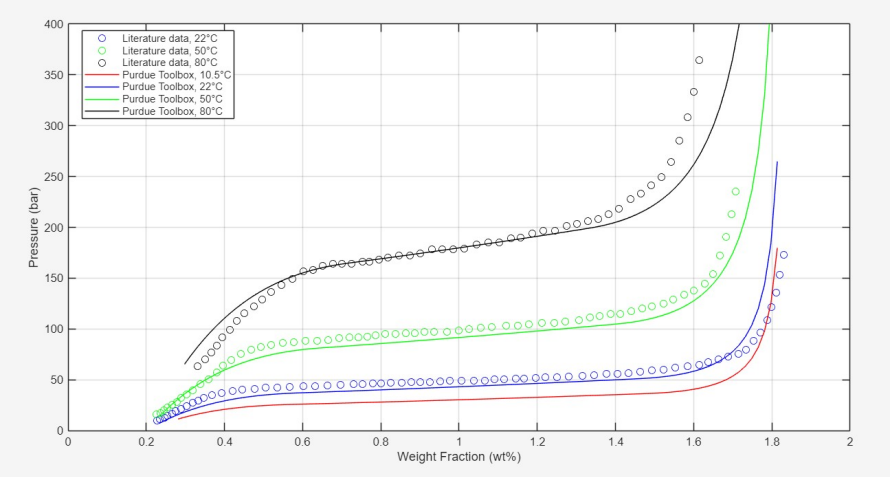

(a) Absorption $Ti_{1.1}CrMn$

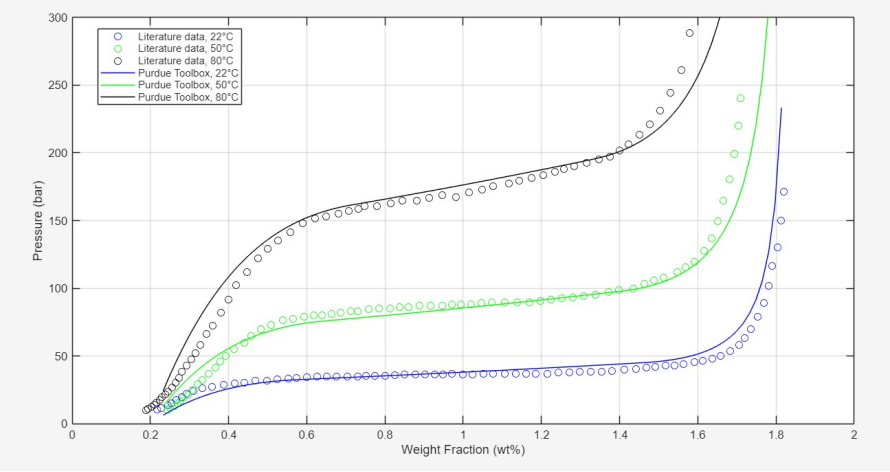

(b) Desorption $Ti_{1.1}CrMn$

Figure 4.12: Comparison of literature data and Purdue Toolbox for $Ti_{1.1}CrMn$

As the other selected alloy Hydralloy C5 is used in materials research at the Helmholtz Zentrum hereon, a wide range of isotherms has been measured, eliminating the need to output further isotherms from the toolbox.

The generated absorption and desorption isotherms for Hydralloy C1 and $Ti_{1.1}CrMn$ exhibit acceptable alignment with literature data across the examined temperature ranges, therefore a good fit is assumed for the required temperatures at which no literature data is available.

4.4.3 Polynomial Approximation of Pressure-Composition Isotherms

These isotherm data sets must now be integrated into the Aspen Custom Modeler (ACM) framework to compute equilibrium pressures p_{eq} for any given temperature T and hydrogen saturation X. The optimal form is a functional relationship $p_{eq}(X, T)$, implemented in ACM as a polynomial fit. Using the programming and numeric computing platform MATLAB and its application Curvefitter, a three-dimensional (3D) surface was constructed from the isotherm data, over which a polynomial was fitted to yield the continuous $p_{eq}(X, T)$ function. This was performed for all three selected alloys, as shown below.

4.4.4 Polynomial Approximation for Hydralloy C1

The polynomials describing the absorption and desorption isotherms of Hydralloy C1 produced the best fit using a 5th-degree polynomial in X (wt%) and 3rd-degree in T (Temperature T). Higher T-degrees yielded poorer results, with 5th-degree being the maximum. Further refinement was achieved with adjusted fit options. The resulting surface plots are shown in Figures 4.13 and 4.14, with the polynomial representing both absorption and desorption displayed in Equation 4.11.

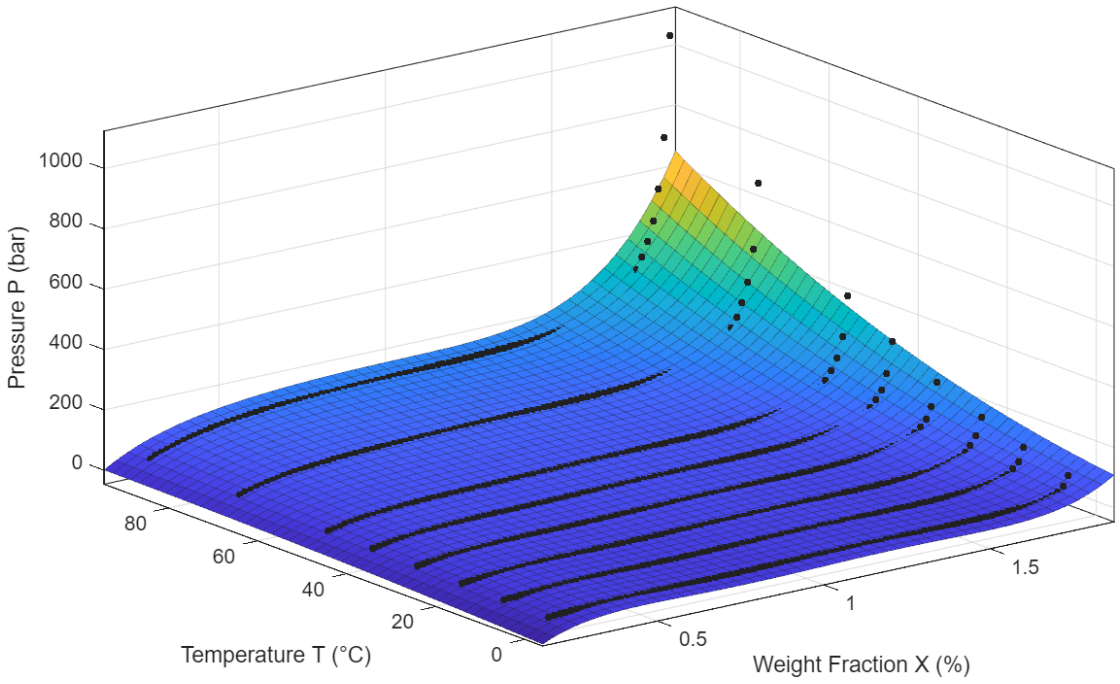

Figure 4.13: Polynomial fit: Absorption Hydralloy C1

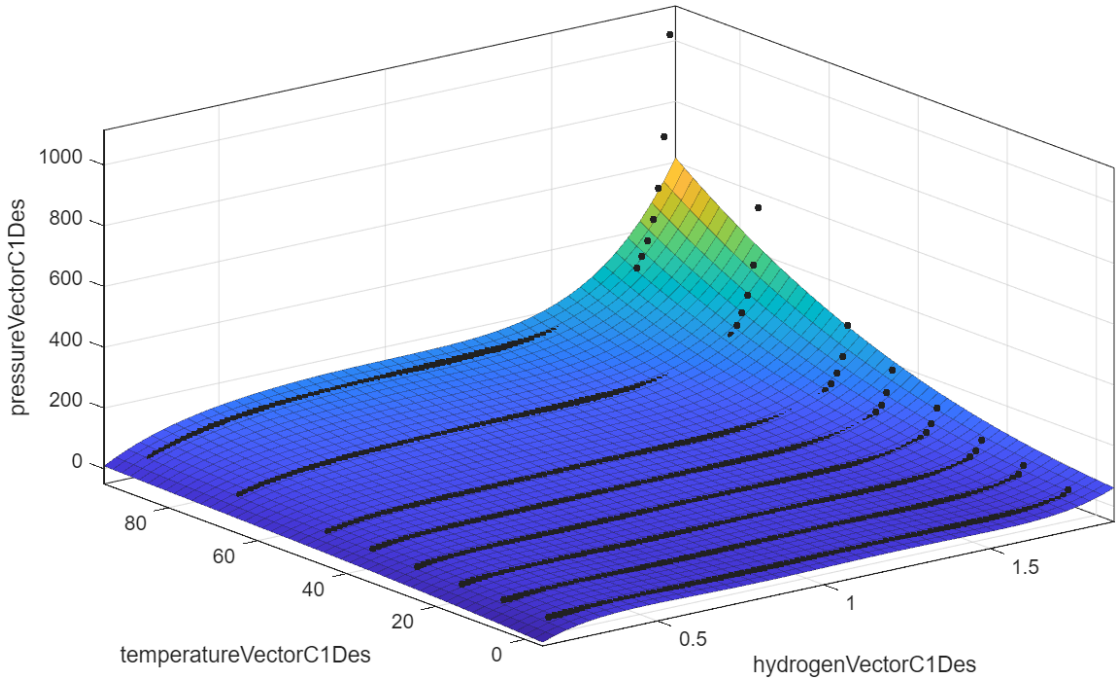

Figure 4.14: Polynomial fit: Desorption Hydralloy C1

$$
\begin{aligned}
f(x,y) = {} & p_{00} + p_{10}x + p_{01}T + p_{20}x^2 + p_{11}xT + p_{02}T^2 \\
& + p_{30}x^3 + p_{21}x^2T + p_{12}xT^2 + p_{03}T^3 + p_{40}x^4 \\
& + p_{31}x^3T + p_{22}x^2T^2 + p_{13}xT^3 + p_{50}x^5 \\
& + p_{41}x^4T + p_{32}x^3T^2 + p_{23}x^2T^3
\end{aligned}
\tag{4.11}
$$

Curve Fitter provides built-in goodness-of-fit metrics including e.g. R^2 and Root Mean Square Error (RMSE). Both figures 4.13 and 4.14 reveal that the literature data at high weight fractions exhibit steeper gradients, slightly reducing R^2 values. In this fit, R^2 reaches 0.9783 for the absorption fit and 0.979 for desorption fit, indicating good agreement between surface and isotherms. The polynomial, with coefficients determined via Curve Fitter (Table 4.9), enables calculation of equilibrium pressures across all weight fractions X and temperatures T, as required for the modeling of the Metal hydride compressor (MHC) in Aspen Custom Modeler (ACM).

Table 4.9: Polynomial Surface Fit (poly53): Absorption and desorption Hydralloy C1

Coefficient	Absorption	Desorption
p_{00}	−163.460	−133.3100
p_{10}	1198.7000	935.5200
p_{01}	1.5503	1.9575
p_{20}	−2967.3000	−2279.1000
p_{11}	−7.1271	−9.1700
p_{02}	−0.0142	−0.0222
p_{30}	3412.6000	2570.1000
p_{21}	14.4410	16.5440
p_{12}	0.0791	0.1060
p_{03}	−2.0017	3.7613
p_{40}	−1837.4000	−1356.4000
p_{31}	−11.3120	−11.8430
p_{22}	−0.0938	−0.1250
p_{13}	3.8026	2.8938
p_{50}	374.5800	271.0900
p_{41}	3.0569	2.9601
p_{32}	0.0342	0.0443
p_{23}	1.8837	2.6249
R^2	0.9783	0.9790

4.4.5 Polynomial Approximation for $Ti_{1.1}CrMn$

After inserting the absorption and desorption isotherms for Ti1.1CrMn, an optimal fit is again obtained for a polynomial of 5th degree in X and 3rd degree in T, with poorer results for a higher degree in X. Further refinement was achieved with adjusted fit options. The resulting surface plots are shown in Figures 4.15 and 4.16, with the polynomial representing both absorption and desorption displayed in Equation 4.12.

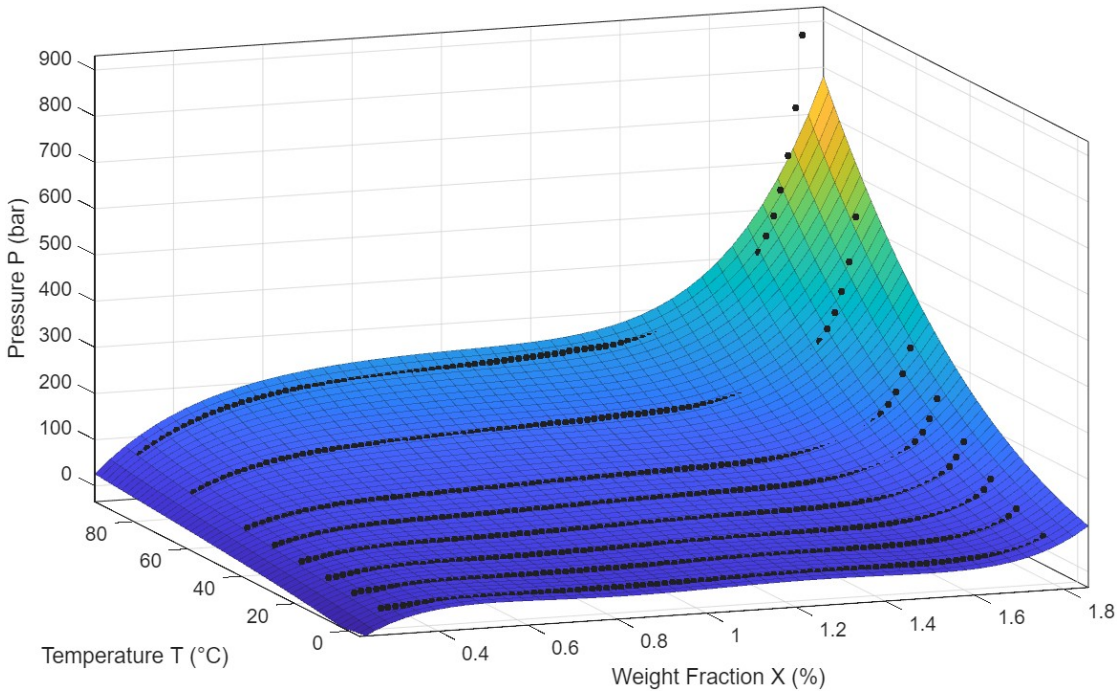

Figure 4.15: Polynomial fit: Absorption $Ti_{1.1}CrMn$

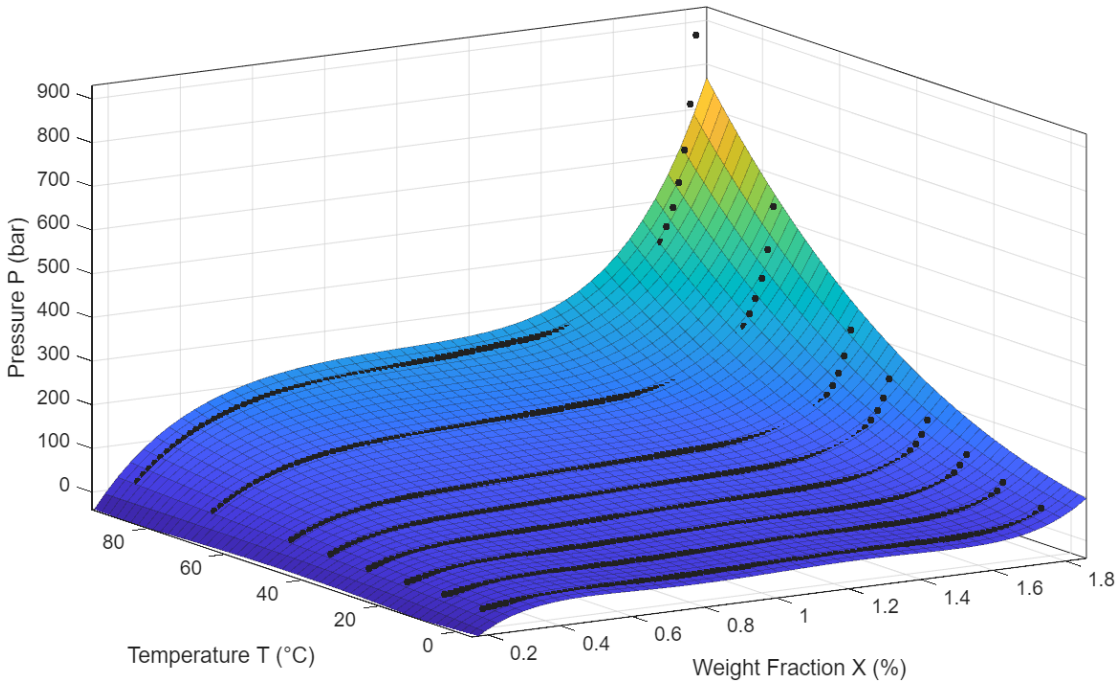

Figure 4.16: Polynomial fit: Desorption $Ti_{1.1}CrMn$

$$
\begin{aligned}
f(x,y) = {} & p_{00} + p_{10}T + p_{01}T + p_{20}x^2 + p_{11}xT + p_{02}T^2 \\
& + p_{30}x^3 + p_{21}x^2T + p_{12}xT^2 + p_{03}T^3 + p_{40}x^4 \\
& + p_{31}x^3T + p_{22}x^2T^2 + p_{13}xT^3 + p_{50}x^5 \\
& + p_{41}x^4T + p_{32}x^3T^2 + p_{23}x^2T^3
\end{aligned}
\tag{4.12}
$$

The isotherms of both figures 4.15 and 4.16 again exhibit a steeper gradient at high weight fractions compared to the polynomial surface. In the fit shown in the Figures, the values of R^2 are 0.9787 for the absorption fit and 0.97836 for desorption. Excluding the two rightmost isotherm data points (corresponding to the highest weight fractions X) from the fit, R^2 reaches 0.99522 for absorption and 0.99501 for desorption, illustrating an excellent fit between polynomial surface and isotherms. The coefficients determined via Curve Fitter are shown in Table 4.10, to be implemented in in ACM model.

Table 4.10: Polynomial Surface Fit (poly53): Absorption and desorption $Ti_{1.1}CrMn$

Coefficient	**Absorption**	**Desorption**
p_{00}	−392.3200	−248.9800
p_{10}	2536.0000	1760.3000
p_{01}	3.8545	2.0469
p_{20}	−5844.8000	−4281.5000
p_{11}	−17.3740	−9.5747
p_{02}	−0.0353	−0.0291
p_{30}	6326.5000	4842.2000
p_{21}	30.7780	19.0650
p_{12}	0.1651	0.1461
p_{03}	1.2072	3.9092
p_{40}	−3235.9000	−2565.7000
p_{31}	−21.8710	−14.4900
p_{22}	−0.1855	−0.1679
p_{13}	4.1000	5.8582
p_{50}	630.9800	515.0000
p_{41}	5.4578	3.8022
p_{32}	0.0641	0.0586
p_{23}	2.4716	1.9664
R^2	0.9787	0.9784

4.4.6 Polynomial Approximation of Hydralloy C5

For Hydralloy C5, a alternative approach was employed, distinct from the previous approach used for Hydralloy C1 and $Ti_{1.1}CrMn$. The publication by Herbrig et al. [113] provides two polynomials representing (Equations 4.13 and 4.14)the surface fit over measured absorption and desorption isotherms, whose coefficients were further refined as a custom fit in Curve Fitter. Due to the larger dataset and direct access to raw data points, avoiding digitization from diagrams, the PCI data measured at the Helmholtz Zentrum hereon were utilized.

$$\begin{aligned} f(x,y) = exp(a_1 + \frac{a_2}{T} + a_3 T + a_4 x^{0.5} + a_5 x + a_6 x^2 + a_7 x^3 + a_8 x^4) \\ + exp(a_9 + a_{10} x + a_{11} T + a_{12} T^2 + a_{13} T^3) \end{aligned} \tag{4.13}$$

$$\begin{aligned} f(x,y) = exp(a_1 + \frac{a_2}{T} + a_3 T + a_4 x^{0.5} + a_5 x + a_6 x^2 + a_7 x^3 + a_8 x^4) \\ + exp(a_9 + a_{10} x + a_{11} T + a_{14} \frac{x}{T}) \end{aligned} \tag{4.14}$$

Figures 4.17 and 4.18 illustrate that the fitted surface overall follows the isotherms closely, with minor deviations in the single phase regions, particularly for absorption, where the isotherms exhibit steep increases at high weight fractions. R^2 values of 0.99606 for absorption and 0.99444 for desorption indicate excellent fit quality, slightly superior to prior fits for Hydralloy C1 and $Ti_{1.1}CrMn$. These polynomials can thus be implemented in Aspen for further analysis, with the in Curvefitter determined coefficients presented in Table 4.11.

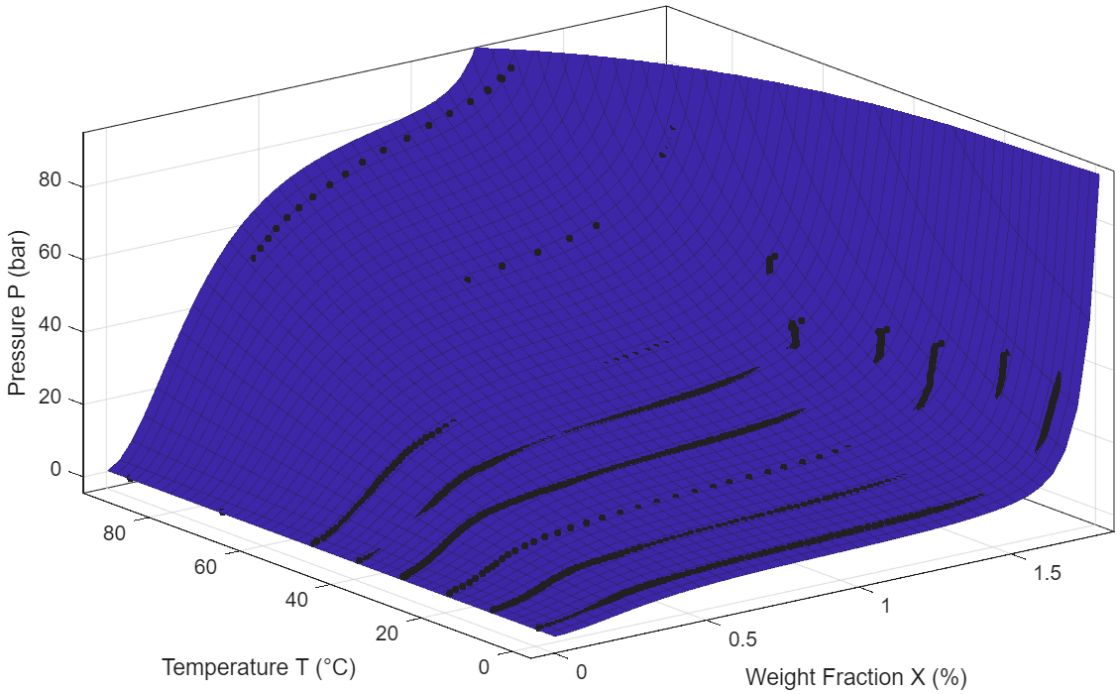

Figure 4.17: Polynomial fit: Absorption Hydralloy C5

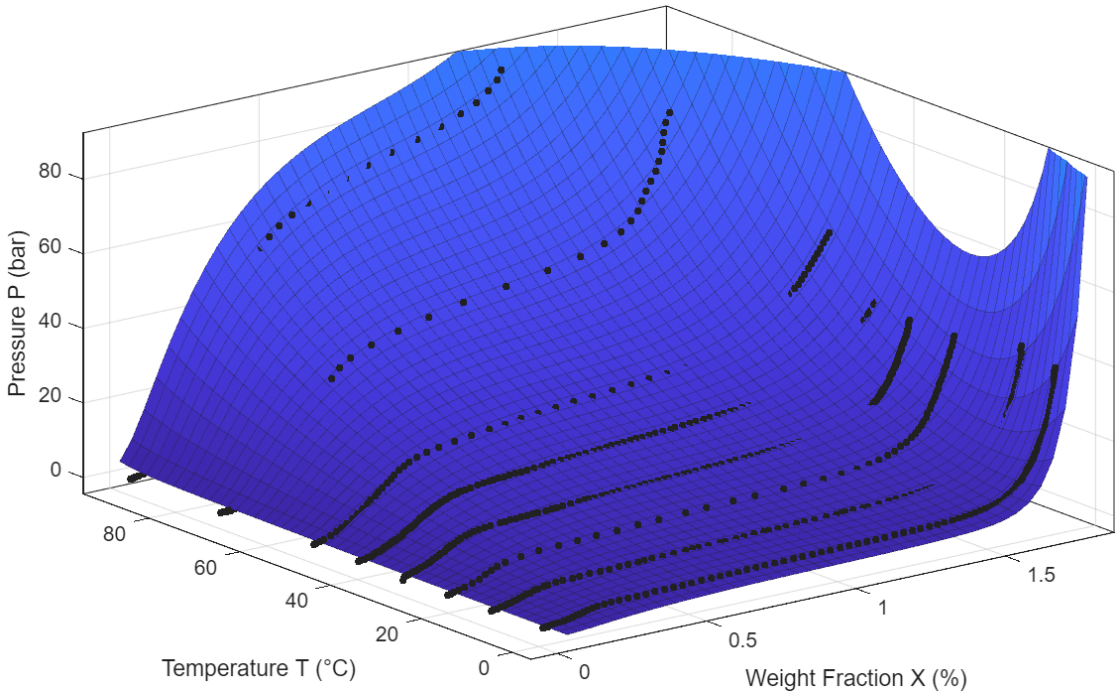

Figure 4.18: Polynomial fit: Desorption Hydralloy C5

Table 4.11: Polynomial Surface Fit (Custom Equation): Absorption and desorption Hydralloy C5

Coefficient	Absorption	Desorption
a_1	9.5763	19.7880
a_2	−3.4485	−3.5483
a_3	−0.0091	−0.0031
a_4	−24.5629	−3.2164
a_5	−25.0013	−2.3259
a_6	12.1440	1.4870
a_7	−5.4158	−0.9129
a_8	1.2330	0.3463
a_9	−356.5782	−89.1045
a_{10}	19.9707	−37.0041
p_{11}	3.4478	0.2427
p_{12}	−0.0122	0
p_{13}	1.4406	0
p_{14}	0	1.4234
R^2	0.996 06	0.994 44

4.5 Integration of the Selected Alloys and Model Development

To make the validated model suitable for the intended application, it is further developed by incorporating additional equations and parameters. This refinement includes the selected metal hydrides as well as the implementation of equations to calculate the required energy demand and productivity of the corresponding alloy. These parameters are essential for evaluating the overall performance of the designed compressor system. In particular, the energy demand quantifies the thermal energy required to compress the hydrogen (per cycle or mass unit MH or compressed hydrogen) and thus serves as a direct indicator of the thermodynamic efficiency of the compression process, while the productivity, expressed as the volume of hydrogen delivered per unit mass of metal hydride per unit time, characterizes the operational throughput of the system.

Together, these aspects allow for a comprehensive assessment of the system design under realistic operating conditions.

As described in Section 4.4, extending the model to include a second stage and integrating two distinct alloys may prove to be necessary to reach the desired pressure, while designing the compressor to be energy efficient and as productive as possible. A second stage installed downstream of valve V-2 enables a controlled gas transfer while preventing undesired pressure equalization between the stages.

Within the ACM framework, multiple alloys can be incorporated into a single model, such as Tank1D, through conditional if–else statements and drop-down list selections. To isolate and troubleshoot error messages that arise during alloy implementation in the model and subsequent design experiments, two separate models, Tank1D and Tank1DStage, were chosen that feature uniquely named variables. The extended two-stage model is illustrated in Figure 4.19.

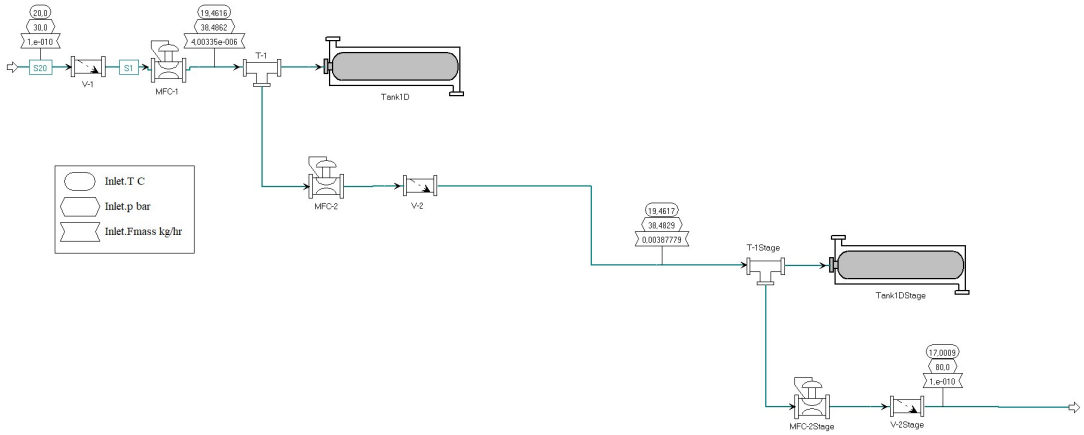

Figure 4.19: Two-stage flowsheet in Aspen Custom Modeler

Figure 4.20 shows the simulated dynamic behavior of the two compressor stages over a total duration of 1200 s, consisting of one absorption and one desorption cycle with a cycle duration of 600 s (10 min) each. During the first phase from 0 to 600 s, Stage 1 shows a positive hydrogen inflow through MFC-1 as it absorbs hydrogen, while Stage 2 exhibits a hydrogen outflow through MFC-3 as it desorbs hydrogen (Figure 4.20i). This alternating operation is reflected in the evolution of the relative hydrogen loading, $fract_{avg}$, which represents the average normalized hydrogen loading of the metal hydride bed relative to its maximum capacity wt_{max}.

In Stage 1, the average fraction increases gradually during absorption, whereas it decreases in Stage 2 as hydrogen is released.

The hydrogen mass flows are driven by the pressure difference between the tank gas pressure P_{gas} and the local equilibrium pressure P_{eq}. Absorption occurs when $P_{gas} > P_{eq,abs}$ ($\Delta p_{abs} > 0$), while desorption occurs when $P_{eq,des} > P_{gas}$ ($\Delta p_{des} > 0$). As a result, the tank pressure in Stage 1 decreases to the inlet pressure of approximately 30 bar during absorption, whereas the pressure in Stage 2 rises during desorption until the target outlet pressure of 80 bar is reached (Figure 4.20ii).

At the same time, the temperature of the heat transfer fluid is ramped down in Stage 1 to the target cooling temperature of 10 °C (Figure 4.20iii), thereby lowering P_{eq} and promoting hydrogen uptake. In Stage 2, the HTF temperature is ramped up to 60 °C, raising P_{eq} and supplying the heat required for the endothermic desorption reaction.

After 600 s, the thermal boundary conditions are switched. Stage 1 is heated and Stage 2 is cooled, which reverses the thermodynamic driving forces and initiates the next cycle. Hydrogen flows back out of Stage 1 and thereby supplying hydrogen to Stage 2, where the absorption process is starting, leading to a corresponding recovery of the hydrogen fraction..

A critical aspect for two-stage compressor operation is the correct pressure transfer between the stages. The desorption pressure of the first stage must match the absorption inlet pressure of the second stage to ensure continuous hydrogen transfer. As illustrated in Figure4.20iii), the first stage compresses hydrogen from the low pressure supply of approximately 30 bar to an intermediate during its desorption phase. This intermediate pressure serves as the absorption inlet pressure for the second stage, which subsequently compresses the hydrogen further to the final outlet pressure of 80 bar.The continuity of this pressure cascade is essential for the correct operation of the overall system, as any mismatch between the outlet pressure of the first stage and the absorption equilibrium pressure of the second stage would impede the transfer between the two stages.

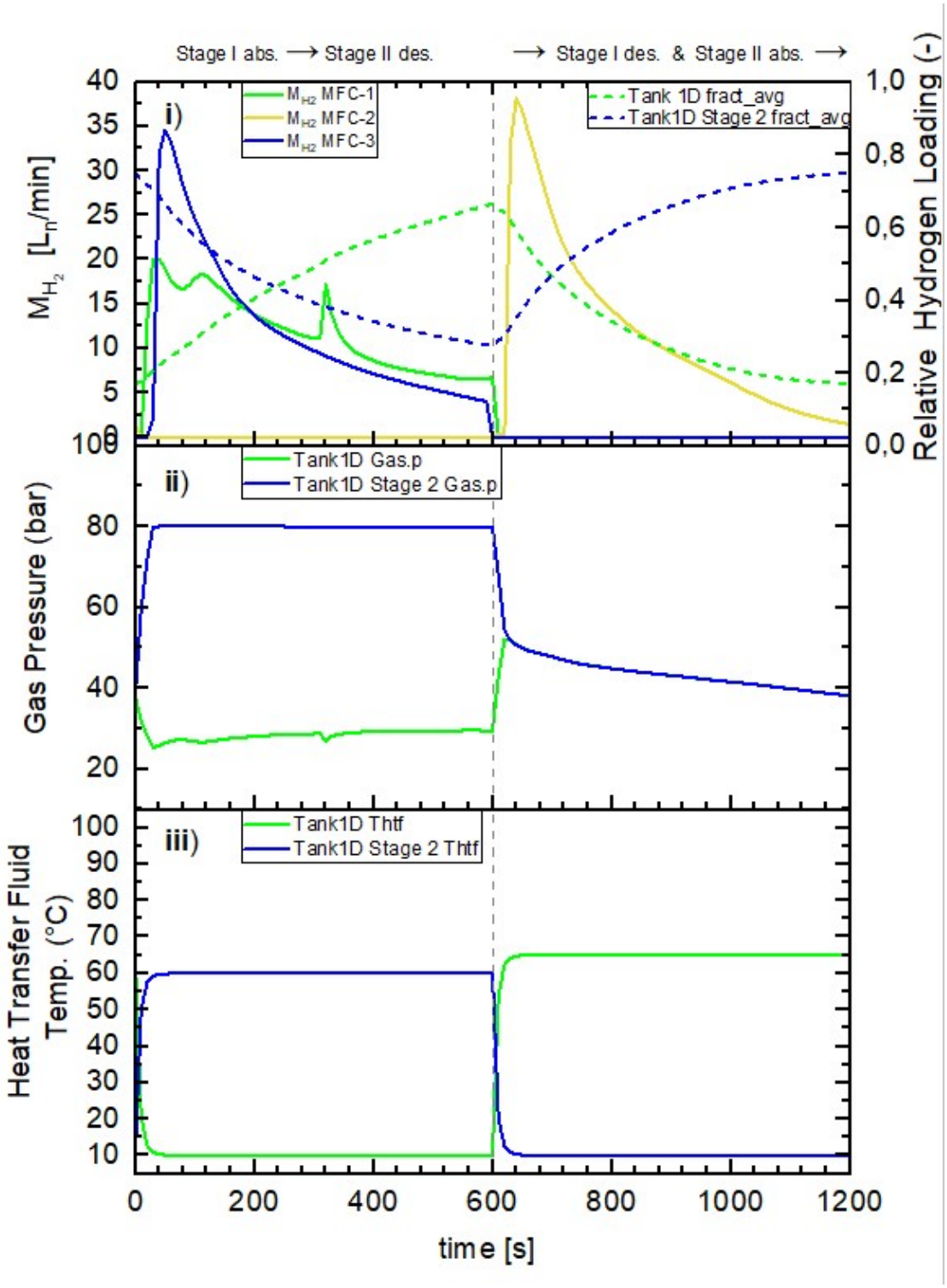

Figure 4.20: Compressor operation in subsequent absorption and desorption cycles

As shown in Table 4.3, several parameters are required to incorporate new alloys into the model. The thermodynamic and kinetic parameters, as well as the appropriate kinetic model for the selected alloys, can be found in Sections 4.3.2, 4.3.2 and 4.3.2. The polynomials and coefficients used for both alloys are provided in Section 4.4.

Productivity:
To quantify the hydrogen output of each compressor stage, the cumulative mass outflow is tracked by integrating the instantaneous outlet mass flow rate over time. In the ACM model, this is implemented as a differential equation for each stage:

$$\frac{d\,m_{out}}{dt} = \dot{m}_{out}(t) \tag{4.15}$$

where $\dot{m}_{out}$ is the instantaneous outlet mass flow rate after the stage and m_{out} is initialized to zero at the start of each simulation. The resulting integrated outflow $m_{out}(t)$ represents the total hydrogen mass delivered by the respective stage up to time t.

This quantity is subsequently normalized by the alloy mass M_{alloy} and the cycle duration to yield the specific productivity:

$$Specific\ \ Productivity = \frac{m_{out}}{m_{alloy} \cdot t_{Simulation}} \quad (Ln/kg_{MH}/h) \tag{4.16}$$

which provides a material-independent performance metric that allows direct comparison with literature values for different alloys and other parameter such as tank geometries.

Energy demand:
The thermal energy demand of the compressor tank is derived from the dynamic energy balance of the Heat Transfer Fluid (HTF) which serves as the thermal interface between the external heat supply and the tank wall.

$$M_{HTF} \cdot c_{p,HTF} \cdot \frac{dT_{HTF}}{dt} = \underbrace{\dot{m}_{HTF} \cdot c_{p,HTF} \cdot (T_{HTF,in} - T_{HTF})}_{\dot{Q}_{flow}} + \underbrace{h \cdot A_{tank} \cdot (T_{wall(end)} - T_{HTF})}_{\dot{Q}_{wall}} \tag{4.17}$$

The first term $\dot{Q}_{flow}$ is then used as the measure of the external thermal energy demand:

$$\dot{Q}(t) = \dot{m}_{HTF} \cdot c_{p,HTF} \cdot (T_{HTF,in} - T_{HTF}) \tag{4.18}$$

The sign of $\dot{Q}$ inherently distinguishes the two operating modes: a positive value indicates that the HTF supplies heat to the tank, corresponding to the endothermic desorption phase, while a negative value indicates heat removal from the tank during the exothermic absorption phase. These contributions are separated into:

$$\dot{Q}_{heating} = \begin{cases} \dot{Q} & \text{if } \dot{Q} > 0 \\ 0 & \text{otherwise} \end{cases} \qquad \dot{Q}_{cooling} = \begin{cases} -\dot{Q} & \text{if } \dot{Q} < 0 \\ 0 & \text{otherwise} \end{cases} \tag{4.19}$$

Both are integrated over time to yield the cumulative heating and cooling energy demands. From these, cycle-averaged thermal power demands and specific energy requirements can be derived by normalizing by the time or alloy mass.

Calculation wall thickness:
When varying the tank diameter during the design investigation, the required wall thickness t_{wall} must be recalculated accordingly to ensure structural integrity under the operating pressure. The calculation follows the standard formula for cylindrical pressure vessels under internal pressure (Kesselformel):

$$t_{wall,min} = \frac{p \cdot d_m}{2 \cdot \sigma_{allowable}} + s_1 + s_2 \tag{4.20}$$

where p is the internal pressure [MPa], d_m the mean diameter [mm], $\sigma_{allowable}$ the allowable stress of the tank material [N/mm^2], s_1 a corrosion allowance, and s_2 a tolerance allowance. Since the mean diameter $d_m = d_i + t$ itself depends on the unknown wall thickness t, Equation 4.20 cannot be evaluated directly. Substituting d_m and rearranging yields the following equation:

$$t_{wall,min} = \frac{p \cdot d_i}{2 \cdot \sigma_{zul} - p} + s_1 + s_2 \tag{4.21}$$

For the tank material 1.4404 (316L stainless steel), the allowable stress is determined from the yield strength of around 200 N/mm^2 [122] divided by a safety factor of 1.5.Since the wall thicknesses in the validated model are designed for 100 bar, this maximum internal pressure is used in the calculations for comparability purposes. Since the calculation includes a generous safety factor and this is a simulation, no additional safety factors for corrosion or tolerance allowance are added. Equation 4.21 is applied for each simulation with a diameter change, ensuring consistency and a reflection of reality.

5 Simulation and Results

5.1 Model Optimization and Design of a Metal Hydride Compressor

As previously discussed in section 4.3.2, the careful selection of one or more suitable metal hydrides is a fundamental step in the design of a metal hydride compressor and essential for achieving the target pressure levels, especially for this work, under the constraint of the narrow available temperature range in Moorburg. However, the overall performance and feasibility of such a system depends not only on the hydrides properties but also on a range of operational and geometric parameters that define the compressors behavior under realistic working conditions.

Therefore, this section focuses on the optimization and design with several remaining key design parameters. The parameters considered include the heating and cooling temperature, metal hydride mass, cycle time, as well as the geometric configuration of the compressor tank. Each of these parameters significantly affects the overall system performance, measured by the specific productivity, the required energy demand but also the system compactness, which cannot be neglected. The results of these experiments allow for the identification of an optimized but feasible design configuration, to provide a foundation for the scaling to a practical design for Moorburg.

5.1.1 Preliminary Single-stage Experiments

As a first step in the optimization process, initial simulation experiments were carried out with the temperature of the Heat Transfer Fluid as a starting parameter. The aim of these preliminary simulation experiments is to determine whether the desired pressures can be reached under the narrow temperature range available and to identify which alloy compositions offer the most promising performance (specific productivity). Furthermore, the simulations help evaluate which system configuration (single-stage or two-stage) provides optimal compression behavior for the given temperature constraints.

The results of these initial studies provide the basis for subsequent, more detailed parameter optimization of the metal hydride compressor model.

The preliminary experiments for all selected metal hydrides are based on the settings used to validate the model for Hydralloy C5. Therefore, the initial simulations were conducted at pressures between 30 and 60 bar and temperatures between 10 and 90°C. Additional parameters, such as cycle time, will be discussed in subsequent sections. The temperature and pressure ranges shown in the Tables 5.1 to 5.3 are intended to illustrate the trends in the behavior of the individual, selected metal hydrides.

As described in Section 4.4, the selected Hydralloy C1 can be applied over the entire investigated pressure range, however, due to the narrow, at Moorburg available temperature range, its use appears more suitable for a first-stage application. This is reflected in the initial simulations, which operate between 30 and 60 bar. The broad temperature range of 10 to 90°C ensures that these pressures can be achieved.

In the preliminary tests, the maximum operating temperature is then gradually reduced to identify the lowest feasible temperature range that maintains acceptable productivity, until either the productivity becomes economically nonviable or ACM indicates convergence errors. This approach allows progressive narrowing of the upper temperature limit for subsequent experiments. In the next step, the maximum temperature is reset to 90°C while the minimum temperature is increased, followed by simultaneous variation of both boundary temperatures. The same procedure is repeated for the entire pressure range of 30 to 80 bar, as well as for additional pressure intervals that may represent viable first-stage conditions.

As outlined in Section 4.4, Hydralloy C5 can also operate across the full pressure range, though its pressure–temperature characteristics suggest a potential advantage as a first-stage material. Consequently, the preliminary experiments performed for Hydralloy C1 are repeated for Hydralloy C5. For the alloy $Ti_{1.1}CrMn$, Section 4.4 similarly indicates its applicability as a single stage alloy over the full pressure range, with a more favorable profile as a possible second stage. The preliminary simulations for $Ti_{1.1}CrMn$ are conducted at considerably lower temperature ranges compared to both Hydralloys, reflecting the distinct pressure–temperature characteristics of this alloy.

5.1.2 Preliminary Single-stage Experiments results

Table 5.1 presents the experimental plan of Hydralloy C1 for the single-stage preliminary experiments and productivity results across varying pressure and temperature ranges.

The initial simulation with the widest temperature range (Exp. 1) at 30 to 60 bar and 10 to 90°C yields a productivity of 146.38 $Ln/kg_{MH}/h$. Progressively narrowing the upper temperature limit reduces productivity accordingly, dropping to 125.80 $Ln/kg_{MH}/h$ at 70°C (Exp. 2) and further to 75.94 $Ln/kg_{MH}/h$ at 60°C (Exp. 3), corresponding to reductions of 20.58 and 49.86 $Ln/kg_{MH}/h$, respectively. Raising the lower temperature boundary has a more pronounced effect. Increasing it to 20 °C (Exp. 5) causes a sharp drop to 55.31 $Ln/kg_{MH}/h$, with increase to 30°C (Exp. 4) the specific productivity drops further to 9.5 $Ln/kg_{MH}/h$, while a combined adjustment to 20 to 80°C (Exp. 6) results in 49.17 $Ln/kg_{MH}/h$.

Across the 30 to 80 bar pressure range, productivity decreases with narrowing temperature intervals, dropping from 119.66 to 57.95 $Ln/kg_{MH}/h$ as the upper temperature limit is reduced from 90 to 70°C. At narrower pressure spans of 30 to 50 bar and 30 to 45 bar, productivity remains elevated even as the temperature interval is reduced, still achieving 92.23 $Ln/kg_{MH}/h$ at 30 to 45 bar with a temperature range as narrow as 15 to 55°C (Exp. 12).

Table 5.1: Experimental plan Hydralloy C1 (preliminary single-stage experiments)

Exp. No.	Pressure (bar)	Temperature (°C)	Productivity (Ln/kg MH/h)
1	30–60	10–90	146.38
2	30–60	10–70	125.80
3	30–60	10–60	75.94
4	30–60	30–90	9.5
5	30–60	20–90	55.31
6	30–60	20–80	49.17
7	30–80	10–90	119.66
8	30–80	10–70	57.95
9	30–50	10–70	149.48
10	30–50	15–65	97.65
11	30–45	15–60	102.3
12	30–45	15–55	92.23

Table 5.2 presents the experimental plan of Hydralloy C5 for the single-stage preliminary experiments and productivity results across varying pressure and temperature ranges.

The initial simulation at 30 to 60 bar and 10 to 90°C (Exp. 1) yields a productivity of 144.35 $Ln/kg_{MH}/h$. Reducing the upper temperature limit leads to a steep decline, falling to 67.87 $Ln/kg_{MH}/h$ at 80°C (Exp. 2) and to 19.87 $Ln/kg_{MH}/h$ at 70°C (Exp. 3). In contrast to Hydralloy C1, raising the lower temperature boundary to 30°C (Exp. 4) increases productivity to 107.13 $Ln/kg_{MH}/h$, while 20°C leads to 129.98 $Ln/kg_{MH}/h$. A combined adjustment to 20 to 80°C (Exp. 6) results in 52.82 $Ln/kg_{MH}/h$. Extending the pressure range to 30 to 80 bar (Exp. 7) yields a comparatively low productivity of 56.47 $Ln/kg_{MH}/h$. Consistent with the findings for Hydralloy C1, a narrower pressure span of 30 to 50 bar produces the highest recorded values, reaching 149.48 $Ln/kg_{MH}/h$ at 10 to 90°C (Exp. 8) and remaining above 80 $Ln/kg_{MH}/h$ even as the temperature interval is progressively narrowed (Exp. 9–10).

Table 5.2: Experimental plan Hydralloy C5 (preliminary single-stage experiments)

Exp. No.	Pressure (bar)	Temperature (°C)	Productivity (Ln/kg MH/h)
1	30–60	10–90	144.35
2	30–60	10–80	67.87
3	30–60	10–70	19.87
4	30–60	30–90	107.13
5	30–60	20–90	129.98
6	30–60	20–80	52.82
7	30–80	10–90	56.47
8	30–50	10–90	149.48
9	30–50	10–80	120.42
10	30–50	10–75	82.2
11	30–50	5–75	88.07

Table 5.3 presents the experimental plan of $Ti_{1.1}CrMn$ for the single-stage preliminary experiments and productivity results across varying pressure and temperature ranges.

At 50 to 80 bar and 10 to 50°C (Exp. 1), a productivity of 124.44 $Ln/kg_{MH}/h$ is achieved, which decreases to 106.08 $Ln/kg_{MH}/h$ upon raising the lower temperature boundary to 15°C (Exp. 2). Extending the pressure range to 30 to 80 bar (Exp. 3) results in a sharp drop to 25.96 $Ln/kg_{MH}/h$ at 5 at 50°C, while Exp. 4 at 2 to 68°C yields 109.96 $Ln/kg_{MH}/h$, though accompanied by simulation errors. A reduced pressure span of 45–80 bar (Exp. 5) at 10 to 50°C produces a productivity of 100.98 $Ln/kg_{MH}/h$.

Table 5.3: Experimental plan $Ti_{1.1}CrMn$

Exp. No.	Pressure (bar)	Temperature (°C)	Productivity (Ln/kg MH/h)
1	50–80	10–50	124.44
2	50–80	15–50	106.08
3	30–80	5–50	25.96
4	30–80	2–68	109.96
5	45–80	10–50	100.98

5.1.3 Discussion of Preliminary Single-stage Experiments

The results indicate that both Hydralloy C1 and Hydralloy C5 are in principle applicable across the full investigated pressure range. However, their sensitivities to temperature adjustments differ notably. Hydralloy C5 exhibits a strong dependence on the upper temperature limit, with productivity declining sharply as the maximum temperature is reduced with a drop of 76.48 $Ln/kg_{MH}/h$ between 90 and 80°C at 30 to 60 bar alone. Hydralloy C1, by contrast, shows productivities above 90 $Ln/kg_{MH}/h$ even at narrow temperature ranges such as 15 to 55 °C at pressure ranges 30 to 45 bar. Hydralloy C1 is therefore preferable over Hydralloy C5 from an operational standpoint. Hydralloy C5 is excluded from further consideration.

The results for $Ti_{1.1}CrMn$ confirm its suitability as a complementary alloy operating at a significantly different pressure–temperature range, with the highest productivities achieved at pressure spans of 50 to 80 bar and moderate temperatures above 10°C and below 50°C. There is a considerable drop in productivity observed when extending the lower pressure boundary to 30 bar (Exp. 3, 4).

To maintain productivity around 100 $Ln/kg_{MH}/h$, low temperatures down to around 0 °C and high temperatures up to around 70 °C must be selected, in opposition to the goal of keeping the temperature range as minimal as possible, or the lower limit of the pressure range must be set again higher than 30 bar. This further supports a narrower pressure span for this alloy and excludes the alloy as a single stage material.

Given the distinct and complementary operating windows of Hydralloy C1 and $Ti_{1.1}CrMn$, a two-stage configuration, with Hydralloy C1 as the first stage and $Ti_{1.1}CrMn$ as the second, is identified as the most promising approach for further investigation. The varying pressure ranges tested across experiments reflect the uncertainty regarding the exact pressure transfer point between the two stages (pressure after the first stage not a fixed value in ACM), which will be determined in subsequent simulations.

5.1.4 Subsequent Two-stage Experiments

Building on the preliminary single-stage experiments, which established approximate suitable temperature ranges and confirmed the material selection of Hydralloy C1 and $Ti_{1.1}CrMn$ in a two-stage system. The simulations investigate the influence of HTF temperature, metal hydride mass, cycle time, and tank dimensioning on system performance. For each parameter, the objective is to identify an optimum with respect to both productivity, evaluated for each individual stage as well as the combined system ($Ln/kg_{MH,total}/h$) and energy demand, while additionally investigating boundary conditions of the stated parameters.

Further temperature investigations are necessary in the two-stage configuration due to the variable intermediate pressure between the stages and the interdependence of both stages, which alters the effective plateau region utilized in each alloy's PCI curve as the operating temperature of the second stage changes. Based on the preliminary results, an operational temperature range of 10 to 60°C is assumed feasible for both stages. Simulations begin at 15 to 50°C, as a lower temperature of 20°C already yielded significantly reduced productivity for both individual alloys. The lower temperature is first reduced stepwise for both stages simultaneously, followed by a stepwise increase of the upper temperature. The two stages are treated independently in the latter step, as $Ti_{1.1}CrMn$ in the second stage reaches the required outlet pressure of 80 bar at moderate temperatures, rendering excessively high temperatures unnecessary. Additionally, the direction of temperature adjustment, whether raising the upper or lowering the lower boundary, is examined with respect to its potential for maximizing productivity.

The investigation of metal hydride mass distribution is conducted based on the optimal temperature conditions identified in the preceding experiment. The validated model used a reference system contains 1.311 kg of metal hydride per tank. Since productivity is normalized to metal hydride mass, a uniform scaling of both tanks leaves the specific productivity unchanged, as hydrogen throughput scales proportionally with total mass. Consequently, the relevant parameter is the mass ratio between the two stages at constant total mass. A suboptimal ratio results in a capacity imbalance between the stages: exemplary, if the first stage contains insufficient metal hydride, less hydrogen is transferred per cycle than the second stage could absorb, reducing overall productivity. The mass ratio is therefore varied iteratively until optimal productivity is achieved or simulation convergence errors occur.

The reference cycle time is 10 minutes per half-cycle, corresponding to 10 minutes of cooling and 10 minutes of heating per full cycle. An optimal cycle time must be sufficiently long to allow complete absorption and desorption, thereby fully utilizing the storage capacity of each alloy, while remaining short enough to maximize the number of cycles per unit time. Both boundaries are examined by stepwise increasing and decreasing the cycle time for both stages.

A further critical design parameter is the tank dimensioning, specifically the ratio between bed diameter and bed length. As described in 4.5, adjusting the tank diameter requires a corresponding recalculation of the wall thickness and adjusting the distance between the outer wall of the tank and the wall of the heat exchanger accordingly (variable $d_{HE,in}$). In the one-dimensional radial model employed, the bed radius is the governing geometric parameter: a larger radius with a correspondingly shorter tank length reduces the heat transfer surface area per unit mass and increases the metal hydride mass per radial node, thereby reducing heat transfer efficiency and therefore the energy demand. A larger bed radius is also expected to negatively affect productivity at a given cycle time.

5.1.5 Subsequent Two-Stage Experiments Results and Discussion

The results of the two-stage temperature investigation are presented in Table 5.4, listing the applied temperature ranges alongside the corresponding stage-wise and total specific productivity as well as energy demand for each experiment.

The two-stage temperature investigation begins at 15 to 50°C for both stages (Exp. 1) yielding a total productivity of 37.66 $Ln/kg_{MH}/h$. Reducing the lower temperature to 10°C (Exp. 2) increases total productivity by 44.7% to 54.52 $Ln/kg_{MH}/h$, consistent with the expectation that a lower cooling temperature allows greater utilization of the alloy plateaus of both alloys. A further reduction to 5°C (Exp. 3) yields only a modest additional gain of 16.6% to 63.58 $Ln/kg_{MH}/h$, given the disproportionate increase in active cooling effort this would require in a real system, 10°C is retained as the lower temperature boundary for the following experiments.

Progressively raising the upper temperature limit from 50 to 55 °C and 60°C at a fixed lower boundary of 10°C (Exp. 2) increases total productivity consistently, reaching 76.92 $Ln/kg_{MH}/h$, as the wider temperature range allows more complete utilization of the alloy plateaus. Differentiating the temperature ranges between the two stages (Stage 1 at 10 to 65°C and Stage 2 at 10 to 60°C (Exp. 7)) yields 81.16 $Ln/kg_{MH}/h$, a 5.5% improvement of the total productivity over Exp. 5, reflecting the fact that the stages utilize two metal hydrides with different material properties. Equalization of both stages at 10 to 65°C (Exp. 8) produces only a marginal additional gain of 2.3% to 82.99 $Ln/kg_{MH}/h$, making a further heating of the second stage unnecessary.

Continuing to raise the upper temperature of Stage 1 beyond 65°C reveals that productivity gains become increasingly small and are outweighed by the associated rise in energy demand. While Exp. 10 (Stage 1 at 10 to 80°C) achieves the highest total productivity in this series at 87.69 $Ln/kg_{MH}/h$, the energy demand already reaches 0.4747 kW, and further increases to 90°C (Exp. 11) and 100°C (Exp. 12) not only fail to improve productivity, dropping to 83.76 and 81.76 $Ln/kg_{MH}/h$ respectively, but drive energy demand to 0.5426 and 0.6104 kW. This reversal suggests that at temperatures above 80°C, the shift in the intermediate pressure between the stages negatively affects the capacity utilization of Stage 2, offsetting any productivity gains in Stage 1. Experiment 13 confirms that a substantial total productivity increase to 102.35 $Ln/kg_{MH}/h$ is only achievable by simultaneously lowering the cooling temperature to 5°C, again broadening the temperature range.

Given the objective of identifying a moderate, practically feasible operating window, the conditions of Experiment 7 (Stage 1 at 10 to 65°C and Stage 2 at 10 to 60°C) represent the best compromise between productivity, energy demand, and temperature interval width, and are adopted as the basis for the subsequent metal hydride mass investigation.

Table 5.4: Experimental plan “temperature” two-stage system

Exp. No.	Temp. (°C)	Productivity (LN/kg MH/h)	Energy demand (kW)	Productivity tot. (LN/kg MH/h)
1 (Stage 1)	15–50	71.92	0.2374	–
1 (Stage 2)	15–50	75.32	0.2374	37.66
2 (Stage 1)	10–50	107.92	0.2713	–
2 (Stage 2)	10–50	109.04	0.2713	54.52
3 (Stage 1)	5–50	127.19	0.3052	–
3 (Stage 2)	5–50	127.16	0.3052	63.58
4 (Stage 1)	10–55	133.24	0.3052	–
4 (Stage 2)	10–55	130.43	0.3052	65.21
5 (Stage 1)	10–60	152.35	0.3391	–
5 (Stage 2)	10–60	153.83	0.3391	76.92
6 (Stage 1)	10–65	150.58	0.3730	–
6 (Stage 2)	10–55	145.02	0.3052	72.51
7 (Stage 1)	10–65	159.2	0.3730	–
7 (Stage 2)	10–60	163.82	0.3391	81.16
8 (Stage 1)	10–65	162.55	0.3730	–
8 (Stage 2)	10–65	165.99	0.3730	82.99
9 (Stage 1)	10–70	164.01	0.4069	–
9 (Stage 2)	10–60	164.61	0.3391	82.3
10 (Stage 1)	10–80	168	0.4747	–
10 (Stage 2)	10–60	175.38	0.3391	87.69
11 (Stage 1)	10–90	166.24	0.5426	–
11 (Stage 2)	10–60	167.53	0.3391	83.76
12 (Stage 1)	10–100	168.04	0.6104	–
12 (Stage 2)	10–60	163.52	0.3391	81.76
13 (Stage 1)	5–90	207.78	0.5765	–
13 (Stage 2)	5–60	204.69	0.3730	102.35

The results of the metal hydride mass investigation are presented in Table 5.5, listing the applied mass ratios and absolute masses alongside the corresponding stage-wise and total productivity for each experiment.

Prior to investigating the effect of mass ratio, the linearity of specific productivity with respect to absolute mass scaling was verified by uniformly increasing and decreasing the metal hydride mass of both stages simultaneously, with the bed length adjusted accordingly. Across the investigated range of 0.811 to 1.811 kg per stage (Exp. 1 to 6), total productivity varies between 78.14 and 80.24 $Ln/kg_{MH}/h$. A slight downward trend is observed with increasing mass, the origin of which is not fully resolved and may reflect numerical effects within the ACM simulation rather than a true physical dependence. The linearity assumption is therefore considered valid for the purposes of this investigation.

The effect of mass ratio between Stage 1 and Stage 2 was subsequently investigated at a constant total mass of 2.622 kg. Increasing the proportion of Stage 1 beyond the 50:50 distribution (Exp. 7 to 10) results in a progressive decline in total productivity, falling from 80.29 $Ln/kg_{MH}/h$ at 55:45 to 70.47 $Ln/kg_{MH}/h$ at 70:30. This is consistent with a growing capacity imbalance: as Stage 1 mass increases, Stage 2 receives more hydrogen per cycle than it can absorb, limiting overall throughput. The opposite trend is observed when increasing the proportion of Stage 2 (Exp. 11 to 13), where total productivity drops even more sharply, reaching 58.07 $Ln/kg_{MH}/h$ at a 30:70 ratio, as Stage 1 can no longer supply sufficient hydrogen to fully utilize Stage 2 capacity. In both directions, deviations beyond the investigated range cause convergence errors in Aspen, indicating operationally unstable configurations.

Since no mass ratio yields a higher total productivity than the 50:50 distribution of the temperature reference experiment, the equal mass distribution at 1.311 kg per stage is retained for the subsequent investigations.

Table 5.5: Experimental plan “MH-Mass” two-stage system

Exp. No.	MH ratio	MH mass (kg)	Productivity (LN/kg/h)	Productivity tot. (LN/kg MH/h)
1 (Stage 1)	50:50	1.411	158.97	–
1 (Stage 2)	–	1.411	160.36	80.18
2 (Stage 1)	50:50	1.511	158.61	–
2 (Stage 2)	–	1.511	159.12	79.56
3 (Stage 1)	50:50	1.811	155.73	–
3 (Stage 2)	–	1.811	156.28	78.14
4 (Stage 1)	50:50	1.211	159.76	–
4 (Stage 2)	–	1.211	159.82	79.91
5 (Stage 1)	50:50	1.111	160.06	–
5 (Stage 2)	–	1.111	160.19	80.09
6 (Stage 1)	50:50	0.811	160.38	–
6 (Stage 2)	–	0.811	160.49	80.24
7 (Stage 1)	55:45	1.442	148.72	–
7 (Stage 2)	–	1.18	178.41	80.29
8 (Stage 1)	60:40	1.573	135.83	–
8 (Stage 2)	–	1.049	199.33	79.75
9 (Stage 1)	65:35	1.704	120.17	–
9 (Stage 2)	–	0.918	219.96	77.01
10 (Stage 1)	70:30	1.835	101.29	–
10 (Stage 2)	–	0.787	234.77	70.47
11 (Stage 1)	45:55	1.18	165.29	–
11 (Stage 2)	–	1.442	136.52	75.08
12 (Stage 1)	40:60	1.049	171.56	–
12 (Stage 2)	–	1.573	123.6	74.15
13 (Stage 1)	30:70	0.787	184.21	–
13 (Stage 2)	–	1.835	82.98	58.07

The results of the cycle time investigation are presented in Table 5.6, listing the applied cycle times alongside the corresponding stage-wise and total productivity as well as energy demand for each experiment.

Increasing the cycle time (referring to one cooling/heating cycle, often called half-cycle). from 10 to 15 and 20 minutes (Exp. 1 to 2) results in a significant drop in total productivity of 14.4% and 23.9% to 69.51 $Ln/kg_{MH}/h$ and 61.74 $Ln/kg_{MH}/h$, respectively, as fewer cycles are completed per unit time. However, this is accompanied by a proportional reduction in energy demand, indicating that longer cycle times may be preferable in energy-constrained applications at the cost of throughput. Reducing the cycle time to 5 minutes (Exp. 3) increases total productivity by 3.6% to 84.12 $Ln/kg_{MH}/h$, while energy demand doubles to 1.4242 kW (0.7460 kW at stage 1 and 0.6782 kW at stage 2) for a cycle, which is a 100% increase relative to the reference Exp. 7 of the temperature investigation. This is suggesting that the marginal productivity gain is disproportionately costly in terms of energy.

A further reduction to 2.5 minutes (Exp. 4) does not continue this trend. Instead, total productivity drops sharply 63.52 $Ln/kg_{MH}/h$, with the energy demand also significantly lower than for the 5 min cycle. This suggests that at cycle times below 5 minutes, the duration is insufficient for complete absorption and desorption, such that the available storage capacity of both alloys can no longer be fully utilized within each cycle. The energy demand again increases significantly. Cycle times shorter than 2.5 minutes result in frequent convergence errors in Aspen. Given the marginal productivity gain at 5 minutes relative to the substantially higher energy demand, the reference cycle time of 10 minutes is retained for subsequent experiments as the best compromise between productivity and energy efficiency.

It should be noted that the present investigation applies equal cycle times to both the absorption and desorption cycles, as well as to both stages. In principle, asymmetric cycle times (applying different durations to absorption and desorption or to each stage independently), could offer additional optimization potential, as the kinetics for both reactions are not symmetric. However, this approach was not pursued in the present study, as its practical implementation would require either buffer tanks between the stages or multiple parallel hydride beds per stage operating in a time-offset manner to achieve a quasi-continuous hydrogen flow. Both solutions considerably increase system complexity and are therefore considered beyond the scope of this work.

Table 5.6: Experimental plan “cycle time” two-stage system

Exp. No.	Cycle time (min)	Productivity (LN/kg/h)	Energy demand (kW)	Productivity tot. (LN/kg MH/h)
1 (Stage 1)	20	124.19	0.1865	–
1 (Stage 2)	20	123.47	0.1696	61.74
2 (Stage 1)	15	139.42	0.2487	–
2 (Stage 2)	15	139.02	0.2261	69.51
3 (Stage 1)	5	165.38	0.7460	–
3 (Stage 2)	5	168.24	0.6782	84.12
4 (Stage 1)	2.5	129.21	1.4921	–
4 (Stage 2)	2.5	127.3	1.3564	63.52

The results of the tank dimensioning investigation are presented in Table 5.7, listing the applied dimensions alongside the corresponding stage-wise and total productivity as well as energy demand for each experiment.

Reducing the bed diameter progressively from 0.046 m to 0.040 m, 0.036 m, and 0.030 m (Exp. 1 to 3), with corresponding increases in bed length to maintain constant mass, yields substantial productivity gains, reaching a maximum of 132.21 $Ln/kg_{MH}/h$ at 0.030 m bed diameter. Simultaneously, the combined energy demand decreases as the smaller radius enable more efficient heat transfer within the one-dimensional radial model. This confirms that a narrower bed diameter improves both productivity and energy efficiency by allowing faster and more complete absorption and desorption cycles.

Experiments 4 and 5 investigate asymmetric configurations, applying different diameters to each stage. Their total productivities of 113.88 and 124.26 $Ln/kg_{MH}/h$ fall between the symmetric configurations of comparable diameter, consistent with the expectation that the stage with the larger diameter limits overall performance. This further confirms that a larger bed radius has a detrimental effect on productivity regardless of which stage it is applied to.

Increasing the bed diameter beyond the reference to 0.052, 0.056, and 0.062 m (Exp. 6 to 8) produces the opposite effect, with total productivity declining and reaching a minimum of 57.24 $Ln/kg_{MH}/h$, while energy demand rises. This is consistent with the expected deterioration in heat transfer efficiency at a larger radius.

The smallest investigated diameter of 0.030 m yields the highest productivity and is therefore selected as the preferred design. The corresponding bed length of 0.705 m may appear too elongated for filling and packing material, but the length can readily be distributed across multiple shorter tank segments. Furthermore, Davids et al. present a metal hydride compressor with tank lengths of 2.5 m [123], placing a bed length of 0.705 m well within a realistic range. The inner diameter of 0.030 m also may introduce practical challenges during filling and packing of the metal hydride material, however, Davids et al. demonstrate a metal hydride compressor with an inner diameter of 26.92 mm [123], confirming that 0.030 m lies within the realistic range. A detailed quantitative assessment of these exemplary challenges is beyond the scope of this work, the configuration of Exp. 3 is therefore carried forward for further analysis.

Table 5.7: Experimental plan “tank dimensions” two-stage system

Exp. No.	d_bed (m)	l_bed (m)	Productivity (LN/kg/h)	Energy demand (kW)	Productivity tot. (LN/kg MH/h)
1 (Stage 1)	0.04	0.34	198.98	0.3386	–
1 (Stage 2)	0.04	0.397	199.24	0.3079	99.62
2 (Stage 1)	0.036	0.49	222.16	0.3196	–
2 (Stage 2)	0.036	0.49	222.5	0.2904	111.25
3 (Stage 1)	0.03	0.705	264.34	0.2905	–
3 (Stage 2)	0.03	0.705	264.42	0.2640	132.21
4 (Stage 1)	0.036	0.49	227.65	0.3195	–
4 (Stage 2)	0.03	0.705	227.77	0.2640	113.88
5 (Stage 1)	0.03	0.705	255.37	0.2904	–
5 (Stage 2)	0.036	0.49	248.52	0.2905	124.26
6 (Stage 1)	0.052	0.235	144.74	0.3967	–
6 (Stage 2)	0.052	0.235	145.05	0.3606	72.53
7 (Stage 1)	0.056	0.202	131.14	0.4159	–
7 (Stage 2)	0.056	0.202	132.02	0.3781	66.01
8 (Stage 1)	0.062	0.165	113.72	0.4444	–
8 (Stage 2)	0.062	0.165	114.48	0.4040	57.24

These subsequent investigations identify the following optimal configuration for the two-stage metal hydride compressor: Stage 1 (Hydralloy C1) operating at 10 to 65°C and Stage 2 ($Ti_{1.1}CrMn$) at 10 to 60°C, with an equal mass distribution of 1.311 kg per stage, a cycle time of 10 minutes per (half-)cycle, and a bed diameter of 0.03 m. Under these conditions, a total productivity of 132.21 $Ln/kg_{MH}/h$ is achieved at an energy demand of 0.2905 kW for stage 1 and 0.2640 kW for stage 2 (heating or cooling energy demand, respectively)). Further improvements in productivity and energy efficiency are possible through reduction of the bed diameter, though practical geometric constraints must be considered in a real system implementation, as the bed diameter is already quite narrow.

5.2 Scale-Up to Industrial Application

Following the parameter investigation and optimization of the two-stage metal hydride compressor in 5.1.5, the resulting configuration is scaled up to the operating conditions at the Moorburg site. This step translates the simulation results into physical dimensions and assesses whether the thermal energy available at Moorburg is sufficient to drive the compressor at the required throughput.

5.2.1 Required Metal Hydride Mass

The hydrogen mass flow entering the compressor at Moorburg amounts to 1998 kg/h, which corresponds to a volumetric flow of 22,449,439 Ln/h. The total metal hydride mass required to achieve this throughput follows directly from the total specific productivity of the optimized compressor 132.21 $Ln/kg_{MH}/h$.

$$m_{MH,scaled} = \frac{\dot{V}_{target}(Ln/h)}{Productivity_{total}(Ln/kg_{MH}/h)} \tag{5.1}$$

This yields a total metal hydride mass of $m_{MH,total}$ = 169801.36 kg. Since the mass ratio between Stage 1 and Stage 2 is 50:50 as determined in 5.1.5, each stage contains a metal hydride mass of $m_{MH,scaled,i}$ = 84900.68 kg.

5.2.2 Bed Geometry

Since the density of the metal hydride evolves during the simulation due to hydrogen absorption and desorption, the bed volume of the scaled system is determined via a linear scaling factor rather than a fixed density value. The scaling factor f is defined as the ratio between the target and simulated metal hydride mass per stage, and the scaled bed volume per stage follows accordingly:

$$f = \frac{m_{MH,scaled,i}}{m_{MH,i}}, \quad V_{bed,scaled,i} = V_{bed,i} * f \tag{5.2}$$

Based on the simulated bed volume of $V_{bed,i}$ = 4.9832 $\cdot 10^{-4}$ m^3 and a corresponding metal hydride mass of $m_{MH,i}$ = 1.311 kg, the scaled bed volume per stage amounts to $V_{bed,scaled,i}$ = 32.27 m^3.

To determine the bed diameter and the bed length, the length-to-diameter ratio (L/D) of the optimized simulation geometry is preserved. The simulated bed dimensions of $d_{bed,i}$= 0.03 m and $l_{bed,i}$ = 0.705 m yield an L/D ratio of 23.5. Applying this ratio to the cylindrical bed volume gives:

$$\begin{aligned} V_{bed,scaled,i} &= L \cdot \frac{\pi}{4} \cdot d_{bed,scaled,i}^2 \\ &= \frac{L}{D} \cdot \frac{\pi}{4} \cdot d_{bed,scaled,i}^3 \\ &= 23.5 \cdot \frac{\pi}{4} \cdot D^3 \end{aligned}$$

$$\Rightarrow \quad d_{bed,scaled,i} = \left(\frac{4 \cdot V_{bed,scaled,i}}{23.5 \cdot \pi} \right)^{1/3} \tag{5.3}$$

Inserting $V_{bed,scaled,i}$ = 32.27 m^3 yields a bed diameter of $d_{bed,scaled,i}$ = 1.20 m and a corresponding bed length of $l_{bed,scaled,i}$ = 28.3 m. It should be noted that these dimensions represent the hydride bed only, the actual vessel dimensions, including wall thickness and heat exchanger would increase the outer diameter and length accordingly.

From a practical standpoint, a single bed of these dimensions (1.20 diameter, 28.3 length, one compressor per stage) could pose significant challenges for thermal management. Therefore, a real implementation is expected to employ multiple parallel beds of smaller dimensions per stage.

5.2.3 Thermal Energy Assessment

Beyond the geometric dimensions, the feasibility of integrating the compressor at the Moorburg site depends on whether sufficient waste heat, such as from the electrolyzer, is available to drive the desorption cycle. Since the two stages operate in a time-offset manner, where Stage 1 is heated while Stage 2 cools and vise versa, only one stage requires heating at any given time. The maximum instantaneous heating demand is therefore determined by the stage with the higher specific heating power.

The average heating powers obtained from the simulation amount to $\dot{Q}_{avg,Stage1}$ = 0.2905 kW for Stage 1 and $\dot{Q}_{avg,Stage2}$ = 0.2604 kW for Stage 2, where $\dot{Q}_{\text{avg}}$ is defined as the integrated heating energy per heating time (half of the total simulation time).

Normalizing by the simulated metal hydride mass and scaling to the target mass yields:

$$\dot{Q}scaled, i = \frac{\dot{Q}_{avg,i}}{m_{MH,i}} \cdot m_{MH,scaled,i} \tag{5.4}$$

This results in a scaled heating demand of $\dot{Q}_{scaled,Stage1}$ = 18.81 MW_{th} and $\dot{Q}scaled, Stage2$ = 17.09 MW_{th}, giving a maximum instantaneous heating requirement of 18.81 MW.

Waste Heat available in Moorburg:

The electrolyzer plant currently being build in Moorburg consists of six Elyzer P-300 arrays, each rated at 17.5 MW, resulting in a total installed plant power of P_{plant} = 105 MW [89]. As detailed in Section 3.2.1, precise operational data for the electrolyzer are subject to confidentiality agreements. The following therefore represents an estimate based on publicly available information. At the beginning of life (BOL), Siemens specifies a plant efficiency of η_{plant} = 75.5 % (HHV) at full load [88]. It must be noted that Siemens Energy does not explicitly define the system boundary for the term *plant*, such that auxiliary systems from which no heat can be recovered, such as rectifiers, may be included in both the rated power and the efficiency figure, introducing uncertainty into the derived waste heat estimates. If auxiliary systems are included, van de Roest et al. report that auxiliary power consumption typically amounts to approximately 5 % of the stack capacity [25], yielding an estimated stack power of P_{stack} = 100 MW. Furthermore, stack efficiencies are generally higher than system-level efficiencies, applying the empirical stack efficiency equation of van de Roest et al. at full load yields

a stack efficiency of $\eta_{\text{stack}} = 76.9\,\%$ (HHV) [25], compared to the published plant value of 75.5%.

The thermal power dissipated by the plant is given by:

$$\dot{Q} = P_{plant} \cdot \left(1 - \eta_{plant}\right) \tag{5.5}$$

Substituting the BOL values yields 25.7 MW_{th} or 23.1 MW_{th} in the case, that auxiliaries are included in the system boundaries.

Over the course of the stack lifetime of 80 000 equivalent operating hours (EOH), progressive degradation due to increasing membrane resistance requires a higher operating voltage to maintain constant hydrogen output, thereby increasing both electrical consumption and waste heat production [25]. Van de Roest et al. report a measured PEM degradation rate of 0.19 % per 1 000 operating hours [25], yielding an increase of energy consumption after 10 years of:

$$\Delta\eta = r_{\text{deg}} \cdot t_{\text{lifetime}} = (0.19\,\%/1\,000\,\text{h}) \cdot 80\ 000\,\text{h} = 15.2\,\% \tag{5.6}$$

The increase in energy consumption of 15.2% leads to a $P_{plant,BOL}$ of 121 MW or 115.2 MW, in the case where auxiliaries are included in the system boundaries. The chemical power output of the plant, defined as $\dot{H}_{2,\text{HHV}} = P_{\text{plant}} \cdot \eta_{\text{plant}}$, remains constant at 79.3 MW or 76.9 MW, since hydrogen production is remains unchanged. The EOL waste heat is therefore:

$$\dot{Q}_{\text{EOL}} = P_{\text{plant,EOL}} - \dot{H}_{2,\text{HHV}} \tag{5.7}$$

Substituting the EOL values yields 41.7 MW_{th} or 38.3 MW_{th} in the case, that auxiliaries are included in the system boundaries.

This concludes the Chapter of the model development results for a two-stage metal hydride hydrogen compressor, comprising Hydralloy C1 in the first stage and $Ti_{1.1}CrMn$ in the second stage. Both stages operate with equal metal hydride masses, a cycle duration of 10 minutes, a slender and elongated tank design, and HTF temperatures ranging from a minimum of 10 °C to a maximum of 65 °C, depending on the respective stage and cycle phase. The scale-up to a capacity that would be required in Moorburg, yields a compressor of 28.3 m bed-length and 1.20 m bed-diameter. Building upon these results, a feasibility assessment of the proposed system is discussed.

6 Feasibility in Moorburg and Integration Assessment

The following section summarizes the key results of the compressor optimization and scale-up of section 5.2, and assesses the technical feasibility of integrating the proposed system at the Moorburg site. Table 6.1 provides an overview of the optimized simulation parameters alongside the corresponding values for the industrially scaled compressor.

Table 6.1: Comparison of optimized simulation model parameters and scaled-up compressor dimensions for the Moorburg application

Parameter	**Model**	**Scaled (Moorburg)**
Compressor Performance		
Total specific productivity	132.21 $Ln/kg_{MH}/h$	132.21 $Ln/kg_{MH}/h$
H_2 mass inflow	0.03009 kg/h	1998 kg/h
Heating power power (averaged) stage 1	0.2905 kW	18.81 MW
Heating power power (averaged) stage 2	0.2640 kW	17.09 MW
Metal Hydride Mass and Cycle time		
Stage 1 (Hydralloy C1)	1.311 kg	84900.68 kg
Stage 2 ($Ti_{1.1}CrMn$)	1.311 kg	84900.68 kg
Total MH mass	2.622 kg	169801.36 kg
Cycle time (half-cycle)	10 min.	-
Bed Geometry (per stage)		
Bed diameter d_{bed}	0.03 m	1.20 m
Bed length l_{bed}	0.705 m	28.3 m
Bed volume V_{bed}	$4.98556e \cdot 10^{-4}$ m^3	32.27 m^3
Temperature Requirements		
Desorption temperature stage 1	65 °C	65 °C
Desorption temperature stage 2	60 °C	60 °C
Absorption temperature stage 1	10 °C	10 °C
Absorption temperature stage 2	10 °C	10 °C
Moorburg Boundary Conditions		
Waste heat electrolyzer (best case) (BOL / EOL)	—	25.7 MW / 41.7 MW
Waste heat electrolyzer (worst case) (BOL / EOL)	—	23.1 MW / 38.3 MW
Max. waste heat temperature	—	46 °C

In Section 1.2, several key research questions were formulated to systematically evaluate the suitability of a MHC for potential integration at the Hamburg Green Hydrogen Hub (HGHH). The following section addresses these questions based on the comprehensive results from the conducted simulations and the subsequent scale-up analysis for the development of an MHC.

Which metal hydrides are suitable for operation within the temperature and pressure boundary conditions at HGHH, either covering the full pressure range or within sub-ranges?

Is a multi-stage arrangement necessary to achieve the required compression ratio and subsequently sufficient productivity, and which combination of metal hydrides is best suited for such a configuration? To what extent can key operating and design parameters, including heating and cooling temperatures, alloy mass, cycle time and compressor dimensions be optimized regarding productivity and specific energy consumption and what values are achievable within the feasible and realistic operating range?

Two metal hydrides were selected through a comprehensive literature review based on established selection criteria encompassing thermodynamic properties (PCI characteristics, plateau slope, hysteresis, reversible capacity), kinetics, cyclic stability, and resistance to gaseous impurities.

Single-stage simulations demonstrated that a two-stage configuration significantly enhances productivity, confirming the pressure range limitations evident from PCI diagrams. Hydralloy C1 was selected for Stage 1 (30 to 50 bar) and $Ti_{1.1}CrMn$ for Stage 2 (50 to 80 bar), thereby achieving the compression ratio of 2.67 in two steps.

The compressor was subsequently optimized by adjusting heating/cooling temperatures, metal hydride mass ratio between the stages, and cycle time. As shown in Table 6.1, this yields a total specific productivity of 132.21 Ln/kg$_{MH}$/h at moderate temperatures (10 to 65°C), deemed appropriate alongside this productivity level for technically feasible and realistic industrial implementation.

What are the resulting compressor dimensions and required alloy mass of a MHC scaled to the full hydrogen output of the 100 MW electrolyzer at Moorburg?

The scale-up analysis reveals substantial system dimensions, as outlined in 6.1. Apart from the the long compressor of around 28.3 m, the total required metal hydride mass (169,801.36 kg) already indicates the size of the system needed.

For comparison, the 4-stage mechanical piston compressor currently being build in Moorburg (higher compression ratio, equivalent throughput) has a estimated footprint of 16 × 14 m (224 m^2) weighing 180 tons. The MHC alloy mass is competitive (20 tons less), however auxiliary components (pressure vessels, heat exchangers, piping, structural supports) are currently not accounted for and will increase total system mass.

While the length of the developed MHC is substantially longer (+12.3 m) than the piston compressor, the width is significantly reduced. Multiple parallel compressor banks could mitigate the length, though at the cost of increased piping and periphery complexity adding to the required footprint.

In conclusion, the MHC offers no clear footprint advantage in comparison to the piston compressor. However, the available space at Moorburg accommodates the mechanical compressor, so the developed MHC is also feasible in this regard.

How do the thermal energy requirements of the scaled MHC system compare to the waste heat available at the HGHH site in terms of temperature level and thermal power?

The metal hydride compressor requires a continuous thermal input of max. $\dot{Q}_{\text{req}} = 18.81\ \text{MW}_{\text{th}}$. As demonstrated by Equation 5.7, the electrolyzer plant provides sufficient waste heat throughout its entire operational lifetime, with the available minimum case margin increasing from $4.3\ \text{MW}_{\text{th}}$ at BOL to $19.31\ \text{MW}_{\text{th}}$ at EOL as stack degradation progresses.

It must be noted, however, that this assessment is purely quantitative. A full feasibility evaluation additionally requires a sufficiently high quality of heat to drive desorption in both stages, also accounting for a minimum temperature driving force ΔT_{min} required for heat transfer. Heat transfer from the waste heat source to the hydride bed is physically impossible when the source temperature is lower than the required process temperature, regardless of the available power. While the electrolyzer provides sufficient waste heat in terms of quantity, the temperature level of the available waste heat represents a fundamental constraint. The maximum waste heat temperature of the electrolyzer at Moorburg amounts to 46 °C. The optimized compressor operates at desorption temperatures of 65 °C in Stage 1 and 60 °C in Stage 2, even after the temperature window was minimized as far as possible, allowing for a balance between compressor productivity and the narrow available temperature range, as illustrated in 5.1.5.

Consequently, the available waste heat temperature of 46 °C falls significantly below (19 °C and 14 °C) the required heating temperature of both stages and is therefore qualitatively insufficient to drive the compression cycle under the current operating conditions at Moorburg.

What measures, e.g. the consideration of alternative electrolyzer technologies with other operating temperature levels, could address potential deficits?

The preceding paragraph identified the waste heat temperature as the binding constraint for the Moorburg integration of the compressor. It should be noted that the waste heating temperature of 46 °C referenced throughout this assessment is specific to the atmospheric 100 MW electrolyzer considered in the original HGHH framework of this work, as described in Chapter 4.1.

As illustrated in 4.1 Scenario A, where the MHC operates downstream of this existing electrolyzer, the temperature deficit can not be resolved through the selection of another electrolyzer since this upstream unit is fixed. Addressing the temperature deficit in this scenario would therefore require an additional measure such as a heat pump.

Scenario B, however, opens a direct pathway to resolving the temperature constraint. Since this scenario already requires the introduction of a new, higher-pressure electrolyzer as part of the HGHH expansion, the technology selection for this electrolyzer is not predetermined. This creates the opportunity to select an electrolyzer that operates at a sufficiently high temperature to provide waste heat capable of driving desorption in both stages of the MHC without auxiliary heating.

As established in Section 2.1, three electrolyzer types are suitable for large-scale green hydrogen production coupled to a metal hydride compressor (MHC): alkaline electrolysis (AEL), proton exchange membrane electrolysis (PEM), and anion exchange membrane electrolysis (AEM). Both AEL and PEM electrolyzers can meet the temperature requirements of the proposed MHC, with PEM preferred due to its technological maturity and superior dynamic response. AEM remains a promising technology but still under development as well as with operating temperatures usually around 60°C rendering it unsuitable for supplying waste heat to an MHC requiring up to 65°C.

During the tendering process in Moorburg for the first 100 MW electrolyzer, two alternative AEL systems were evaluated alongside the baseline. Table 6.2 compares their operating conditions.

Table 6.2: Operating temperatures and pressures of electrolyzer technologies

Technology	Operating Temperature	Pressure
AEL (Vendor 1)	$\leq 80^{\circ}$C	30–32 bar
AEL (Vendor 2)	75°C	30.5 bar

All alternatives deliver an operating pressure of approximately 30 bar, thereby eliminating the initial mechanical compression stage from atmospheric pressure to 30 bar and exhibit operating temperatures with ΔT margins of min. 10 °C above the requirements of the MHC. However, AEL electrolyzers exhibit several drawbacks, particularly when integrated with fluctuating renewable energy sources. These include slow ion transport kinetics, resulting in sluggish response times, and high sensitivity to low current densities, neither of which is optimal for variable power inputs.

The cooling infrastructure must also be considered. The minimum achievable temperature with the current Moorburg setup is 35°C, which exceeds the required MHC cooling target of 10°C by 25°C. While expanding the cooling capacity, such as for the planned for the 800 MW scaleup, could address this shortfall, but introduces additional capital and operational costs.

In conclusion, integration of the developed MHC with the current atmospheric electrolyzer is infeasible due to insufficient waste heat temperature levels, despite adequate thermal energy quantities. The adoption of an alternative pressurized electrolyzer is fundamentally viable, however, a comprehensive evaluation of technology-specific advantages and disadvantages, particularly operating pressures, is essential. Should an atmospheric-pressure system be selected, an initial mechanical compressor stage to 30 bar would again be required. No recommendation is made to adopt AEL technology just for a potential integration wit an MHC, as the technology, while mature, has several drawbacks.

From both a systemic and energetic perspective, which advantages of the MHC approach, such as a potentially more compact design, or the direct utilization of waste heat, remain relevant under the given boundary conditions? Is an integration of a MHC in Moorburg feasible?

The main MHC advantages still relevant under the Moorburg boundary conditions are the avoidance of moving parts, the resulting lower vibration and noise emission, lower maintenance demand as well as the possibility of using waste heat as the driving energy source instead of electrical compression work. However, these advantages only become meaningful if the waste heat is at a sufficiently high temperature; in Moorburg, the available 46 °C waste heat is too low for the optimized two-stage MHC, even though the available thermal power is sufficient. The advantage of a more compact system over mechanical compression could not be confirmed either, as a significant bed-length is required for both stages.

Furthermore, regarding safety, it should be noted that even though hydrogen is stored at low pressure in MHC, the selected material, $Ti_{1.1}CrMn$, ignites in the presence of air or moisture, [making] its handling [...] both difficult and dangerous [117].

Taken together, the assessment yields a differentiated picture of MHC feasibility at the Moorburg site, both energetically and systemic. The developed system meets the quantitative thermal energy requirements across the entire electrolyzer lifetime, its alloy mass is broadly comparable to the mechanical alternative, and the available site area could accommodate the system. However, the temperature level of the waste heat provided by the current PEM electrolyzer represents a fundamental barrier to direct, thermally driven operation, that requires active temperature upgrading through a heat pump or higher-temperature electrolyzer as well as additional cooling. The integration of the developed MHC under under the present site conditions is not possible. The MHC therefore cannot be recommended as a direct drop-in replacement for the reciprocating piston compressors currently planned at HGHH, but remains a technically sound candidate contingent on deliberate system-level adaptations, while carefully weighing technical but also economical advanates and disadvantages.

7 Summary and Outlook

This thesis developed a metal hydride compressor for hydrogen pipeline injection as a possible alternative to conventional mechanical compression, using the Hamburg Green Hydrogen Hub (HGHH) as a real-world reference case with site-specific boundary conditions. The development was conducted by means of dynamic process simulation in Aspen Custom Modeler (ACM).

Following a comprehensive review of electrolyzer and mechanical compression technologies as well as the fundamentals on metal hydride materials, thermodynamics and kinetics, Chapter 3 and Chapter 4.1 characterized the operational context at Moorburg as well as the resulting boundary conditions. This includes the compression challenges arising from the required compression ratio of 2.67 (30 to 80 bar) with an exceptionally narrow, available temperature range between heating and cooling temperatures of only ΔT = 11 K.

In Chapter 4.3.1, a structured, criteria-based literature search was carried out, identifying Hydralloy C1, $Ti_{1.1}CrMn$ and Hydralloy C5 as the most suitable alloys. To address the limited experimental pressure-composition isotherm (PCI) data, the selected alloys were integrated into the Purdue Metal Hydride Toolbox, enabling the generation of isotherms across the full temperature range of interest. The resulting data were subsequently represented as polynomial surface fits and implemented into the ACM simulation model, which was extended to the specific needs of this work.

Chapter 5 presented a systematic parameter study covering one- and two stage configurations, operating temperatures, alloy mass ratios between stages, cycle times, and bed geometries and was evaluated by the resulting specific productivity, as well as energy demand. The optimized configuration consists of Hydralloy C1 in Stage 1 (30 to approximately 50 bar, 10 to 65 °C) and $Ti_{1.1}CrMn$ in Stage 2 (approximately 50 to 80 bar, 10 to 60 °C), with an equal alloy mass per stage, a half-cycle time of 10 minutes, and a slender bed geometry of 0.030 m diameter and 0.705 m length. Under these conditions, a total specific productivity of 132.21 $Ln/kg_{MH}/h$ is achieved, with an instantaneous heating/cooling demand of 0.2905 kW (Stage 1) and 0.2640 kW (Stage 2). The subsequent

scale-up revealed that handling the full hydrogen output of the 100 MW electrolyzer (1998 kg/h hydrogen) requires a total metal hydride mass of approximately 169,801 kg and a bed geometry of 1.20 m diameter and 28.3 m length per stage. The maximum instantaneous heating demand of 18.81 MW is quantitatively covered by the available electrolyzer waste heat throughout its entire operational lifetime (23.1 to 41.7 MW depending on system boundary and degradation state).

The feasibility assessment in Chapter 6 identified the waste heat temperature as the binding constraint: the available 46 °C falls ΔT = 19 K and ΔT = 14 K short of the required desorption temperatures in Stage 1 and Stage 2, respectively. Two technically viable pathways to resolving this deficit were identified. In Scenario A (operating the MHC downstream of the existing atmospheric PEM electrolyzer and mechanical compression) integration of a heat pump would be required to upgrade the waste heat temperature. In Scenario B (deploying the MHC in the context of the planned HGHH expansion with a pressurized electrolyzer) the selection of an higher-temperature electrolyzer could provide qualitatively sufficient waste heat without auxiliary equipment. In both scenarios, the MHC constitutes a technically feasible compression concept, but requires deliberate system-level adaptations that go beyond the current configuration at Moorburg.

7.1 Outlook

The present work developed a simulation-based foundation for MHC at industrial scale and clearly defines the governing constraints. Several directions for future work emerge from the findings:

Experimental validation: The two-stage configuration developed in this work has not been validated experimentally. Laboratory-scale tests on the Hydralloy C1 / $Ti_{1.1}CrMn$ stage combination under the identified operating conditions would be essential to confirm the predicted productivity, energy demand, and thermal cycling behavior, particularly under dynamic load conditions representative of fluctuating renewable energy input.

Techno-economic analysis: No economic evaluation was performed in this work. A full life-cycle cost comparison of the MHC system against the conventional reciprocating piston compressors in Moorburg, covering capital expenditure, maintenance costs, energy consumption, and expected service lifetimes, is essential before a technology recommendation with industrial relevance can be made.

Heat pump integration (Scenario A): A detailed energy and cost and scale analysis of coupling a heat pump to upgrade the waste heat from 46 °C to above 65 °C would quantify the additional energy penalty and assess whether the overall system remains energetically competitive with mechanical compression.

Alternative electrolyzer selection (Scenario B): The identification of AEL technology as a possible upstream technology should be followed by a compatibility study addressing the problematic dynamic load-behavior and the impact of the AEL operating pressure on downstream conditioning and MHC inlet conditions.

Multi-bed thermal arrangement and management: The scaled single-bed geometry of 1.20 m diameter and 28.3 m length presents significant engineering challenges for thermal management and material handling. Future work should investigate multi-bed arrangement, which adds complexity to the system as a whole (periphery) but at more practical bed dimensions.

Industrial-scale system requirements: The present work optimized the MHC configuration at laboratory scale and derived industrial dimensions through linear scale-up. However, the specific operational requirements of a fully scaled system warrant closer investigation. In particular, the achievable cycle times at large bed geometries, where radial heat and mass transport paths are substantially longer than in the laboratory-scale configuration. This could result in reduced specific productivity and altered thermal management requirements and tank design (fins or heating throughout the tank instead of an outer heat exchanger) at industrial scale. A dedicated study of the scaled system is therefore necessary to confirm the operational feasibility of the scaled system under realistic industrial conditions.

In summary, this work demonstrates that a metal hydride compressor is a technically conceivable and thermodynamically grounded alternative to mechanical compression at large-scale hydrogen production sites. The principal advantages (vibration-free and low-maintenance operation, the absence of moving parts, and the potential for direct utilization of low-grade waste heat) remain relevant. Under the specific boundary conditions of the HGHH at Moorburg, however, direct integration is not feasible without targeted system-level adaptations.

Bibliography

[1] Nationaler Wasserstoffrat. *Wasserstoff Aktionsplan Deutschland 2021-2025*. Tech. rep. July 2021. URL: www.wasserstoffrat.de.

[2] Hamburger Senat. *Erste Fortschreibung des Hamburger Klimaplans (Drucksache 21/19200)*. Tech. rep. Dec. 2019.

[3] Hamburger Senat. *Zweite Fortschreibung des Hamburger Klimaplans (Drucksache 22/12774)*. Tech. rep. Hamburg, Aug. 2023.

[4] *Kohleausstieg - Hamburger Energiewerke*. URL: https://www.hamburger-energiewerke.de/energiewende/energiewende-in-hamburg/kohleausstieg (visited on 11/18/2025).

[5] *Waermewende im Hamburger Hafen: Fernwaerme gruen transformieren - energiezukunft*. Oct. 2025. URL: https://www.energiezukunft.eu/erneuerbare-energien/waermewende/fernwaerme-gruen-transformieren (visited on 02/16/2026).

[6] Behoerde fuer Wirtschaft und Innovation. *Green Hydrogen Hub Europe - Hamburg als Drehkreuz fuer Wasserstoffimporte nach Deutschland und Europa - Ein wirtschaftspolitisches Konzept der Behoerde fuer Wirtschaft und Innovation*. Tech. rep. Feb. 2022.

[7] Antwort des Senats Abgeordneter Stephan Jersch (Die Linke). *Schriftliche Kleine Anfrage: Truegerische Ruhe um Moorburg? (Drucksache 23/2272)*. Tech. rep. Hamburg, Dec. 2025.

[8] HGHH. *HGHH – Hamburg Green Hydrogen Hub*. URL: https://www.hghh.eu/ (visited on 02/16/2026).

[9] Furat Dawood, Martin Anda, and G. M. Shafiullah. "Hydrogen production for energy: An overview". In: *International Journal of Hydrogen Energy* 45 (2020), pp. 3847–3869. ISSN: 03603199. DOI: 10.1016/j.ijhydene.2019.12.059.

[10] T. Amirthan and M. S.A. Perera. "The role of storage systems in hydrogen economy: A review". In: *Journal of Natural Gas Science and Engineering* 108

(Dec. 2022), p. 104843. ISSN: 18755100. DOI: 10.1016/j.jngse.2022.104843.

[11] Sajid Ali Ansari et al. "Sustainable Hydrogen Production, a Review of Methods, Types, Applications, Challenges, and Future Perspectives". In: *Global Challenges* 9 (2025), p. 2500086. ISSN: 20566646. DOI: 10.1002/gch2.202500086.

[12] M. Hermesmann and T. E. Mueller. "Green, Turquoise, Blue, or Grey? Environmentally friendly Hydrogen Production in Transforming Energy Systems". In: *Progress in Energy and Combustion Science* 90 (Feb. 2022), p. 100996. ISSN: 03601285. DOI: 10.1016/j.pecs.2022.100996.

[13] Eike S. Wienken et al. "Zero-dimensional electrochemical modeling of a market-ready anion exchange membrane electrolyzer". In: *Journal of Power Sources* 665 (Dec. 2025), p. 239086. ISSN: 03787753. DOI: 10.1016/j.jpowsour.2025.239086.

[14] J. O. Abe et al. "Hydrogen energy, economy and storage: Review and recommendation". In: *International Journal of Hydrogen Energy* 44 (June 2019), pp. 15072–15086. ISSN: 03603199. DOI: 10.1016/j.ijhydene.2019.04.068.

[15] Julián Atilio Puszkiel. "Tailoring the Kinetic Behavior of Hydride Forming Materials for Hydrogen Storage". In: *Gold Nanoparticles - Reaching New Heights*. IntechOpen, 2018. DOI: http://dx.doi.org/10.5772/intechopen.82433.

[16] Katja Mau. "Energiewendebeirat, 13. Sitzung". In: Hamburger Energienetze, 2024.

[17] Aiman Albatayneh et al. "Future of Electric and Hydrogen Cars and Trucks: An Overview". In: *Energies* 16 (2023). ISSN: 19961073. DOI: 10.3390/en16073230.

[18] "Metal Hydrides for Hydrogen-Based Energy Storage". In: ed. by Volodymyr Yartys. 1st. Vol. 2. Woodhead Publishing, Dec. 2025. Chap. 7, pp. 289–339. ISBN: 978-0-443-44873-7. DOI: 10.1016/C2025-0-01811-2.

[19] Georgios Karagiorgis et al. "Design, development, construction and operation of a novel metal hydride compressor". In: *International Journal of Hydrogen Energy* 42.17 (Apr. 2017), pp. 12364–12374. ISSN: 03603199. DOI: 10.1016/j.ijhydene.2017.03.195.

[20] Giuseppe Sdanghi et al. "Towards non-mechanical hybrid hydrogen compression for decentralized hydrogen facilities". In: *Energies* 13.12 (June 2020). ISSN: 19961073. DOI: 10.3390/en13123145.

[21] G. Sdanghi et al. "Review of the current technologies and performances of hydrogen compression for stationary and automotive applications". In: *Renewable*

and Sustainable Energy Reviews 102 (Mar. 2019), pp. 150–170. ISSN: 18790690. DOI: 10.1016/j.rser.2018.11.028.

[22] Jose Bellosta von Colbe et al. "Application of hydrides in hydrogen storage and compression: Achievements, outlook and perspectives". In: *International Journal of Hydrogen Energy* 44.15 (Jan. 2019), pp. 7780–7808. ISSN: 03603199. DOI: 10.1016/j.ijhydene.2019.01.104.

[23] M. V. Lototskyy et al. "Metal hydride hydrogen compressors: A review". In: *International Journal of Hydrogen Energy* 39.11 (Apr. 2014), pp. 5818–5851. ISSN: 03603199. DOI: 10.1016/j.ijhydene.2014.01.158.

[24] V. A. Martinez Lopez et al. "Dynamic operation of water electrolyzers: A review for applications in photovoltaic systems integration". In: *Renewable and Sustainable Energy Reviews* 182 (May 2023), p. 113407. ISSN: 18790690. DOI: 10.1016/j.rser.2023.113407.

[25] Els van der Roest et al. "Utilisation of waste heat from PEM electrolysers – Unlocking local optimisation". In: *International Journal of Hydrogen Energy* 48.72 (Apr. 2023), pp. 27872–27891. ISSN: 03603199. DOI: 10.1016/j.ijhydene.2023.03.374.

[26] Mostafa El-Shafie. "Hydrogen production by water electrolysis technologies: A review". In: *Results in Engineering* 20 (Dec. 2023). ISSN: 25901230. DOI: 10.1016/j.rineng.2023.101426.

[27] H. Kumar S. Lim. "PEM overview". In: *The Royal Society of Chemistry* 7.Sustainable Energy & Fuels (July 2023), pp. 3560–3583. DOI: 10.1039/d3se00336a.

[28] Bahman Amini Horri and Hasan Ozcan. "Green hydrogen production by water electrolysis: Current status and challenges". In: *Current Opinion in Green and Sustainable Chemistry* 47 (2024), p. 100932. ISSN: 24522236. DOI: 10.1016/j.cogsc.2024.100932.

[29] Ajitanshu Vedrtnam, Kishor Kalauni, and Rahul Pahwa. "A review of water electrolysis technologies with insights into optimization and numerical simulations". In: *International Journal of Hydrogen Energy* 140 (2025), pp. 694–727. ISSN: 03603199. DOI: 10.1016/j.ijhydene.2025.05.295.

[30] Marcelo Carmo et al. "A comprehensive review on PEM water electrolysis". In: *International Journal of Hydrogen Energy* 38.12 (Mar. 2013), pp. 4901–4934. ISSN: 03603199. DOI: 10.1016/j.ijhydene.2013.01.151.

[31] Jörn Brauns and Thomas Turek. "Alkaline water electrolysis powered by renewable energy: A review". In: *Processes* 8 (Feb. 2020), p. 248. ISSN: 22279717. DOI: 10.3390/pr8020248.

[32] ACS Industries. *PEM vs Alkaline Electrolyzer: Which is Right for Your Application?* URL: https://acsindustries.com/2025/06/18/pem-vs-alkaline-electrolyzer/ (visited on 02/27/2026).

[33] Waqad Ul Mulk et al. "Electrochemical hydrogen production through anion exchange membrane water electrolysis (AEMWE): Recent progress and associated challenges in hydrogen production". In: *International Journal of Hydrogen Energy* 94 (Nov. 2024), pp. 1174–1211. ISSN: 03603199. DOI: 10.1016/j.ijhydene.2024.11.143.

[34] Kandela Ruiz et al. "Current market status of solid oxide hydrogen technology: From starting materials to system level". In: *Energy Reports* 15 (Feb. 2026), p. 109091. ISSN: 23524847. DOI: 10.1016/j.egyr.2026.109091.

[35] Udo Lubenau et al. *H2-Kurzstudie: Wasserstoffqualitaet in einem gesamtdeutschen Wasserstoffnetz*. Tech. rep. DBI Gas- und Umwelttechnik GmbH, Frontier Economics Limited, June 22.

[36] Efenwengbe Nicholas Aminaho, Ndukaegho Sabastine Aminaho, and Faith Aminaho. "Techno-economic assessments of electrolyzers for hydrogen production". In: *Applied Energy* 399 (Dec. 2025). ISSN: 03062619. DOI: 10.1016/j.apenergy.2025.126515.

[37] McKenzie Hubert et al. *Hydrogen Shot: Water Electrolysis Technology Assessment*. Tech. rep. U.S Department Of Energy.

[38] Heinz P. Bloch. *A PRACTICAL GUIDE TO COMPRESSOR TECHNOLOGY*. Second Edition. Hoboken. New Jersey: John Wiley & Sons, Inc., 2006, pp. 5–27. ISBN: 978-0-471-72793-4.

[39] Kui Lu, Ibrahim A. Sultan, and Truong H. Phung. "A Literature Review of the Positive Displacement Compressor: Current Challenges and Future Opportunities". In: *Energies* 16.20 (Oct. 2023). ISSN: 19961073. DOI: 10.3390/en16207035.

[40] Pascal Stouffs, Mohand Tazerout, and Pierre Wauters. "Thermodynamic analysis of reciprocating compressors". In: *Int. J. Therm. Sci* 40 (2001), pp. 52–66.

[41] Helmut Tschoeke and Herbert Hoelz. "Dubbel Taschenbuch fuer den Maschinenbau 3: Maschinen und Systeme". In: *Dubbel Taschenbuch fuer den Maschinenbau 3: Maschinen und Systeme*. Springer Berlin Heidelberg, 2020. Chap. 3, pp. 39–68. DOI: 10.1007/978-3-662-59715-6{_}3.

[42] A. Peschel. "Industrial Perspective on Hydrogen Purification, Compression, Storage, and Distribution". In: *Fuel Cells* 20.4 (Aug. 2020), pp. 385–393. ISSN: 16156854. DOI: 10.1002/fuce.201900235.

[43] Mohammad Reza Tahan. "Recent advances in hydrogen compressors for use in large-scale renewable energy integration". In: *International Journal of Hy-*

drogen Energy 47 (2022), pp. 35275–35292. ISSN: 03603199. DOI: 10.1016/j.ijhydene.2022.08.128.

[44] Ann-Christin Fleer et al. *Compression and hydrogen transport: A technical and economic analysis*. June 2025.

[45] S. Orlova, N. Mezeckis, and V. P.K. Vasudev. "Compression of Hydrogen Gas for Energy Storage: A Review". In: *Latvian Journal of Physics and Technical Sciences* 60.2 (Apr. 2023), pp. 4–16. ISSN: 08688257. DOI: 10.2478/lpts-2023-0007.

[46] Leonard van Lier et al. *HYDROGEN COMPRESSION BOOSTING THE HYDROGEN ECONOMY*. Nov. 2022.

[47] Detlef Stolten and Bernd Emonts, eds. *Hydrogen Science and Engineering: Materials, Processes, Systems and Technology*. Wiley-VCH Verlag GmbH & Co. KGaA, 2016, p. 662. ISBN: 9783527674268. DOI: 10.1002/9783527674268.

[48] LLC air Squared. *Scroll Technology for Hydrogen Recirculation*. 2026. URL: https://airsquared.com/markets/clean-energy/fuel-cell/hydrogen-recirculation/ (visited on 03/21/2026).

[49] Anil Taskin et al. "Development and validation of an all-metal scroll pump for PEM fuel cell hydrogen recirculation". In: *International Journal of Hydrogen Energy* 184 (Nov. 2025). ISSN: 03603199. DOI: 10.1016/j.ijhydene.2025.151654.

[50] Wittig - Ingersoll Rand. *Hydrogen Compressors for critical applications*. URL: https://www.wittigsystems.com/en/industries/hydrogen/ (visited on 03/21/2026).

[51] Roots Blowers. *Roots Rotary Blowers*. URL: https://www.rootsblower.com/en/products/ (visited on 02/16/2026).

[52] Xiangcheng Kong et al. "Investigation on the pressure fluctuation of hydrogen Roots pump with a novel reflow structure for fuel cell vehicles". In: *International Journal of Hydrogen Energy* 50 (Jan. 2024), pp. 66–78. ISSN: 03603199. DOI: 10.1016/j.ijhydene.2023.08.021.

[53] Qingqing Zhang et al. "Study on the Scroll Compressors Used in the Air and Hydrogen Cycles of FCVs by CFD Modeling". In: *International Compressor Engineering Conference*. 2018, p. 2535. URL: https://docs.lib.purdue.edu/icec/2535.

[54] Yian Zhang, Ying Zhao, and Xueyuan Peng. "Three-dimensional CFD Simulation of a Roots Blower for the Hydrogen Circulating Pump". In: *International Compressor Engineering Conference*. Purdue e-Pubs. 2018, p. 2625. URL: https://docs.lib.purdue.edu/icec/2625.

[55] Nash - An Ingersoll Rand Business. *Hydrogen Compressors with Liquid Ring Technology*. URL: https://www.nashpumps.com/en/industries/chemical/hydrogen-compression/ (visited on 03/21/2026).

[56] Si Huang et al. "Theoretical Model for the Performance of Liquid Ring Pump Based on the Actual Operating Cycle". In: *International Journal of Rotating Machinery* 2017 (2017). ISSN: 15423034. DOI: 10.1155/2017/3617321.

[57] Everllence. *Screw compressors for hydrogen*. URL: https://www.everllence.com/industries/campaigns/screw-compressors-for-hydrogen (visited on 03/20/2026).

[58] Ltd. Kawasaki Heavy Industries. *World's-first Centrifugal Hydrogen Compressor for Hydrogen Liquefaction Plants Starts Demonstration*. Mar. 2026. URL: https://global.kawasaki.com/en/corp/newsroom/news/detail/?f=20260305_6618 (visited on 03/21/2026).

[59] C Tellier. "APPLICATION OF AXIAL FLOW COMPRESSORS FOR LONG DISTANCE PIPELINE TRANSMISSION OF HYDROGEN". In: *Int. J. Hydrogen Energy* 6.4 (1981), pp. 413–422.

[60] Kirk Lupkes. *Advanced Hydrogen Compressor for Hydrogen Storage Integrated with a Powerplant*. Tech. rep. Work performed under DOE Award: DE-FE0032033, June 2022.

[61] Antonio Giuffrida and Paolo Colbertaldo. "Overview of diaphragm compressors for hydrogen service: capacity, discharge pressure and operational challenges". In: *Journal of Energy Storage* 129 (Sept. 2025). ISSN: 2352152X. DOI: 10.1016/j.est.2025.117286.

[62] Xin Ran. *Hydrogen Ionic Compressor*. URL: http://www.xinrancompressor.com/9-3-hydrogen-ionic-compressor.html (visited on 03/21/2026).

[63] Hao Zhou et al. "Development and experimental research of an integrated dynamic simulation platform for an ionic liquid hydrogen compressor utilized in hydrogen refueling stations". In: *Renewable Energy* 252 (Oct. 2025). ISSN: 18790682. DOI: 10.1016/j.renene.2025.123565.

[64] Neumann und Esser. *Piston Compressors*. URL: https://www.neuman-esser.com/en/products-services/compressors-compressor-systems/piston-compressors/ (visited on 02/16/2026).

[65] Luiz Soranio and Neumann und Esser. *Design Considerations on Reciprocating Compressors for Green Hydrogen Production Plants*. 2024. URL: https://www.neuman-esser.com/en/news-media/magazine/design-

considerations-on-reciprocating-compressors-for-green-hydrogen-production-plants/ (visited on 02/15/2026).

[66] Mykhaylo Lototskyy and Vladimir Linkov. "Thermally driven hydrogen compression using metal hydrides". In: *International Journal of Energy Research* 46.15 (Dec. 2022), pp. 22049–22069. ISSN: 1099114X. DOI: 10.1002/er.8189.

[67] Gabriele Scarpati et al. "A comprehensive review on metal hydrides-based hydrogen storage systems for mobile applications". In: *Journal of Energy Storage* 102 (Nov. 2024). ISSN: 2352152X. DOI: 10.1016/j.est.2024.113934.

[68] J. A. Puszkiel et al. "On the hydrogen storage properties and life cycle evaluation of a room temperature hydride for scale-up applications: The case of an AB2-alloy". In: *International Journal of Hydrogen Energy* 118 (May 2025), pp. 482–499. ISSN: 03603199. DOI: 10.1016/j.ijhydene.2025.03.161.

[69] Kakumanu Suvarna Jaya Prakash and Vinod Kumar Sharma. "Recent developments on metal hydride hydrogen compressors – A comprehensive review". In: *Journal of Alloys and Compounds* 1037 (July 2025), p. 182505. ISSN: 09258388. DOI: 10.1016/j.jallcom.2025.182505.

[70] National Institute of Standards and Technology. *NIST Chemistry WebBook*. URL: https://webbook.nist.gov/chemistry/form-ser/ (visited on 02/19/2026).

[71] Gary Sandrock. "A panoramic overview of hydrogen storage alloys from a gas reaction point of view". In: *Journal of Alloys and Compounds* 293 (1999), pp. 877–888.

[72] Jussara Barale. "Hydrogen Storage and Compression based on Metal Hydrides Jussara Barale". PhD thesis. Torino: Universita degli Studi di Torino, June 2022.

[73] Hans-Peter Klein. "Betriebsverhalten einer zweistufigen Metallhydrid-Sorptionsanlage zur Kälteerzeugung". PhD thesis. Stuttgart: Universität Stuttgart, July 2007.

[74] Christoph Weckerle. "A metal hydride air-conditioning system for fuel cell vehicles". PhD thesis. University of Stuttgart, 2020.

[75] Michael Hirscher. *Handbook of Hydrogen Storage: New Materials for Future Energy Storage*. Ed. by M Hirscher. WILEY-VCH, 2010. ISBN: 978-3-527-32273-2.

[76] A. M. Neves et al. "Modeling the kinetic behavior of the Li-RHC system for energy-hydrogen storage: (I) absorption". In: *International Journal of Hydrogen Energy* 46.63 (Sept. 2021), pp. 32110–32125. ISSN: 03603199. DOI: 10.1016/j.ijhydene.2021.06.227.

[77] André Martins Neves et al. "Kinetic-model identification in metal-hydride reactions using neural network autoencoder surrogate models". In: *Energy and AI* 22 (Dec. 2025). ISSN: 26665468. DOI: 10.1016/j.egyai.2025.100659.

[78] Tyler G. Voskuilen, Essene L. Waters, and Timothée L. Pourpoint. "A comprehensive approach for alloy selection in metal hydride thermal systems". In: *International Journal of Hydrogen Energy* 39.25 (Aug. 2014), pp. 13240–13254. ISSN: 03603199. DOI: 10.1016/j.ijhydene.2014.06.119. URL: https://github.com/PurdueH2Lab/MetalHydrideToolbox.

[79] Luxcara. *Hamburg Green Hydrogen Hub celebrates laying of foundation stone for 100 MW electrolyzer*. URL: https://www.luxcara.com/press-releases/hamburg-green-hydrogen-hub-celebrates-laying-of-foundation-stone-for-100-mw-electrolyzer (visited on 02/16/2026).

[80] *"We're creating the heart of the hydrogen economy in Hamburg" - Renewable Energies Hamburg | EEHH*. URL: https://www.erneuerbare-energien-hamburg.de/en/news/details/we-re-creating-the-heart-of-the-hydrogen-economy-in-hamburg.html (visited on 02/15/2026).

[81] Luxcara. *Hamburg Green Hydrogen Hub awards contract for 100 MW electrolyzer to Siemens Energy*. URL: https://www.luxcara.com/press-releases/hamburg-green-hydrogen-hub-awards-contract-for-100-mw-electrolyzer-to-siemens-energy (visited on 02/16/2026).

[82] Mitteilung des Senats an die Buergerschaft. *Transformation des ehemaligen Kohlekraftwerks Moorburg zu einem Green Energy Hub (Drucksache 22/15481)*. Tech. rep. June 2024.

[83] Bundesministerium fuer Wirtschaft und Klimaschutz. *Uebersicht der deutschen IPCEI Hy2Infra-Projekte*. Tech. rep.

[84] Ramboll. *Hamburgs Green Hydrogen Hub - 100 MW Elektrolyseanlage fuer die Dekarbonisierung*. URL: https://www.ramboll.com/de-de/projekte/energie/hamburgs-green-hydrogen-hub-100-mw-elektrolyseanlage-fur-die-dekarbonisierung (visited on 02/16/2026).

[85] Europa. *Commission approves up to €6.9 billion of State aid by seven Member States for the third Important Project of Common European Interest in the hydrogen value chain*. Feb. 2024. URL: https://ec.europa.eu/commission/presscorner/detail/en/ip_24_789 (visited on 02/16/2026).

[86] Hamburg. *Bilanz des Statistikamtes Nord fuer 2023 - Erneut deutliche CO2-Minderung in Hamburg*. URL: https://www.hamburg.de/politik-und-verwaltung/behoerden/bukea/themen/klima/klimaschutz-klimaplan/co2-bilanz-hh-2023-169240 (visited on 02/16/2026).

[87] Vattenfall - Pressemitteilung. *Vattenfall verkauft Heizkraftwerk Moorburg an Hamburger Energiewerke (HEnW)*. Mar. 2023. URL: https://group.vattenfall.com/de/newsroom/pressemitteilungen/2023/vattenfall-verkauft-heizkraftwerk-moorburg-an-die-hamburger-energiewerke-henw (visited on 02/16/2026).

[88] Siemens Energy Global GmbH & Co. KG Transformation of Industry. *Brochure:Hydrogen and Power-to-X solutions*. 2025.

[89] Siemens Energy Global GmbH & Co. KG Transformation of Industry. *Elyzer plant Fact sheet: 100 MW electrolyzer reference plant*. 2025.

[90] Drees & Sommer. *Hamburg Green Hydrogen Hub (HGHH) - From coal-fired power plant to engine of the future: Drees und Sommer contributes expertise across all project phases*. URL: https://www.dreso.com/de/en/projects/details/hamburg-green-hydrogen-hub-hghh (visited on 02/16/2026).

[91] Vattenfall. *Moorburg: Von Kohlekraft zu Wasserstoff*. Apr. 2021. URL: https://energysales.vattenfall.de/publikationen/artikel/hamburg-moorburg-vom-kohlekraftwerk-zum-wasserstoff-hub (visited on 02/16/2026).

[92] Bundesnetzagentur. *Ausschreibung nach dem KVBG / Gebotstermin 1. September 2020*. Dec. 2020. URL: https://www.bundesnetzagentur.de/DE/Fachthemen/ElektrizitaetundGas/Kohleausstieg/BeendeteAusschreibungen/0109_2020/start.html (visited on 02/16/2026).

[93] Luxcara. *Luxcara joins Hamburg Green Hydrogen Hub*. Sept. 2023. URL: https://www.luxcara.com/press-releases/luxcara-joins-hamburg-green-hydrogen-hub (visited on 02/16/2026).

[94] Hamburg. *Platz fuer gruene Wasserstoff-Infrastruktur - Sprengung der Kamine am Standort Moorburg*. Nov. 2024. URL: https://www.hamburg.de/politik-und-verwaltung/behoerden/bwai/aktuelles/pressemeldungen/2024-11-10-bwi-sprengung-der-kamine-am-standort-moorburg-987682 (visited on 02/16/2026).

[95] Arcadis. *Rueckbau Steinkohlekraftwerk Hamburg Moorburg*. URL: https://www.arcadis.com/de-de/projects/europe/germany/rueckbau-kraftwerk-hamburg-moorburg (visited on 02/16/2026).

[96] Kraftanlagen - An Equans company. *Hamburg Green Hydrogen Hub has commissioned Kraftanlagen to construct the infrastructure for 100 MW electrolyzer*. Oct. 2025. URL: https://www.kraftanlagen.com/en/hamburg-

green-hydrogen-hub-has-commissioned-kraftanlagen-to-construct-the-infrastructure-for-100-mw-electrolyzer/ (visited on 02/16/2026).

[97] Hamburger Energiewerke. *Grundsteinlegung fuer Wasserstoff-Elektrolyseur*. Dec. 2025. URL: https://www.hamburger-energiewerke.de/services/magazin/grundsteinlegung-fuer-wasserstoff-elektrolyseur (visited on 02/17/2026).

[98] Hamburg Green Hydrogen Hub Bjoern Jotzo. *Hamburg Green Hydrogen Hub - Wann ist gruener Wasserstoff gruen? Nationale und europaeische Regulatorik*. Tech. rep. 2024.

[99] Bundesnetzagentur. *Kernnetz für Wasserstoff*. 2024. URL: https://www.bundesnetzagentur.de/DE/Fachthemen/ElektrizitaetundGas/Wasserstoff/Kernnetz/start.html,%20pr%C3%A4sentation-ewb (visited on 02/20/2026).

[100] Hamburger Energienetze. *HH-WIN – Hamburger Wasserstoff-Industrie-Netz*. URL: https://www.hamburger-energienetze.de/content/wasserstoffkarte/index.html (visited on 02/18/2026).

[101] Hamburger Energienetze. *HH-WIN nutzt Bestandsleitung und senkt Investition*. Mar. 2025. URL: https://www.hamburger-energienetze.de/ueber-uns/presse/pressemitteilungen/hh-win-nutzt-bestandsleitung-und-senkt-investition (visited on 02/20/2026).

[102] Hyperlink-Gasunie. *Hyperlink 1 - 2*. URL: https://www.hyperlink-gasunie.de/en/about-hyperlink/hyperlink-1---2 (visited on 02/18/2026).

[103] Erneuerbare Energien Hamburg. *„Das Netz ist die Grundvoraussetzung fuer das Wasserstoffoekosystem in Hamburg“*. URL: https://www.erneuerbare-energien-hamburg.de/de/blog/details/das-netz-ist-die-grundvoraussetzung-f%5C%C3%5C%BCr-das-wasserstof%5Cf%5C%C3%5C%B6kosystem-in-hamburg.html (visited on 02/18/2026).

[104] Erneuerbare Energien Hamburg. *Wasserstoffnetz HH-WIN*. URL: https://www.erneuerbare-energien-hamburg.de/de/news/details/wasserstoffnetz-hh-win.html.

[105] Abhishek Parida et al. “Experimental study and performance evaluation of a large-scale multistage metal hydride-based hydrogen compressor”. In: *Applied*

Energy 390 (July 2025). ISSN: 03062619. DOI: 10.1016/j.apenergy.2025.125798.

[106] Bilfinger. *Wasserstofftrockung mit H2DRY*. URL: https://www.bilfinger.com/de/de/h2dry/ (visited on 02/19/2026).

[107] AspenTech. *Aspen Custom Modeler: Optimize processes with specialized equipment by creating and sharing custom high-fidelity models with trusted accuracy and flexible workflows*. URL: https://www.aspentech.com/en/products/engineering/aspen-custom-modeler.

[108] AspenTech. *Aspen Custom Modeler 12.1 User Guide*. Aug. 2003. URL: http://www.aspentech.com/.

[109] K. W. Bowman et al. "Evaluation of ACCMIP outgoing longwave radiation from tropospheric ozone using TES satellite observations". In: *Atmospheric Chemistry and Physics* 13.8 (Apr. 2013), pp. 4057–4072. ISSN: 16807324. DOI: 10.5194/acp-13-4057-2013.

[110] GfE Metalle und Materialien GmbH. *HYDRALLOY C:GfE Art. No. 2019929 / 2005169 / 2004732*. June 2024.

[111] Alexander Wimmer et al. "High performance reactor of a metal hydride based cooling system for air-conditioning of fuel cell electric vehicles". In: *Applied Energy* 391 (Aug. 2025). ISSN: 03062619. DOI: 10.1016/j.apenergy.2025.125911.

[112] Marc Linder and Rudi Kulenovic. "An energy-efficient air-conditioning system for hydrogen driven cars". In: *International Journal of Hydrogen Energy* 36.4 (Jan. 2011), pp. 3215–3221. ISSN: 03603199. DOI: 10.1016/j.ijhydene.2010.11.101.

[113] Kai Herbrig et al. "Hydrogen storage systems based on hydride-graphite composites: Computer simulation and experimental validation". In: *International Journal of Hydrogen Energy* 38.17 (June 2013), pp. 7026–7036. ISSN: 03603199. DOI: 10.1016/j.ijhydene.2013.03.104.

[114] Lukas Fleming. *Persönliche Kommunikation*. Persönliches Gespräch mit M. Sc., HSU, 2025. 2025.

[115] Claudio Corgnale and Martin Sulic. "High pressure thermal hydrogen compression employing Ti1.1CrMn metal hydride material". In: *JPhys Energy* 2 (2020), p. 014003. ISSN: 25157655. DOI: 10.1088/2515-7655/ab47b0.

[116] Andrea Mazzucco and Masoud Rokni. "Generalized computational model for high-pressure metal hydrides with variable thermal properties". In: *International Journal of Hydrogen Energy* 40 (2015), pp. 11470–11477. ISSN: 03603199. DOI: 10.1016/j.ijhydene.2015.03.032.

[117] Milan Visaria and Issam Mudawar. “Coiled-tube heat exchanger for high-pressure metal hydride hydrogen storage systems - Part 2. Computational model”. In: *International Journal of Heat and Mass Transfer* 55 (Dec. 2011), pp. 1796–1806. ISSN: 00179310. DOI: 10.1016/j.ijheatmasstransfer.2011.11.036.

[118] M. Kandavel et al. “Improvement of hydrogen storage properties of the AB2 Laves phase alloys for automotive application”. In: *International Journal of Hydrogen Energy* 33 (July 2008), pp. 3754–3761. ISSN: 03603199. DOI: 10.1016/j.ijhydene.2008.04.042.

[119] Milan Visaria and Issam Mudawar. “Experimental investigation and theoretical modeling of dehydriding process in high-pressure metal hydride hydrogen storage systems”. In: *International Journal of Hydrogen Energy* 37.7 (Jan. 2012), pp. 5735–5749. ISSN: 03603199. DOI: 10.1016/j.ijhydene.2011.12.140.

[120] Yoshitsugu Kojima et al. “Development of metal hydride with high dissociation pressure”. In: *Journal of Alloys and Compounds* 419 (Nov. 2005), pp. 256–261. ISSN: 09258388. DOI: 10.1016/j.jallcom.2005.08.078.

[121] A. Satheesh and P. Muthukumar. “Performance investigation of double-stage metal hydride based heat pump”. In: *Applied Thermal Engineering* 30.17-18 (Dec. 2010), pp. 2698–2707. ISSN: 13594311. DOI: 10.1016/j.applthermaleng.2010.07.021.

[122] AGST Draht & Biegetechnik GmbH. *Data sheet: AISI 316L / EN 1.4404 (DIN EN 10088-3)*. Tech. rep. AGST Draht & Biegetechnik GmbH, Mar. 2026.

[123] M W Davids et al. “Design and development of metal hydride hydrogen compressors at HYSA systems based at the University of the Western Cape”. In: *2nd Southern African Hydrogen and Fuel Cell Conference*. 2025.

Anhang

Eidesstattliche Erklärung

Ich versichere hiermit, dass ich die vorliegende Arbeit mit dem Titel

Simulation-Based Development of a Metal hydride Compressor for Hydrogen Pipeline Injection

ohne fremde Hilfe selbständig verfasst und nur die angegebenen Quellen und Hilfsmittel verwendet habe.
Wörtlich oder dem Sinn nach aus anderen Werken entnommene Stellen sind unter Angabe der Quellen kenntlich gemacht.

Ort/Datum: _____

Unterschrift: _____